THE DYNAMICS AND MISFOLDING PATHWAYS OF THE PRION PROTEIN AT ATOMIC RESOLUTION

Chin Jung Cheng

A dissertation

submitted in partial fulfillment of the

requirements for the degree of

Doctor of Philosophy

University of Washington

2015

Reading Committee:

Valerie Daggett, Chair

James Bryers

Shaoyi Jiang

Program Authorized to Offer Degree:
Bioengineering

University of Washington

Abstract

THE DYNAMICS AND MISFOLDING PATHWAYS OF THE PRION PROTEIN AT ATOMIC RESOLUTION

Chin Jung Cheng

Chair of the Supervisory Committee:
Professor Valerie Daggett
Bioengineering

Prion diseases are fatal, transmissible and incurable neurodegenerative diseases that only infect mammals. While the manifestation of prion disease is not completely understood, it is known that the prion protein (PrP) plays a critical role in prion disease development. The PrP can exist in two different isoforms: PrP^C is the native cellular form which is innocuous, while PrP^{Sc} is the pathogenic form. PrP^{Sc} is aggregation-prone thus forming soluble oligomers which are toxic and infectious. Using molecular dynamics simulations, we have investigated misfolding pathways for human PrP pathogenic mutants and bovine PrP at acidic pH. In order to better understand the molecular dynamics of the PrP^C at a physiological environment, we have also performed simulations of the human PrP^C attached with glycans in a membrane environment, revealing protective mechanisms against misfolding. Using recent experimental data on PrP^{Sc} soluble oligomers, we have validated our current structural model for PrP^{Sc} oligomers and finally,

combining our findings from both bovine PrP$^{\text{Sc}}$ and human PrP$^{\text{C}}$, we have constructed a system to model the PrP$^{\text{Sc}}$-induced misfolding for the human PrP$^{\text{C}}$ in a physiological environment. Our research sheds light on the PrP misfolding mechanism at the atomic level, potentially advancing future therapeutic and diagnostic development on prion diseases.

TABLE OF CONTENTS

LIST OF FIGURES

LIST OF TABLES

ACKNOWLEDGEMENTS

I would like to thank Professor Valerie Daggett for the mentorship that I have received throughout the PhD program. I would like to thank my committee members, Professors James Bryers, Shaoyi Jiang, and John Berg for their time and commitment. I would like to thank Daggett lab members, especially people who helped maintaining the servers, including Drs. Michelle Mccully, Steve Rysavy, Clare Towse, Wen-wai Yim, Ivan Vulovic, Gene Hopping and Matt Childers. I would also like to thank the two postdocs, Drs. Marc van der Kamp and Wei Chen who gave me significant guidance on my prion project. I would like to thank my officemates for companionship, including, Sara Calhoun, Benjamin Mo, Sarah Chamberlain, Michael Liao, Tom Schmidlin and Matt Childers. I am grateful for the financial support provided by NIH and the UW BIOE department.

DEDICATION

I would like to thank my girlfriend, Stephanie, for her endless support on my general exam, job search and life in general. I would like to thank my housemates Cameron, Rochelle, Ted and Leslie for their support during tough times and for all the happy memories that we share.

Chapter 1

BACKGROUND AND SIGNIFICANCE

1.1 Prion Diseases

Prion diseases are fatal, transmissible and incurable neurodegenerative diseases that infect mammals (1, 2). Transmission of prion disease among mammals can occur via ingestion of prion-infected tissues of deceased mammals. For example, humans have acquired variant Creutzfedlt-Jacob Disease (vCJD) by consuming prion-contaminated beef products (3, 4). However, some prion diseases, such as chronic wasting disease (CWD) and scrapie, can be transmitted to other mammals via their prion-contaminated saliva, urine, and feces (5–8). CWD in the US spread from 6 states in 2002 to 16 states in 2013 (9, 10). Given that CWD can transmit to a range of mammals (10–12), including some primates (13), the increasing spread of CWD has raised concerns about food safety in elk meat products and prion-contamination in the wildlife (14). In addition, the lack of effective prion diagnostics and therapeutics has made prion disease even more threatening to public health. Furthermore, prion diseases among livestock, especially cattles, significantly impacts the economy of the society: in 2003, a single case of bovine spongiform encephalopathy (BSE) in Washington resulted in an estimated annual loss of $7 billion to $10 billion due to suspended beef exports to overseas markets (15). While the manifestation of prion disease is not completely understood, it is known that the prion protein (PrP) plays a necessary role in prion disease development (16, 17).

1.2 The Prion Protein

1.2.1 *Structure and function of the prion protein*

After cleavage of the endoplasmic reticulum (ER) signal peptide (residues 1-22) and the glycophosphatidylinositol (GPI) anchoring signal peptide (residues 231-253), the mature human PrP consists of residues 23-230. The flexible N-terminus includes residues 23-127, which consist of an octapeptide repeat region (residues 60-91) and a hydrophobic region (residues 112-127). The remaining C-terminus of the PrP is the structured globular domain (residues 128-228) (Figure 1.1), containing three α-helices (HA, HB, and HC) and two short β-strands (S1, and S2). There are two glycosylation sites at N181 and N197, which allow the PrP to be un-, mono-, or di-glycosylated. The native cellular form of PrP (PrP^C) is bound to the extracellular side of the plasma membrane via the C-terminal GPI anchor. Currently, the function of the PrP is still poorly understood. Since PrP-knockout mice develop and behave normally without any defects, it has been suggested that PrP^C is dispensable (18). However, other findings suggests that PrP^C is implicated in copper metabolism (19) and signal transduction (20, 21). Nonetheless, PrP-knockout mice are resistant to prion diseases, suggesting that expression of PrP^C is necessary for developing prion disease.

1.2.2 *PrP^C misfolding and mechanism of prion propagation*

PrP^C can be converted into the infectious scrapie form, PrP^{Sc}, by *in vitro* methods (22), and the process of conversion can be amplified by a series of sonication and incubation with PrP^C (23). The infectivity of these recombinant PrP^{Sc} has been confirmed with animal models (23, 24). This strongly supports the “protein-only hypothesis” (25), which states that the pathogenic PrP^{Sc}, is a protein-only, self-replicating entity that causes prion disease. In order to explain the process of PrP^{Sc} replication, the seeded-nucleation mechanism (1) was proposed (Figure 1.2).

According to the seeded-nucleation hypothesis, the monomeric PrP^{C} and PrP^{Sc} are in equilibrium, with PrP^{C} being the major species. Multiple monomeric PrP^{Sc} can spontaneously self-aggregate and form a soluble PrP^{Sc} oligomer (seed). The initial rate of aggregation is slow due to the low concentration of monomeric PrP^{Sc} in equilibrium with PrP^{C}. Once formed, this soluble PrP^{Sc} oligomer recruits misfolded PrP^{C} and forms a larger PrP^{Sc} oligomer. Eventually, these large oligomers undergo unknown conformational changes to form insoluble amyloid. Fragmentation of amyloids generates more infectious PrP^{Sc} oligomers, resulting in an autocatalytic process of PrP^{Sc} propagation, which is observed in *in vitro* production of PrP^{Sc} (26). Interestingly, protein misfolding cyclic amplification (PMCA) (26), a method that exploits this autocatalytic process of PrP^{Sc} propagation, exponentially amplifies PrP^{Sc} in solution by a series of sonication and incubation of recombinant PrP^{C} . Sonication accelerates the fragmentation of larger oligomers and thus generates more infectious seeds in the solution. These infectious seeds are incubated with PrP^{C}, allowing the infectious seeds to recruit more monomeric PrP^{Sc}. The success of PMCA gives support to the seeded-nucleation hypothesis for explaining PrP^{Sc} propagation.

The seeded-nucleation hypothesis assumes that PrP^{C} is in equilibrium with monomeric PrP^{Sc}, overlooking the possibility that oligomeric PrP^{Sc} may shift this equilibrium by facilitating PrP^{C} misfolding. Given that PrP^{Sc} binds to PrP^{C} in solution (27), it is important to consider the interactions between PrP^{C} and PrP^{Sc}. It would be a significant achievement if the structure of the

PrP^C-PrP^{Sc} complex could be resolved, as such structure may reveal crucial interactions between PrP^{Sc} and PrP^C that facilitate PrP^{Sc}-induced misfolding. The nature of these interactions would be important in understanding the molecular mechanism of prion propagation.

1.3 Methods of Studying Prion Diseases

1.3.1 *Limitations of current experimental studies on prion disease*

Experimental methods such as NMR (28–30) and X-ray crystallography (31–33) have been used to resolve the structure of recombinant PrP^C. However, these high resolution techniques are incapable of resolving the structure of the toxic soluble oligomers of PrP^{Sc}, due to their heterogeneity, poor solubility and aggregation tendency. Therefore, low resolution methods have been used to date to characterize the PrP^{Sc} structure.

Low resolution methods, such as circular dichroism (CD) and Fourier-transform infrared spectroscopy (FTIR) detected higher β-sheet content in PrP^{Sc} than in PrP^C (34–36), which is mostly helical. Protein modification (with mass spectroscopy), such as lysine acetylation and tyrosine nitration can probe for solvent accessible regions of PrP^{Sc} (37, 38), but structural information obtained is limited to the amino acids that react with the probing agent, and excessive chemical modification causes undesired changes in the structure of PrP^{Sc}. Other techniques to probe for solvent exposed regions of the PrP^{Sc} include limited proteolysis (39) and hydrogen exchange mass spectroscopy (HXMS) (40). However, since both solvent accessibility and secondary structure affect the hydrogen exchange rates and proteolysis susceptible regions on the protein, making it difficult to interpret the experimental data in a structural context. Antibody epitope mapping of PrP^{Sc} is one of the relatively successful methods of detecting accessible regions of $\mathrm{PrP^{Sc}}$: antibodies that bind to $\mathrm{PrP^{Sc}}$ indicate exposed regions on the surface of $\mathrm{PrP^{Sc}}$, and antibodies that bind to both $\mathrm{PrP^{C}}$ and $\mathrm{PrP^{Sc}}$ indicate preserved $\mathrm{PrP^{C}}$ epitopes in $\mathrm{PrP^{Sc}}$.

The highest resolution structure of $\mathrm{PrP^{Sc}}$ was resolved by electron microscopy of prion rods (41, 42), indicating a three-fold symmetry arrangement of $\mathrm{PrP^{Sc}}$ subunits spanning 69 Å in diameter. In agreement with electron microscopy, X-ray diffraction studies (43) have also confirmed the symmetry and the diameter of the $\mathrm{PrP^{Sc}}$ particle. However, no atomic details of the $\mathrm{PrP^{Sc}}$ structure have been revealed.

1.3.2 *Molecular dynamics simulations of the prion protein*

An increasing number of research groups are using computational methods to study misfolding of $\mathrm{PrP^{C}}$ (44–49). Computational methods provide an attractive solution to study protein misfolding systems, as they are not limited by protein stability, solubility, and heterogeneity. Hence, the Daggett Lab uses computational methods, in particular, molecular dynamics (MD) simulations, to study protein misfolding. MD simulations use classical mechanics to simulate the atomic motion of proteins. Dynamics are resolved at the femtosecond timescale. MD simulations can, therefore, reveal the protein structural dynamics at the atomic level that are otherwise not observable with experimental methods. Using solution NMR structures as the starting point of simulations, we can predict the behavior of amyloidogenic proteins under conditions of our interest (such as low pH misfolding conditions).

The Daggett lab has performed MD simulations to characterize the misfolding of $\mathrm{PrP^{C}}$ at low pH conditions (44, 50–52). From these low pH misfolding simulations, four common structural traits have been consistently observed in the misfolded structure: 1) the three helices (HA, HB, and HC) in the globular domain are preserved; 2) HA detaches from HC; 3) the native strand S1 recruits a nonnative strand (E1) at the flexible N-terminus; and 4) the S1-HA loop becomes extended and forms the isolated strand E4. Figure 1.3 shows an example of an MD-derived misfolded structure with the two nonnative strands, E1 and E4 (Figure 1.3).

Previously we could not directly validate our MD-derived misfolded monomeric PrP^{Sc} structure with experimental findings, as there were no monomeric PrP^{Sc} isolated for experimental characterization. However, in 2014, a putative misfolded monomeric PrP^{Sc} structure was discovered by X-ray crystallography (53). In the crystal structure, the misfolded monomer was bound to a nanobody that inhibits PrP^{Sc} formation. The structure of the monomer was strikingly similar to our MD-derived misfolded monomer, in that both the crystal and the MD-derived misfolded structures have native helices preserved and a nonnative strand formed at the flexible N-terminal region of the PrP. Therefore, with some confidence, we can claim that our MD-derived misfolded PrP^{Sc} is representative of the actual PrP^{Sc} as our MD-derived misfolded structure has hallmarks of conversion. Using MD-derived misfolded structures as subunits, the Daggett lab has proposed the spiral model for oligomeric PrP^{Sc} (51, 52). The spiral model has also been validated with a variety of experimental data (54), further supporting our predicted monomeric PrP^{Sc} structure from MD simulations.

1.4 Spiral Model for Oligomeric PrP^{Sc}

The spiral model was generated from MD-derived misfolded PrP structures (51). The monomers in the spiral model are docked together, such that the oligomerization sites, the E1 and E4 strands, of each monomer form the docking interface between neighboring subunits. Figure 1.4 illustrates the procedure of constructing the spiral model, with monomers arranged in a three-fold symmetric spiral. The resulted model agrees well with a variety of experiments (54). As new structural data become available, it is important to incorporate these new experimental observations into the spiral model and make revisions accordingly.

It is important to keep in mind that the soluble oligomers are the major toxic species, not fibrils (55), and that the spiral model is a model for soluble oligomers of PrP^{Sc}. Amyloidogenic proteins are known to form fibrils with cross-β structure (56). However, PrP^{Sc} soluble oligomers do not have a significant amount of cross-β structure. This is demonstrated by Thioflavin T (a fluorescent dye for cross-β structures) binding studies (57) indicating that soluble oligomers have weak binding affinity toward Thioflavin T. Another study monitoring both the size of PrP^{Sc} soluble oligomers and the fluorescent signal of Thioflavin T simultaneously confirmed that soluble oligomers of PrP^{Sc} weakly bind to Thioflavin T (58). However, the increase in β-sheet content is evident in these soluble oligomers as indicated by CD (59–61) and FTIR spectroscopy (62). Therefore, these β-sheet rich soluble oligomers are expected to undergo conformational changes, ultimately reaching a cross-β structure at the fibril state. Although the exact conformational differences between the soluble oligomers and fibrils are not known, the spiral model has flexible loop regions (S1-HB loop and HA-S2 loop) that may facilitate conformational changes to achieve a cross-β architecture upon fibrillation.

1.5 This Work

I began my studies by performing and analyzing MD simulations of the human PrP pathogenic mutations Y218N and E196K, along with the wildtype human PrP. I proposed that the two different pathogenic PrP mutants, despite their different misfolding mechanisms, achieved common traits of a misfolded structure. This study was published in the journal *Prion* (63) and is included as Chapter 2. Other than human PrP, I have also researched the misfolding mechanism of bovine PrP. I have identified important polar and hydrophobic contacts that contribute to the increase in β-sheet content of the misfolded bovine PrP structures. This study was published in the journal *Biomolecules* (64) and is included as Chapter 3.

Due to improvements in computational speed, our lab has been able to perform simulations of the PrP^C in complex systems, including lipids, GPI anchors and glycans. I performed in-depth analysis on the human membrane-bound PrP^C MD simulations, which were previously performed by Dr. Marc van der Kamp and Dr. Heidi Koldsø. I proposed a mechanism by which the PrP^C can shield its aggregation sites from exogenous PrP^{Sc}, thus deterring PrP^{Sc}-induced misfolding. This work is presented in Chapter 4.

In Chapter 5, I compared the three prevalent PrP^{Sc} models by evaluating these models with current experimental data on PrP^{Sc} soluble oligomers. The spiral model is in good agreement with a variety of experimental data. Given our confidence in the spiral model, in the final Chapter 6, I combined my previous findings in both human and bovine PrP and constructed a membrane-bound human PrP^C system with an approaching bovine PrP^{Sc} (a hexameric spiral model). This system has more than 277,000 atoms and this is to our knowledge the first MD simulation for studying the PrP^C-PrP^{Sc} interactions in a physiological environment.

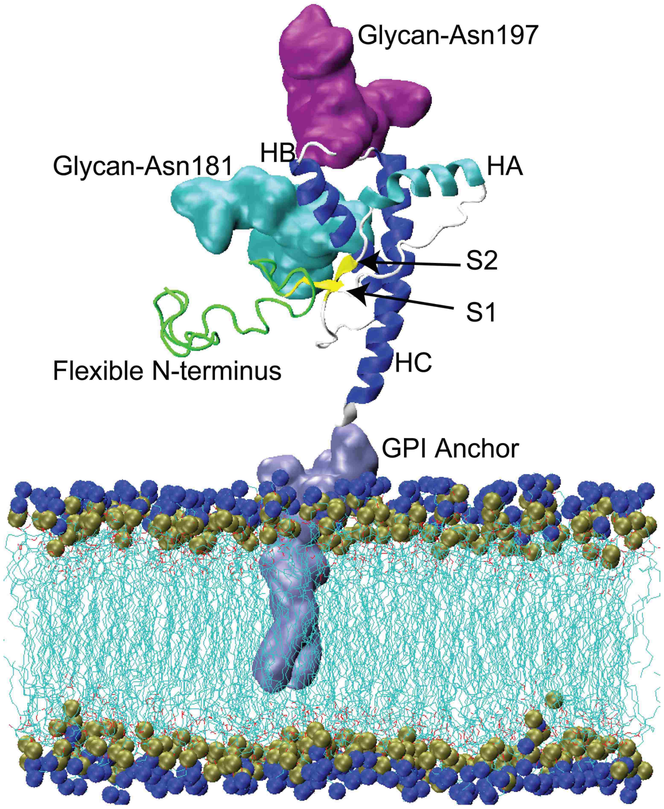

Figure 1.1 PrP^C membrane-bound via GPI anchor.

Residues 90-230 of the human PrP and its secondary structural elements are shown: flexible N-terminus (residues 90-127) in green; loop regions in white; helices HB and HC in blue; HA in cyan; native strands S1 and S2 in yellow. Glycans are attached at N181 (cyan) and N197 (magenta) of the PrP. GPI anchor (gray) is embedded in the membrane and linked to the C-terminal of the HC.

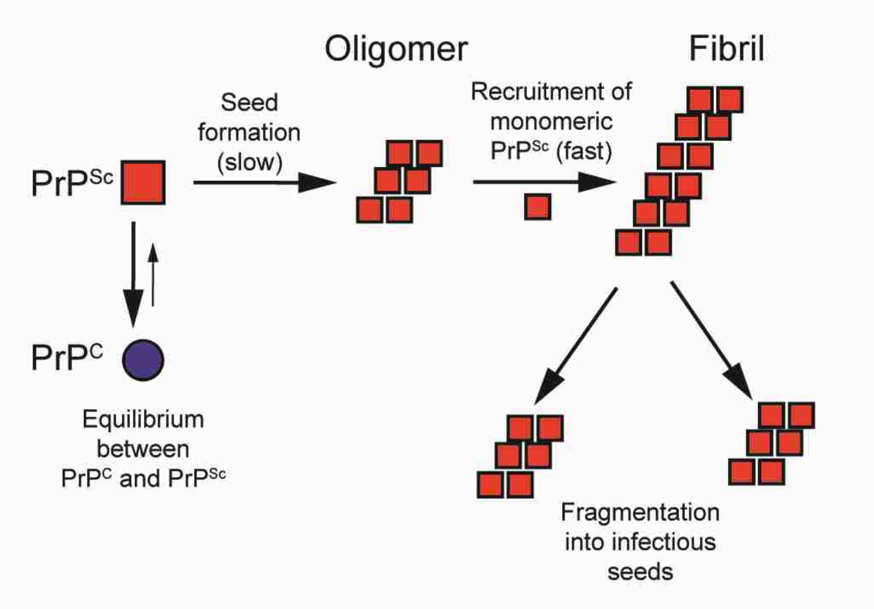

Figure 1.2 Illustration of the seeded-nucleation mechanism.

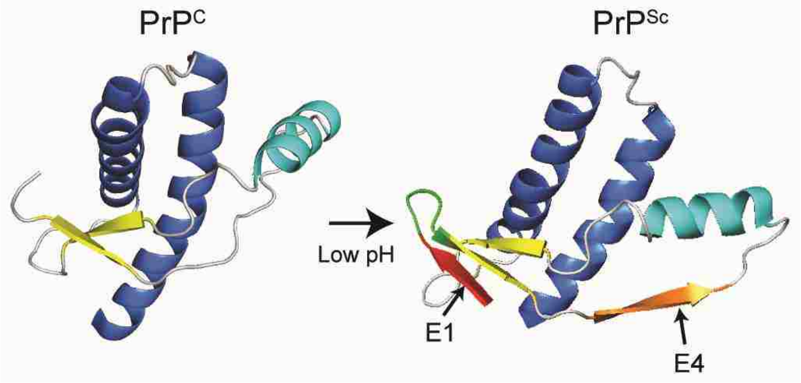

Figure 1.3 Example of an MD-derived monomeric PrP^{Sc}.

Human PrP^C structure was obtained from NMR (PDBID: 1QLX) and low pH MD simulation generated a misfolded structure of the human PrP. Two nonnative strands, E1 (red) and E4 (orange) were formed.

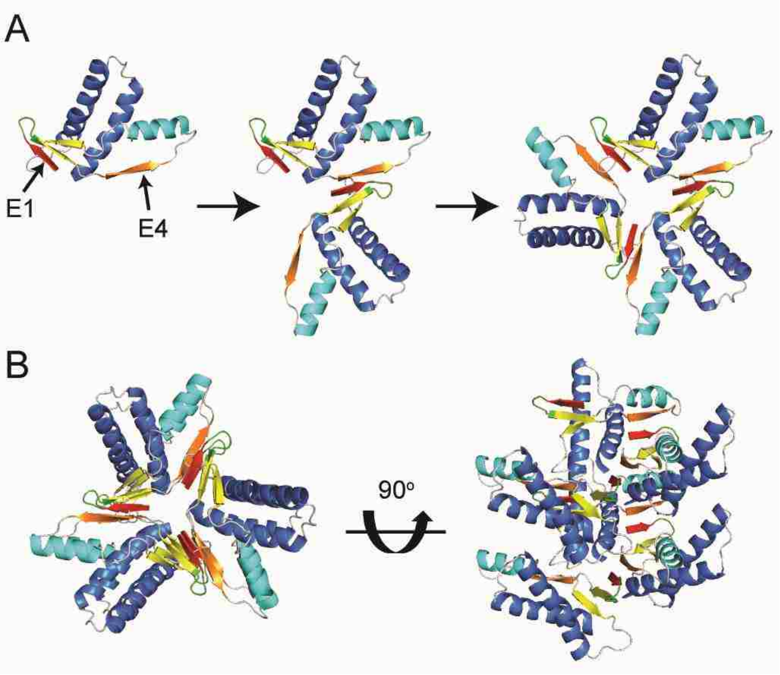

Figure 1.4 The spiral model.

(A) Using the MD-derived monomeric human PrP^{Sc} structure, a trimeric unit of the spiral model was constructed by docking the E1 strand (red) against E4 strand (orange). (B) Top view and side view of the hexameric spiral model are shown.

Chapter 2

HUMAN PRION PROTEIN PATHOGENIC MUTATIONS: Y218N & E196K

2.1 Summary

Prion diseases are caused by misfolding and aggregation of the prion protein (PrP). Pathogenic mutations such as Y218N and E196K are known to cause Gerstmann-Sträussler-Scheinker syndrome and Creutzfeldt-Jakob disease, respectively. Here we describe molecular dynamics simulations of these mutant proteins to better characterize the detailed conformational effects of these sequence substitutions. Our results indicate that the mutations disrupt the wild-type native PrP^C structure and cause misfolding. Y218N reduced hydrophobic packing around the X-loop (residues 165-171), and E196K abolished an important wild-type salt bridge. While differences in the mutation site led PrP mutants to misfold along different pathways, we observed multiple traits of misfolding that were common to both mutants. Common traits of misfolding included: 1) detachment of the short helix (HA) from the PrP core; 2) exposure of side chain F198; and 3) formation of a nonnative strand at the N-terminus. The effect of the E196K mutation directly abolished the wild-type salt bridge E196-R156, which further destabilized the F198 hydrophobic pocket and HA. The Y218N mutation propagated its effect by increasing the HB-HC interhelical angle, which in turn disrupted the packing around F198. Furthermore, a nonnative contact formed between E221 and S132 on the S1-HA loop, which offered a direct mechanism for disrupting the hydrophobic packing between the S1-HA loop and HC. While there were common misfolding features shared between Y218N and E196K, the

differences in the orientation of HB and HC and the X-loop conformation might provide a structural basis for identifying different prion strains.

2.2 Introduction

Prion diseases, or transmissible spongiform encephalopathies, are neurodegenerative diseases that include Creutzfeldt-Jakob disease (CJD), Gerstmann-Sträussler-Scheinker Syndrome (GSS) and fatal familial insomnia. Human prion diseases are extremely heterogeneous in terms of their clinical presentations and biomolecular characteristics (65–67). Different prion diseases can only be identified upon examination of the prion protein (PrP) aggregates in neuronal tissues (68, 69). Despite differences in neuropathology, all prion diseases share the same causative agent, which is the scrapie form of the prion protein, PrP^{Sc}. The normal cellular prion protein (PrP^{C}) is innocuous, but it may undergo misfolding and convert into PrP^{Sc} (70, 71). which is toxic and infectious. Currently, the PrP^{Sc} conversion mechanism is not well understood, nor is there a clear understanding of how different types of prion diseases occur.

PrP^{C} is expressed in neuronal cells as a membrane bound protein with two glycosylation sites. The N-terminus (residues 23-127) is highly flexible, but the C-terminal globular domain (residues 128-228) is structured in various species (29, 30, 72, 73). The C-terminal globular domain consists of three helices (HA, HB, and HC) and two short β-strands (S1 and S2) (Figure 1.1). At the C-terminus, there is a glycosylphosphatidylinositol (GPI)-anchor that tethers the PrP^{C} to the cell membrane. Transgenic mice expressing full-length mouse PrP without the GPI anchor produces mostly unglycosylated PrP (74, 75). In addition, these mice are susceptible to prion diseases (74). This suggests that the protein-only portion of PrP (without glycosylation and the GPI anchor) is sufficient for PrP^{Sc} formation in mice. Proteinase K digestion of PrP^{Sc} aggregates in human patients indicate that residues ~90-230 are protected and thus these residues are considered to be the core of PrP^{Sc} (76). The PrP fragment with residues 90-230 (PrP90-230) contains critical residues in the N-terminus that are required for PrP^{Sc} conversion (77–80). *In vivo* studies have also demonstrated that recombinant fibrils of PrP90-230 in mouse are infectious (81). These findings suggest that PrP90-230 is the core of PrP^{Sc} that carries infectivity.

Nearly all (>30) of the known single point pathogenic mutations in the human PrP are within residues 90-230 (82–85). More than 20 of these single point pathogenic mutations are spread throughout the HB and HC regions. The lack of convergence into a hot spot of mutations makes it difficult to rationalize the mutation-induced misfolding pathway, as different mutations have different local effects on PrP dynamics. While several unfolding studies indicate that single point pathogenic mutations destabilize the PrP^{C} structure, some mutations increase or have little effect on the thermodynamic stability of PrP^{C} (86, 87). Molecular dynamics (MD) studies of pathogenic mutations in the PrP hydrophobic core (88) have identified misfolded structures in agreement with earlier MD studies of the human wild-type (WT) PrP using low pH to trigger misfolding (50, 51).

Disease-associated mutations Y218N (89) and E196K (90) cause GSS and familial CJD, respectively. These two mutants are different in terms of the amino acids mutated, and the mutation sites are separated by ~29 Å. Here, we used MD simulations to study the PrP dynamics of these two disease-associated mutants. We observed common misfolding events in agreement with previous MD studies of other pathogenic mutants (88). However, certain structural features and the pathways of misfolding were different for Y218N and E196K. The structural differences provide us with a structure-based hypothesis regarding the formation of different prion strains.

2.3 Results

2.3.1 *Major conformational change in the globular domain*

The Cα root-mean-square-deviation (RMSD) of the globular domain was used to monitor conformational changes in the structured region of PrP (Figure 2.2). At the end of 50 ns, Y218N simulations 1 and 3 reached much higher Cα RMSDs (~3.5 Å) than that of the average from the WT simulations (1.9 Å). The Cα RMSD of simulation 2 at the end was about 2.5 Å, which was ~0.5 Å higher than that of the average WT simulations. Previous low pH MD simulations of human PrP have shown that the HA helix is highly mobile and can contribute to the high globular Cα RMSD (44). To monitor the HA movement with respect to the core of the protein, the Cα RMSD of HA was measured (Figure 2.2) by using the stable core domain (residues 174-186 and 200-219) for alignment. The increasing Cα RMSD of HA in simulations 1 and 3 correlated with the increasing globular Cα RMSD. Simulation 2 had relatively low Cα RMSD of HA compared to that of the other simulations and the average WT Cα RMSD. Such Cα RMSD trend indicates that simulation 2 preserved the native HA orientation with respect to the core unlike the other two simulations of Y218N. The globular domain Cα RMSD of E196K was similar to that of the WT. The Cα RMSD of HA in E196K simulations stayed close to the average WT value, in contrast to Y218N. However, there was an increase in Cα RMSD of HA in E196K simulation 1 after 48 ns, which indicated a sudden HA movement with respect to the core.

2.3.2 *HA detachment from core in mutant simulations*

HA detached from the protein core in simulation 3 of Y218N (Figure 2.3A). The hydrophobic contacts between S1-HA loop and HC (42 atom contacts) in the starting structure were the main attractive force that held HA and HC together. Within the first nanosecond, D202 formed a hydrogen bond with Y149. At 5 ns, a rare hydrogen bond between S132 and E221 formed. This contact was only observed in WT simulations 0.57% of the time. At 18 ns, HA moved away from HC, which occurred ~13 ns after the formation of the S132-E221 nonnative hydrogen bond. The HA movement was characterized by three events that happened cooperatively: 1) a change from 3_{10}-helix to α-helix at the C-terminus of HA (Figure 2.3B); 2) the loss of a hydrogen bond between D202 and Y149 (Figure 2.3C); and 3) the loss of hydrophobic contacts between the S1-HA loop and HC (Figure 2.3D). HA remained in this nonnative position for the rest of the simulation.

The starting structure of E196K had only minute differences from Y218N (Cα RMSD = 0.140), except that the mutant E196K had a new salt bridge between K196 and D202. The WT salt bridge between E196-R156 was abolished due to the E196K mutation. The hydrogen bond between D202 and Y149 formed within the first nanosecond of the simulation. After 48 ns in simulation 3, HA detached from HC (Figure 2.4A**)** and was characterized by the three aforementioned events (Figure 2.4B, C and D). The nonnative salt bridge K196-D202 was particularly prominent in E196K simulation 3 and lasted throughout the course of the simulation (Figure 2.4C). Since the D202 side chain was occupied with K196, and the side chain of residue 196 became positively charged, R156 lost both of its WT salt bridge partners (residue 202 and 196). The salt bridge between D202 and R156 was occupied on average 1.84% of the time from

25-50 ns of the E196K simulations, unlike WT and Y218N (36% and 59% respectively). The remaining neighbors available for interacting with R156 were on HA. In particular, the side chain of N153 was available to interact with R156 (Figure 2.4C).

2.3.3 *Hydrophobic core packing and F198 solvent exposure*

Both mutants had a more exposed hydrophobic core than that of WT, except for one simulation of E196K (Figure 2.5). Exposure of the hydrophobic core was mainly attributed to HA movement, X-loop hydrophobic packing and also the solvent exposure of F198. The average solvent accessible surface area (SASA) of F198 in WT was only 34 Å^2, while some of the mutant simulations achieved >150 Å^2 at some time points. F198 can be roughly classified into three conformational states by its solvent exposure: native state (SASA ~20 Å^2) with F198 side chain buried between HB and HC; semi-exposed state (SASA ~80 Å^2) with one side of the phenyl group exposed to solvent; and, fully exposed state (SASA ~140 Å^2) with the side chain fully exposed to solvent. These conformations of F198 are illustrated in Figure 2.6 for WT, Y218N and E196K.

In WT simulations, F198 was mostly in its native state and occasionally visited the semi-exposed state. The backbone conformation of F198 was stabilized by its neighbor T199, which formed a capping box interaction (91) with D202 at the N-terminus of HC (Figure 2.6A). The WT native salt bridge between E196 and R156 also stabilized the backbone conformation of the HB-HC loop. This WT native salt bridge was preserved in Y218N (Figure 2.6B). However, for E196K, the mutation at residue 196 abolished the WT native salt bridge and directly triggered a mechanism that destabilized the conformation of F198 (Figure 2.6C). K196 and D202 formed a salt bridge in the starting structure. This new salt bridge caused the side chain of K196 to clash with F198. At 1.6 ns, the F198 side chain reached the semi-exposed state due to steric repulsion with K196. As R156 formed another salt bridge with D202 at 17.2ns, K196 was pushed out of the protein core and the side chain of F198 became fully exposed. The backbone conformation of the HB-HC loop was vulnerable at the very beginning, because K196 formed a salt bridge with D202, thereby preventing the formation of the capping box interaction between T199 and D202.

Y218N simulations also had a disrupted F198 hydrophobic pocket, but via an indirect mechanism, which involved an increase in the interhelical angle between HB and HC (Figure 2.7A). In general, Y218N had a larger interhelical angle than that of WT and E196K (Figure 2.7B). The 25-50 ns average WT, E196K and Y218N HB-HC interhelical angles were 131^o, 133^o and 140^o, respectively. In simulation 1 of Y218N, the interhelical angle increased at the beginning. The C-terminus of HB and N-terminus of HC approached each other. F198 was pushed to the semi-exposed state by HB and HC at 0.2 ns. The increase in the interhelical angle also accommodated backbone conformational changes within the HB-HC loop, which allowed F198 to become fully exposed at 18 ns. Interestingly, the native WT salt bridge between E196 and R156 was preserved in Y218N. Despite this, the capping box interaction between T199 and D202 was lost. The difference in the salt bridge network and interhelical angles between E196K and Y218N demonstrated the different pathways for disrupting of the hydrophobic packing around F198 in these two mutants.

2.3.4 *Loss of X-loop hydrophobic packing in Y218N*

While E196K and WT displayed comparable compactness at the X-loop, Y218N lost significant X-loop packing interactions as a result of the mutation (Figure 2.8A). To measure the hydrophobic packing at the X-loop, the number of atom contacts, consisting of a list of bulky residues around the X-loop (including residue Y/N218 and M166), were quantified for all simulations (Figure 2.8B). Both WT and E196K had about 80 atom contacts and M166 was always buried between HB and HC. Y218N tended to have less atomic contacts compared to WT and E196K. Simulation 2 of Y218N had an exceptionally low number of atom contacts (~28 contacts). This was caused by the change in the X-loop conformation at 1.1 ns such that M166 became exposed to solvent.

2.3.5 *Nonnative strand at the flexible N-terminus.*

A nonnative strand (denoted as E1) at the flexible N-terminus formed (Figure 2.9A) within the first 3 ns of both Y218N and E196K simulations. Once formed, E1 was stable throughout the rest of the simulation (Figure 2.9B). E1 formed independently of other conversion events (e.g. the large HA movement and the disrupted hydrophobic core). E1 used the native strand, S1, as a nucleation site and formed ≥4 backbone hydrogen bonds with S1. There were stable β-bulges in E1, which formed short, α-strand-like backbone conformations that are believed to be early steps of amyloidosis (92, 93). The residues that participated in E1 formation were in the range of 117-124, which overlap with critical amyloidogenic sequences in the N-terminus, such as the 112-AGAAAAGA-119 palindrome (77) and the neurotoxic peptide 106-126 (78, 94).

2.4 *Discussion*

Using MD simulations, we studied the effects of two pathogenic mutants Y218N and E196K on the structure and dynamics of the human PrP. The mutation sites caused local differences between the mutants. The E196K mutation eliminated the WT salt bridge E196-R156. The Y218N mutation resulted in a loss of hydrophobic packing around the X-loop region. Despite local differences around the mutation sites, the two mutants shared common traits of misfolding: 1) HA detached from PrP core; 2) F198 left its native position and became solvent exposed; and 3) the flexible N-terminus formed a new strand. Here we have shown that each mutant has a unique pathway for triggering common misfolding events.

2.4.1 *Repositioning of the HA helix*

In mutant Y218N simulations, the mutation caused HC to bend towards the S1-HA loop; E221 then formed a stable contact with S132 on the S1-HA loop (Figure 2.3). The S132-E221 contact was only scarcely (< 1% simulation time) populated in WT simulations. This nonnative contact offered a pathway for the mutation to affect the S1-HA loop conformation. The change in the S1-HA loop conformation disrupts the hydrophobic packing between the S1-HA loop and HC, which therefore destabilizes HA. The importance of the hydrophobic packing between HC and the S1-HA loop has been verified by mutational studies on PrP: polar residue mutations of M206 and M213 reduce thermal stability and enhance amyloidogenicity of PrP^C (95).

The native WT salt bridge E196-R156 tethers HA to the protein core. This salt bridge, which is present in NMR structures of human PrP (28, 73), is also highly populated in several MD studies (96–99). Low pH MD simulations of human PrP resulted in loss of the E196-R156 salt bridge and HA detachment from HC (44). The E196K mutation abolished the native WT salt bridge due to the charge repulsion between K196 and R156. However, the effect of the mutation was not observed immediately. Hydrophobic packing between the S1-HA loop and HC, and also the hydrogen bond between D202 and Y149, held HA intact until later in simulation when HA detached from HC (Figure 2.4).

The stability of HA can be influenced by low pH (100), chemical denaturants (101), temperature and pressure (102). Our previous MD studies first suggest that HA significantly changes its position at low pH (44, 50, 51, 96, 103). Furthermore, two other groups have also used computational methods and found HA to be significantly repositioned (104, 105). HA repositioning has also been observed in MD simulations of pathogenic PrP mutants (88). These studies suggest that the repositioned HA conformation is permissible and that it can be induced under destabilizing conditions. An engineered disulfide bond (by double-cysteine mutants) that tethers HA to HC prevents formation of PrP oligomers (106) and fibrils in *in vitro* experiments (107). *In vivo* cell studies indicate that these double-cysteine mutants do not propagate PrP^{Sc} formation (107). These experimental findings suggest that separation of HA and HC is necessary for oligomerization and propagation of PrP^{Sc}, and thereby support our computational observation that repositioning of HA is an important hallmark for PrP^{Sc} conversion.

2.4.2 *Exposure of F198 and disruption of the hydrophobic pocket between HB and HC*

The E196K mutation had a direct impact on the hydrophobic core of the PrP (Figure 2.6C). F198 became fully exposed due to its steric repulsion with K196. The N-capping box interaction at HC was lost; furthermore K196 formed a stable salt bridge with D202 which prevented the side chain hydrogen bond between D202 and T199. Loss of the capping box interaction allowed for more conformational freedom of the HB-HC loop (residues 194-199), thus facilitating disruption of the F198 hydrophobic pocket.

Y218N also adapted a different HB-HC loop conformation that exposed F198 to the solvent, but by a very different mechanism. The Y218N mutation resulted in a significant loss of hydrophobic packing around the X-loop (Figure 2.8). The mutation also caused a significant increase in the HB-HC interhelical angle (Figure 2.7), so that HB and HC became more antiparallel to each other. As the interhelical angle increased, the hydrophobic pocket that contained F198 was disrupted and so was the HB-HC loop. The HB-HC loop adopted a nonnative conformation and F198 became exposed to solvent.

Riek et al. previously predicted that a pathogenic mutation, F198S, introduces a destabilizing void volume in the PrP core (91). Subsequent thermodynamic studies are in agreement with this prediction (86), and MD studies have also indicated that F198S destabilizes PrP^C (88, 108, 109). *In vitro* results confirmed that F198S has a higher tendency to misfold (110, 111). From these studies of F198S, we conclude that the loss of hydrophobic packing around F198 facilitates misfolding. Denaturation studies indicate that stable NOE contacts exist between F198-M206 and F198-Y157 in bovine PrP (111), which confirms the stabilizing effect of F198 in the native state. The binding of a PrP^{Sc}-specific antibody to residues 187-206 suggests that the loop between HB and HC adapts a misfolded/altered conformation in PrP^{Sc} (112). Thus, change in the HB-HC loop conformation and exposure of F198 to solvent appears to be another likely hallmark for PrP^{Sc} conversion.

2.4.3 *Putative aggregation sites: the flexible N-terminus and the S1-HA Loop*

In both mutants, we observed significant movement of HA and the S1-HA loop. The number of hydrophobic contacts between the S1-HA loop and HC were significantly reduced as HA detached from HC. Mutation studies on the PrP have confirmed that the hydrophobic packing between the S1-HA loop and HC are crucial for the native PrP^C thermal stability (95, 113). The loss of hydrophobic packing between HC and the S1-HA loop allowed higher conformational flexibility for the S1-HA. High pressure unfolding experiments performed on the PrP have also identified that residues I139, H140, and F141 in the S1-HA loop have a higher conformational variability/heterogeneity (114), which might be related to the early steps of misfolding. According to studies on prion peptic fragments, the sequence of residues 136-140 is critical for aggregation (115). In particular, alanine mutations at hydrophobic residues P137 and I139 completely halted conversion to PrP^{Sc}. This indicates that the hydrophobic residues in the S1-HA loop play an important role in misfolding and aggregation. Abalos et al. further hypothesized that residues 136-140 participate in the PrP^{Sc}-PrP^C binding interface and also the process of misfolding (115). This hypothesis is in agreement with our first simulations of PrP^C conversion (50) and our later protofibril models (51, 54). We hypothesize that, during PrP^{Sc} oligomerization, the S1-HA loop forms a new strand by docking with a neighboring PrP^{Sc} unit. The new strand at S1-HA loop is one of the putative aggregation site denoted as E4 (51).

In vivo experiments show that the flexible N-terminus in PrP^C is required for extracellular β-oligomers to induce cellular toxicity (116, 117). *In vitro* studies indicate that residues from the flexible N-terminus are critical for aggregation, such as residues 98-110 (115), the 112-AGAAAAGA-119 palindrome (77), neurotoxic peptide 106-126 (78, 94), polybasic region (residues 94-110) (80), and the mini prion 106 (79, 118). Interestingly, there is a pathogenic Y145Stop mutant (119, 120), which suggests that a neurotoxic conformation is encoded in the PrP residues before HA. Our simulations detected the formation of the E1 strand at the flexible N-terminus, which has been observed in previous MD simulations of other pathogenic mutants (88, 121) and also under acidic pH conditions (44, 50, 51). These data suggest that the N-terminus is critical to the conversion process and must be included in simulation studies of PrP. In our spiral model for PrP^{Sc} soluble oligomers (51), the PrP^{Sc} monomeric units have a nonnative strand formed at the N-terminus, which is docked to E4 (the S1-HA loop). We hypothesize that the nonnative strand formed at the N-terminus is an aggregation site for PrP^{Sc}.

2.4.4 *Structural basis for different prion strains*

Although both Y218N and E196K differ only by two residues in their primary sequences, they share significant differences in the X-loop conformation and HB-HC interhelical angle. A single point mutation (D167S) changing the structure of the X-loop in mouse PrP can cause prion disease (122), but the relationship between structure, sequence and disease phenotype is still obscure. Previously, we have proposed that the differences in X-loop conformations provide a structural basis for prion disease resistance (123). This is likewise applicable to explain the differences between Y218N and E196K, as they cause two different prion diseases, GSS and familial CJD, respectively. The spiral model (51) places the X-loop between PrP monomer interfaces; the HB-HC helical orientation also plays a significant role in the complementarity of the PrP^{Sc} intermolecular binding surface. Antibody-binding studies (124, 125) and X-ray diffraction (43, 126) have confirmed that distinct prion strains have different conformations.

While it is premature to conclude that the differences in the X-loop conformation and HB-HC orientation would cause different pathogenesis, the significant structural differences between Y218N and E196K supports the hypothesis of a structural basis for different prion strains.

2.5 Materials and Methods

The NMR structure of human PrP (73), PDB code 1QLX, was used as the starting structure for the globular domain (residues 128-228). Since residues 90-230 the critical core of PrP^{Sc} (76), and the PrP fragment with residues 90-230 (PrP90-230) contains critical residues in the N-terminus that are required for PrP^{Sc} conversion (77–79), the missing flexible N-terminus (residues 90-127) and residues 229-230, were manually built as described previously (44). Briefly, limited NOE restraints were used to model residues 90-127 such that it can move freely in any direction with respect to the globular domain. The protocol for generating starting structure of PrP mutants was described previously (121). First, the side chain at the mutation site was replaced, using our rotamer library (127) built from the Dynameomics database (128). Multiple structures with different rotamers at the mutation site were generated, followed by 100 steps of steepest descent minimization on all side chains. Finally, the lowest energy structure was selected as the starting structure.

Simulations were performed at neutral pH and 310 K. The protonation states of histidine residues were consistent with our previous study at neutral pH (44), i.e. only H144 was protonated on Nδ1; all other histidine residues were protonated on Nε2. All side chains of aspartate and glutamate residues were negatively charged. Side chains of lysine and arginine residues were positively charged. MD simulations were performed using *in lucem* Molecular

Mechanics (*il*mm) (129), which uses the Levitt et al. force field (130) and F3C water model (131). The NVE microcanonical ensemble was employed. Previously developed protocols were used to prepare and perform the simulations (132). Triplicate simulations of 50 ns each were generated for each mutant. Four simulations of 50 ns were generated for WT. A different random number seed was used for each simulation to generate replicates to improve sampling.

Most of the analysis methods have been described previously (88). The Cα RMSD of the globular domain was aligned to and calculated for residues 128-228. The Cα RMSD of HA was aligned to the stable core (residues 174-186 and 200-219) and calculated for residues 144-156. SASA was calculated by *il*mm using the Lee and Richards method (133). Secondary structure analysis was performed by using the DSSP (Define Secondary Structure of Proteins) algorithm (134) but with additional definitions (52). Heavy atoms were considered to be in contact when they are less than 4.6 Å apart, or 5.4 Å apart if both heavy atoms were carbon atoms. Hydrogen bonds were defined by a 2.6 Å distance between a hydrogen atom and an acceptor and the donor-H-acceptor angle must be within 45° of linearity. In order to calculate interhelical angle between HB and HC, Cα atoms of residues 179-194 (on HB) and 200-214 (on HC) were fit to two vectors and the angle between the two vectors was measured.

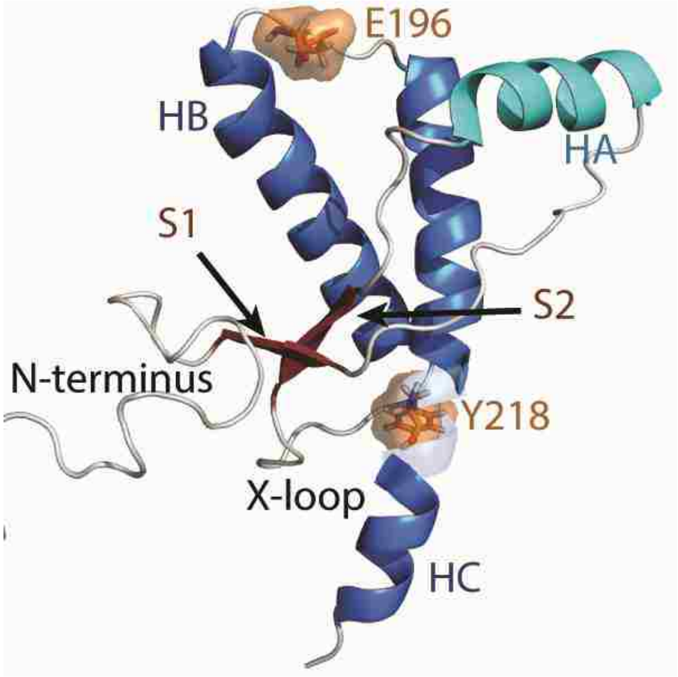

Figure 2.1 Native structure of the human PrP

Starting structure for WT PrP MD simulations. Structure of residues 128-228 was obtained from PDB 1QLX. Structure of the flexible N-terminus (residues 90-127), and C-terminus (residues 229-230) were constructed manually. Helices HB and HC are colored in blue and HA is colored in cyan. Native strands (S1 and S2) are colored in dark red. The remaining loop regions are in gray. Mutation sites are indicated in orange.

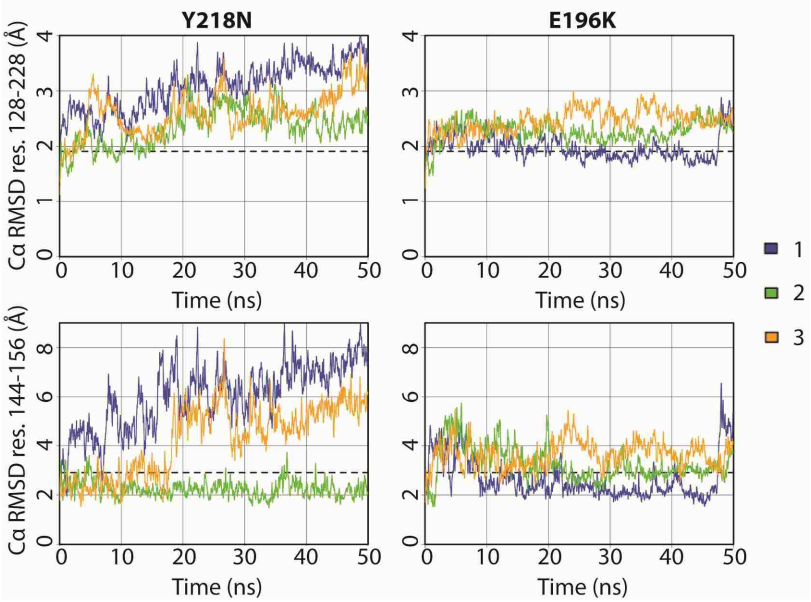

Figure 2.2 Cα RMSD of the globular domain (residues 128-228) and HA (residues 144-156) for Y218N and E196K simulations (three simulations of each)

The globular domain was aligned for calculating Cα RMSD residues 128-228, and the core domain (residues 174-186 and 200-219) was aligned for calculating Cα RMSD residues 144-156. Window averages (100 ps) of the Cα RMSD are shown for all mutant simulations. The average Cα RMSD value over the last 25 ns of the four WT simulations are shown as dashed lines.

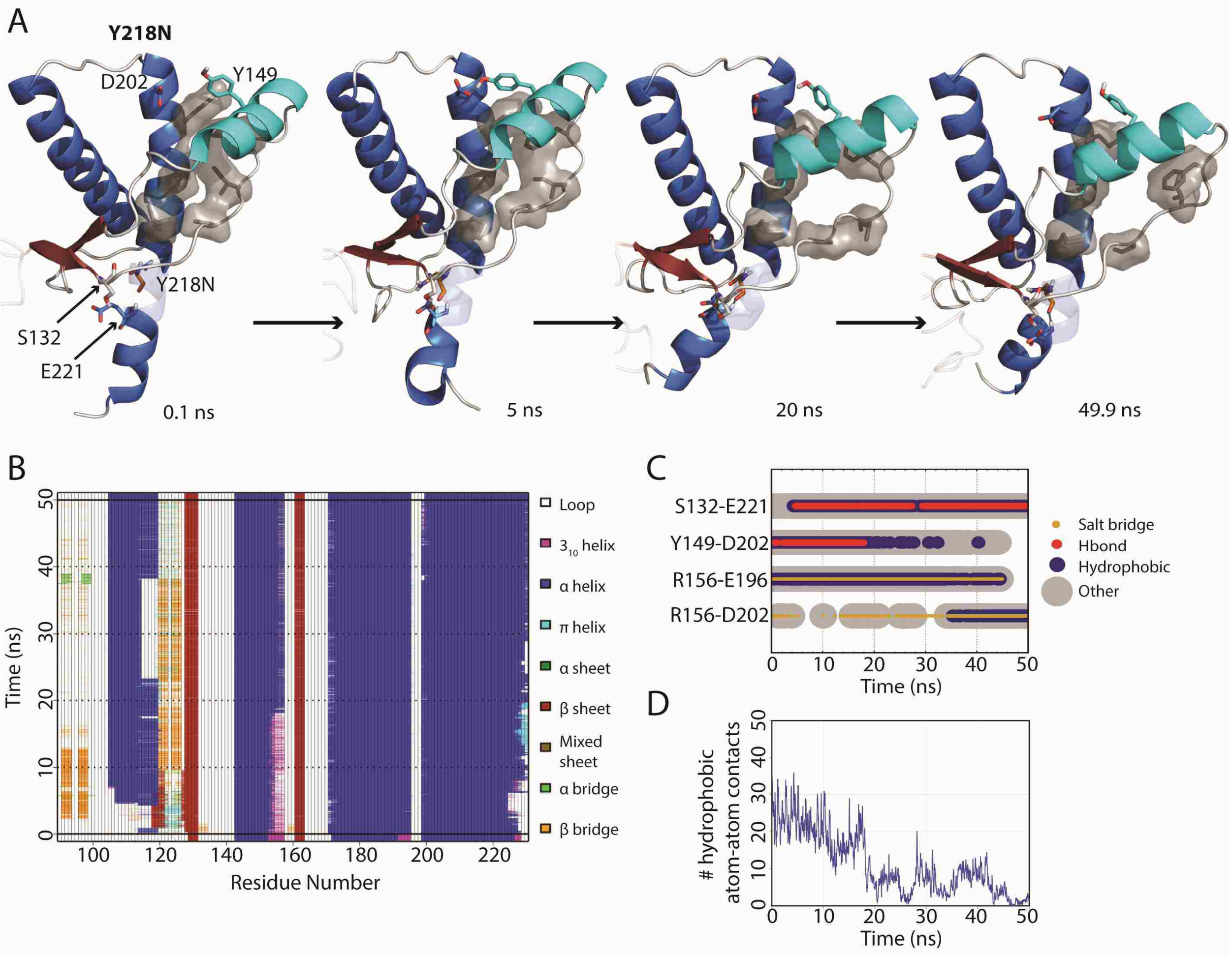

Figure 2.3 HA detachment from the PrP core in Y218N simulation 3

(A) Structures taken at 0.1, 5, 20, and 40.9 ns of the simulation. Residues S132, Y149, D202 and E221 are shown as sticks. Residues shown in gray sticks with a transparent surface are P137, I139, F141 on the S1-HA loop and M205, V209, M213 on HC. (B) DSSP analysis on the protein secondary structure. (C) Contacts between pairs of listed residues over 50 ns in simulation. (D) Window average (100 ps) of the number of contacts between residues P137, I139, F141 on the S1-HA loop and M205, V209, M213 on HC.

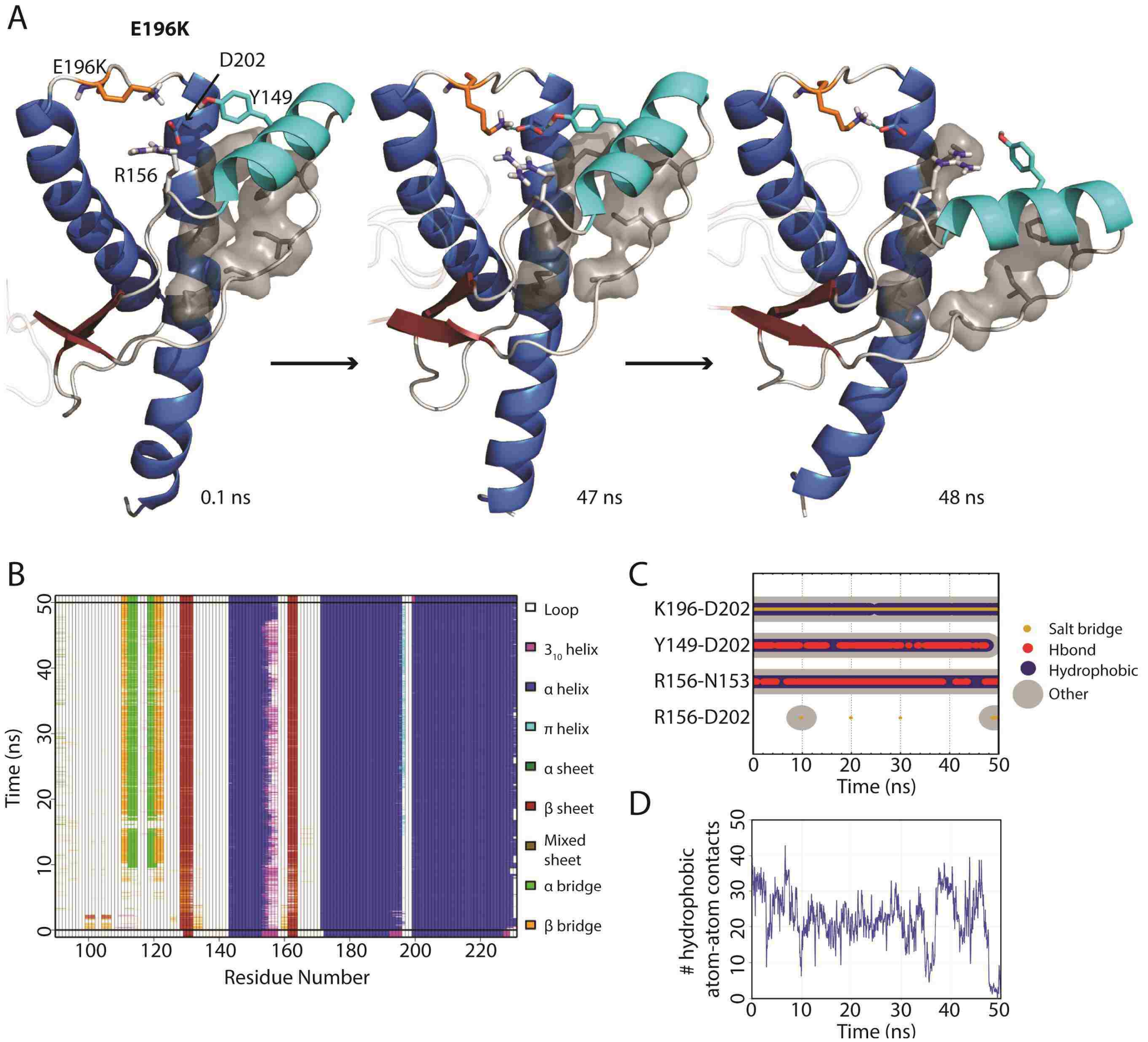

Figure 2.4 HA detachment from the PrP core in E196K simulation 1

(A) Structures taken at 0.1, 47, and 48 ns. Residues D202, Y149, R156 and K196 are shown as sticks. Residues shown in gray sticks with a transparent Van der Waals radius are P137, I139, F141 on the S1-HA loop and M205, V209, M213 on HC. (B) DSSP analysis on the protein secondary structure. (C) Contacts between pairs of listed residues over 50 ns in simulation. (D) Window average (100 ps) of the number of contacts between residues P137, I139, F141 on the S1-HA loop and M205, V209, M213 on HC.

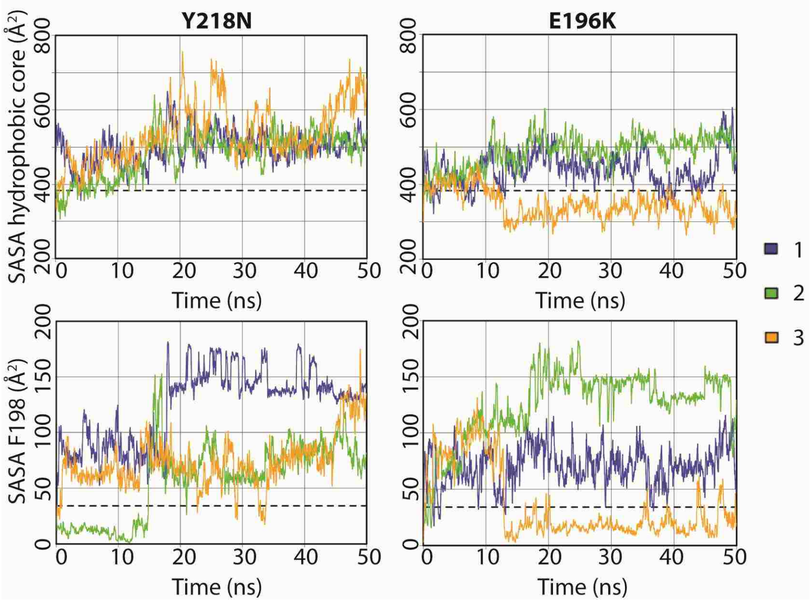

Figure 2.5 Solvent accessible surface area of the hydrophobic core and F198 in the Y218N and E196K simulations

The hydrophobic core was defined as residues 134, 137, 139, 141, 158, 161, 175, 176, 179, 180, 184, 198, 203, 205, 206, 209, 210 and 213–215. Window averages (100 ps) of the SASA are shown for all mutant simulations. The average SASA values over the last 25 ns of the WT simulations are shown in dashed lines.

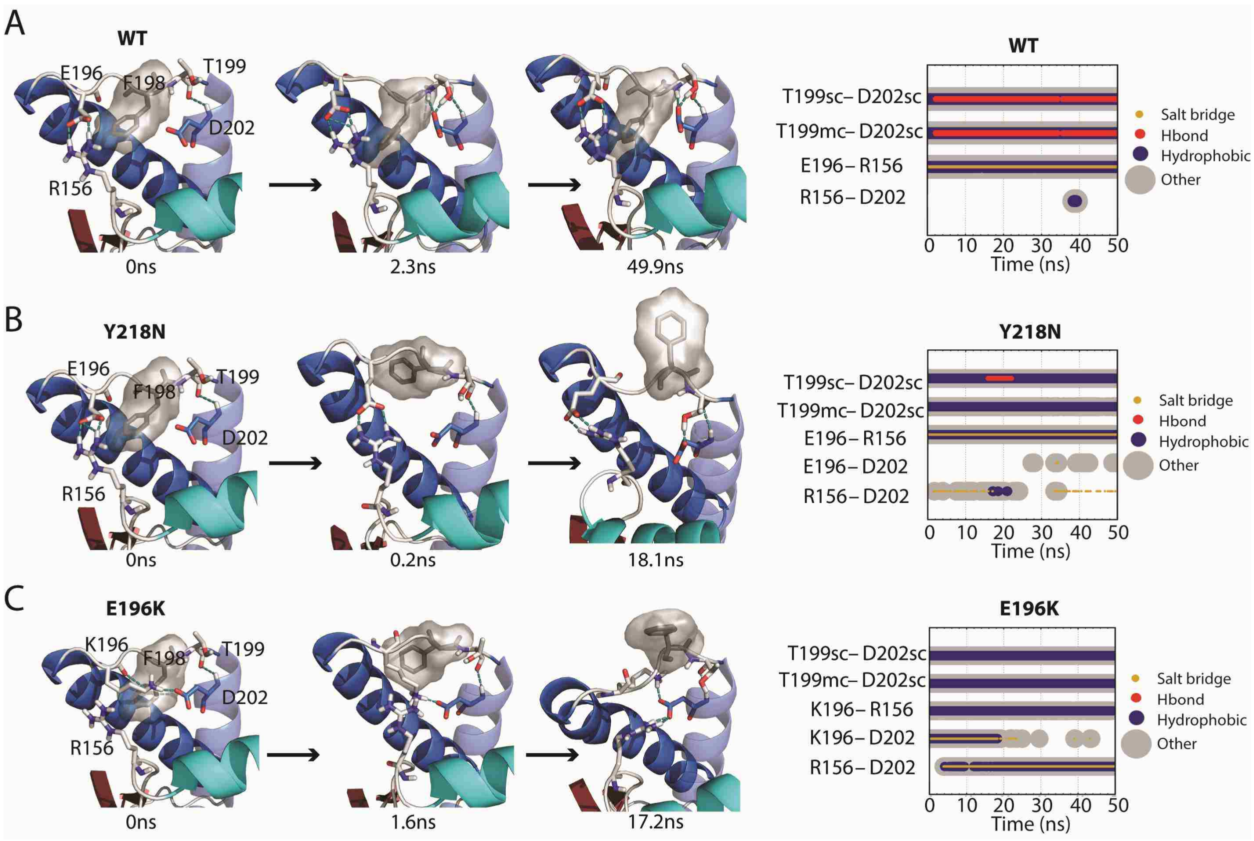

Figure 2.6 Salt bridge network around the F198 side chain

(A, B and C) Structures at specific time points of the WT simulation 2, Y218N simulation 1, and E196K simulation 2, respectively. Secondary structure color schemes are cyan for HA, blue for HB and HC, where the transparent helix is HC. Residues E/K196, F198, T199, D202, and R156 are shown in sticks and hydrogen bonds are indicated with dotted blue lines. (far right) Relevant contacts are plotted over time.

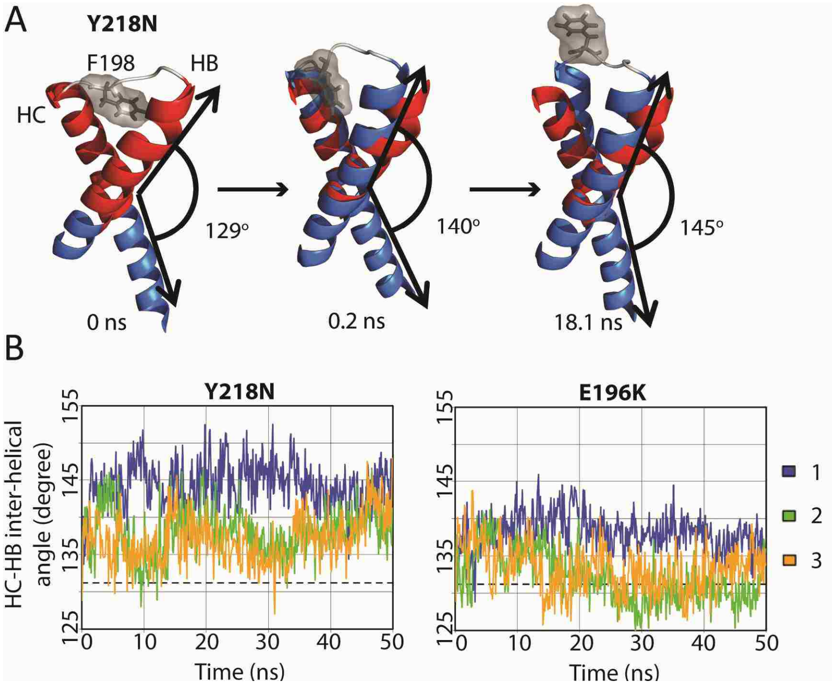

Figure 2.7 Change in interhelical angle between HB and HC in Y218N

(A) Structures in simulation 1 of Y218N. Only the HB-HC loop (gray), HB and HC (blue) are shown. The red helices represent the starting structure of residues 179-194 and 200-214, where the interhelical angle is defined between those two fragments of HB and HC. Interhelical angles between HB and HC for each snapshot are indicated. (B) Inter helical angle between HB and HC at 100 ps granularity. The average interhelical angle of the last 25 ns of the WT simulations is shown in dashed lines.

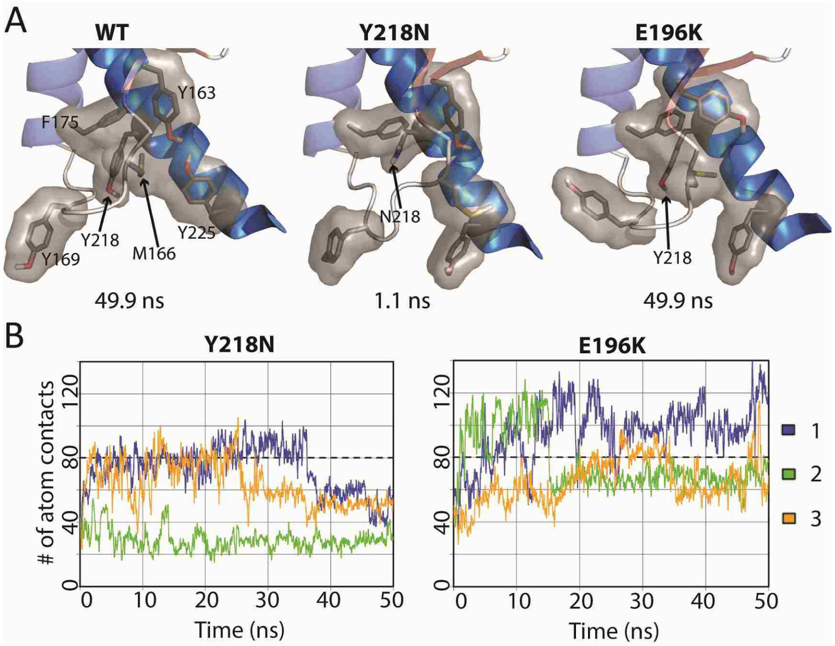

Figure 2.8 Loss of hydrophobic packing around in the X-loop in Y218N simulations

(A) Relevant residues involved in X-loop packing interactions are shown in sticks for simulation 2 of WT, Y218N, and E196K (B) Number of atom contacts between residues Y163, M166, Y169, F175, Y/N218, and Y225. Window averages (100 ps) of number of atom contacts are shown for all mutant simulations. The average number of atom contacts of the last 25 ns of the WT simulations is shown in dashed lines.

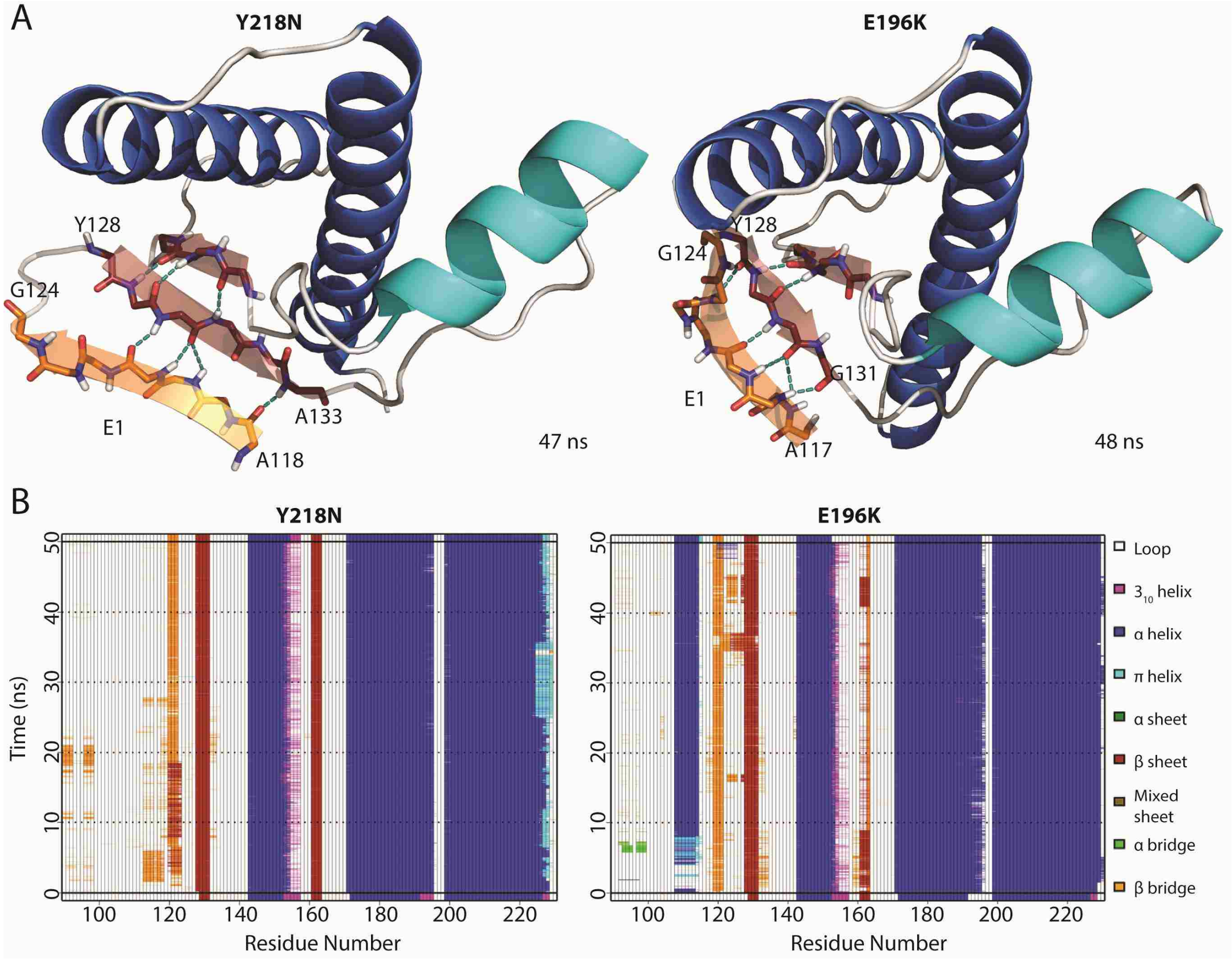

Figure 2.9 Formation of nonnative strand (E1) in both Y218N and E196K simulations

(A) Representative E1 structure for each mutant. Backbone of E1 is shown in sticks with carbon atoms colored in orange. Carbon atoms of the extended native sheets are colored in red. Hydrogen bonds between strands are indicated with the cyan dashed lines. The N- and C-terminal residues for E1 and the extended S1 strand (in red) are labeled. (B) Secondary structure analysis of simulation 2 of Y218N and simulation 3 of E196K.

Chapter 3

MISFOLDING OF BOVINE PRION PROTEIN AT ACIDIC PH

3.1 Summary

Bovine spongiform encephalopathy (BSE), or mad cow disease, is a fatal neurodegenerative disease that is transmissible to humans and that is currently incurable. BSE is caused by the prion protein (PrP), which adopts two conformers; PrP^{C} is the native innocuous form, which is α-helix rich; and PrP^{Sc} is the β-sheet rich misfolded form, which is infectious and forms neurotoxic species. Acidic pH induces the conversion of PrP^{C} to PrP^{Sc}. We have performed molecular dynamics simulations of bovine PrP at various pH regimes. An acidic pH environment induced conformational changes that were not observed in neutral pH simulations. Putative misfolded structures, with nonnative β-strands formed in the flexible N-terminal domain, were found in acidic pH simulations. Two distinct pathways were observed for the formation of such nonnative β-strands: at low pH, hydrophobic contacts with M129 nucleated the nonnative β-strand; at mid pH, polar contacts involving Q168 and D178 facilitated the formation of a hairpin at the flexible N-terminus. These mid and low pH simulations capture the process of nonnative β-strand formation, thereby improving our understanding of how PrP^{C} misfolds into the β-sheet rich PrP^{Sc} and how pH factors into the process.

3.2 Introduction

Prion diseases are neurodegenerative diseases that are transmissible, fatal and currently incurable. Such diseases include Creutzfeldt–Jakob disease (CJD) in humans, bovine spongiform encephalopathy (BSE) in cattle, chronic wasting disease in elk and scrapie in sheep (135, 136).

In humans, variant CJD is caused by consuming BSE-contaminated products (3, 137). BSE has a significant economic impact on society; in 2003, a single case of BSE in Washington resulted in an estimated annual loss of $7 billion to $10 billion, due to suspended beef exports to overseas markets (15).

Prion diseases are caused by the misfolding and aggregation of the prion protein (PrP). The native form of PrP (denoted as $\mathrm{PrP^C}$) is innocuous and expressed ubiquitously in all mammalian cells. However, $\mathrm{PrP^C}$ can misfold into $\mathrm{PrP^{Sc}}$, which can then self-aggregate and form soluble oligomers that cause neuronal cell death. Misfolding is rare, but it can be induced by an acidic pH environment (138–142). $\mathrm{PrP^C}$ is a glycolipid anchored protein expressed at the cell surface. While some $\mathrm{PrP^C}$ is endocytosed and digested in lysosomes (143), some $\mathrm{PrP^C}$ is leaked into the cytosol (144). Therefore, $\mathrm{PrP^C}$ experiences pH from 7.4 (in cytosol) (145) to 4.6 (in endosome) (146) during its cellular lifetime. The endosome is a site for PrP misfolding (147–150), and low pH triggers conversion *in vitro* (138–142). It is therefore of interest to study the pH effects on the native $\mathrm{PrP^C}$ structure, which ideally would narrow down possible cellular regions, where pH-induced misfolding may occur. The pH-induced structural effect on recombinant PrP has been studied for various species (141, 142, 151). Recombinant human PrP in between pH 7.2 and 5.0 is mostly helical, but PrP misfolds into a β-sheet rich structure at a lower pH range (pH 4 to 3.6) (142).

The structure of the C-terminal domain of $\mathrm{PrP^C}$ has been resolved by NMR methods for various species (29, 30, 72, 73). The NMR structure of bovine $\mathrm{PrP^C}$ is almost identical to that of other mammalian species. All mammalian $\mathrm{PrP^C}$ structures consist of a structured C-terminal domain with three helices (HA, HB and HC) and two short β-strands (S1 and S2), and a flexible

N-terminal domain (Figure 1.1). Although no high resolution structure for PrP^{Sc} is available, low resolution experimental methods have suggested that the native PrP^{C} converts from an α-helical rich protein (47% α-helix, 3% β-structure) to the β-sheet rich PrP^{Sc} (43–54% α-helix, 17–30% β-structure) (34–36). The bovine PrP^{Sc} structure is important for understanding the mechanism of cross-species transmission, especially the transmission of BSE to humans (137). However, the aggregation tendency and heterogeneity of PrP^{Sc} has limited experimental methods to isolate PrP^{Sc} and obtain a high-resolution structure of PrP^{Sc}. The cross-species transmissibility of bovine PrP^{Sc} makes experimental characterization of PrP^{Sc} potentially dangerous, and outfitting a lab of a suitable safety level can be a hurdle to perform experimental work. Given the experimental limitations of studying bovine PrP^{Sc}, computational methods offer an attractive alternative.

Molecular dynamics (MD) simulations can capture protein dynamics and associated conformational changes at the atomic level. Furthermore, modeling acidic pH environment in simulations is also possible by changing the protonation states of protein amino acids (44, 50, 96, 152). We have performed acidic pH simulations of various species of PrP (44, 50, 51, 96), including bovine PrP (103); however, the bovine simulations were not analyzed in depth, and the sampling was limited. In order to more thoroughly investigate the pH-induced misfolding of the bovine PrP, we performed MD simulations of the bovine PrP at neutral, mid and low pH, which corresponds approximately to ranges around pH 7, 5 and 4, respectively. Five 50 ns simulations were performed for each pH regime, which amounted to a total of 750 ns of simulations. Both mid and low pH affected the native polar contact network, which resulted in conformational changes of the HA helix and the native sheet. At acidic pH, nonnative β-strands formed, which are hallmarks of PrP misfolding (44, 51, 96). These MD-derived misfolded structures are useful for modeling the oligomeric structure of $\mathrm{PrP^{Sc}}$ (51, 52) and improve our understanding of the misfolding and aggregation process of $\mathrm{PrP^{Sc}}$.

3.3 Results and Discussion

The starting structure of bovine $\mathrm{PrP^{C}}$ was constructed from the NMR structure of the C-terminal fragment (PDB code: 1DWY, residues 128–227) (30). The flexible N-terminal residues 90–127 and C-terminal residues 228–231 were manually constructed, as described previously (44). We performed simulations of bovine PrP at neutral, mid and low pH, which corresponded to the approximate pH environment in the cytosol (pH 8–6), endosome (pH ~5–4) and *in vitro* misfolding experiments (pH ~4). Amino acid side chains were protonated differently in order to model the bovine PrP at each pH regime (see the Experimental Section for details). Protonation of side chains had a significant impact on the polar contacts within the protein. At neutral pH, histidines were neutral, while Asp and Glu were negatively charged. At mid pH, histidines were doubly protonated (positively charged), which allowed them to form salt bridges with other negatively charged amino acids. At low pH, all Asp and Glu acids were protonated (neutral charge). This abolished all salt bridges and significantly disrupted the native hydrogen bonds that involve the side chains of Asp and Glu. Large conformational changes were observed at mid and low pH relative to the neutral pH simulations. The solvent accessible surface area of hydrophobic regions increased in most of the mid and low pH simulations. Putative misfolded structures were also observed in both mid and low pH simulations; the flexible N-terminus formed nonnative β-strands by interacting with the S1 strand. Using MD simulations, we have captured the structural effects on bovine PrP induced by acidic pH. These results are discussed in detail below.

3.3.1 *Structural Stability and Deviation from the Native Structure*

To determine the structural deviations at the C-terminal domain, the Cα root mean square deviations (RMSDs) of residues 128–225 were measured for all simulations (Figure 3.2A). Residues 128–225 include the stable native secondary structures, except for residues 226–231, which are flexible residues at the C-terminus. The Cα RMSD signifies the backbone structural deviation from the native bovine PrP starting structure. The Cα RMSD of residues 128–225 of most simulations reached a plateau by 10 ns, and all simulations reached the steady state after ~25 ns (Figure 3.2A,B). The average Cα RMSD value over the 25–50 ns interval for all neutral pH simulations was 1.9 Å with a standard deviation of 0.22 Å, indicating small deviations from the native structure. Mid pH simulations consistently reached higher Cα RMSDs than neutral pH simulations did by ~1 Å. The Cα RMSDs of the low pH simulations were less consistent than that of mid pH simulations. Low pH simulations 2 and 4 had higher Cα RMSDs than the neutral pH simulations. These results are consistent with our expectation that acidic pH induces structural changes.

The amount of backbone fluctuations in residues 128–225 are reflected in the Cα root mean square fluctuations (RMSF) for each residue from 128 to 225 (Figure 3.2B). Generally, the secondary structure elements had lower Cα RMSF (~0.4–0.6 Å) than the loop regions (~0.6–1.2 Å). Both neutral and mid pH had comparable Cα RMSF, with the highest Cα RMSF being 0.9 Å at residue 140, which is located at the loop preceding HA. Low pH simulations had higher Cα

RMSF, especially in the loop regions. Residues 140–145 near the N-terminus of HA were noticeably more mobile (Cα RMSF >0.9 Å) at low pH than at neutral or mid pH.

The Cα RMSD indicates that the C-terminal domain of the mid pH simulations deviated consistently from the native structure, but the C-terminal domain retained a similar backbone flexibility profile to that of the neutral pH simulations. This suggests that the doubly protonated histidines in the mid pH simulations altered the native PrP conformation, but they did not affect the backbone flexibility significantly. The Cα RMSDs of low pH simulations were less consistent, and residues 128–225 in low pH simulations were markedly more mobile at loop regions than in neutral and mid pH simulations. The mobility gained in low pH simulations is expected, since all salt bridges and many side chain hydrogen bonds were abolished.

3.3.2 *HA and Native Sheet Conformational Changes*

To measure tertiary structural deviation from the native structure, a stable core region (residues 174–186 and 200–219) was used as the alignment for the subsequent Cα RMSD measurements. The stable core region is the most well-defined substructure within bovine PrP, as determined by NMR (30). Cα RMSDs were measured for the globular domain (residues 128–228), HA (residue 144–156) and native strands (residues 128–131 and 161–164) (Figure 3.3A). For the last 25 ns of the neutral pH simulations, the average Cα RMSD of the globular domain and HA were 2.5 Å and 2.8 Å, respectively. Cα RMSD for the globular domain and HA of mid pH simulations were on average 1.4 Å and 3 Å higher than those of neutral pH simulations respectively (Figure 3.3B). Among the low pH simulations, only in simulations 2 and 4 did the globular domain and HA regions deviate significantly from the native structure. For simulations

1, 3 and 5, the Cα RMSDs of HA were comparable to that of the neutral pH simulations. Therefore, the low pH simulations were able to adopt both native and nonnative conformations of HA, unlike the mid pH simulations that yielded consistently nonnative conformations. The large globular Cα RMSD values correlated with the large Cα RMSD of HA, suggesting that HA is the main contributor to the structural changes in the globular domain. Structures of HA in the last 25 ns of the mid and low pH simulations are shown in Figure 3.3A. All mid pH simulations had HA shifted downward from the native position, while some low pH simulations still retained a native-like HA position. Previous MD simulations of human and hamster PrP (44, 50, 51, 96) and replica exchange simulations of sheep PrP [34] have detected a PrP intermediate state, in which HA detaches from HC. Our simulation results suggest that the conformation of HA is sensitive to acidic pH, consistent with experimental studies on the mouse PrP, indicating that residues 144–149 (a portion of HA) increase in mobility at acidic pH (100).

The average Cα RMSDs of the β-sheet in the neutral, mid and low pH simulations were 1.48 Å, 1.67 Å and 2.09 Å, respectively. In addition to the Cα RMSD, the inter-strand angles of the native sheets were measured to identify different sheet conformations (Figure 3.3C). The inter-strand angles were defined, such that they were in between 0^{o} (flat and parallel β-strands) and 180^{o} (flat and anti-parallel β-strands). The average inter-strand angles and native sheet Cα RMSDs for the last 25 ns of mid and low pH simulations are shown in Figure 3.3C. All low pH simulations had average inter-strand angles $>132^{o}$, whereas all mid pH simulations had average inter-strand angles $<129^{o}$. For neutral pH simulations, the inter-strand angles, ranging from 123^{o} to 133^{o}, were in between the range of both mid and low pH inter-strand angles. Although the inter-strand angles at neutral pH were not consistent across simulations, native strands were consistently more twisted in mid pH simulations than in low pH simulations. pH-induced conformational changes of the native strand S2 has been confirmed by spin-labeling experiments on mouse PrP (100). In addition, a PrP^{Sc}-specific antibody that binds to the tyrosine-tyrosine-arginine epitope at S2 suggests that S2 undergoes conformational changes upon misfolding (153). Therefore, the conformational differences of the native sheet between neutral and acidic pH simulations (both mid and low pH) may be related to the early misfolding mechanisms of the PrP.

3.3.3 *Structural Changes and Alterations in Native Polar Contacts*

In order to understand the cause of deviations of HA and native strands from their native conformation at both mid and low pH, the polar contacts near HA and the native strands were analyzed (Table 3.1). Polar contacts include both hydrogen bonds and salt bridges between residues (see the Experimental Section for details). Mid pH simulations were able to form nonnative salt bridges with the doubly protonated histidines. Most of the native side chain polar contacts were lost at low pH. Changes in polar contacts at acidic pH simulations led to the detachment of HA and alterations to the β-sheet, as well as other changes in the protein. These issues are discussed in detail in the following sections.

Polar Contacts with HA

In the neutral pH simulations, the populated polar contacts (average occupancy >50%) around HA were: Y149-D202, R156-D202, E146-R208 and K194-E196 (Figure 3.4A). HA was anchored to HC by the side chain polar contacts, Y149-D202 and E146-R208. The salt bridge R156-D202 tethered the C-terminus of HA to HC. Among these three HA stabilizing contacts, the hydrogen bond Y149-D202 was the most stable contact, on average occupied 91% of the time in the neutral pH simulations (Table 3.1). In the mid pH simulations, only two of these HA stabilizing contacts were preserved: E146-R208 and R156-D202. The hydrogen bond between Y149 and D202 was completely lost in all mid pH simulations. The doubly protonated H155 formed a nonnative salt bridge with E196. The salt bridge H155-E196 was 100% populated in two of the mid pH simulations. These changes in the polar contacts around HA were accompanied with the large deviation of HA from its native position (Figure 3.3B).

Large HA movements were also observed in low pH simulations 2 and 4 (Figure 3.3B). The low pH simulations lost all of the polar contacts around HA (percentage of time in contact during 25–50 ns, <1%). While both mid and low pH simulations displayed large deviations of HA from its native position, HA was less flexible at mid pH than at low pH, as indicated by the Cα RMSF (Figure 3.2B). This suggests that the polar contacts at mid pH have a stabilizing effect on the nonnative position of HA. These observations are consistent with previous NMR studies on the human PrP at acidic pH, suggesting that the doubly protonated H155 affects the native PrP structure (28). Such effect was shown explicitly in two of our mid pH simulations, whereby H155 formed a nonnative salt bridge with E196, thus stabilizing the nonnative position of HA. As for low pH simulations, the loss of all salt bridges and many side chain hydrogen bonds allowed for flexibility at HA, as indicated by Cα RMSF (Figure 3.2B).

Polar Contacts with S2

In the neutral pH simulations, three polar contacts, Y163-E221, Y162-T183 and Y162-E186, had average occupancies of 71%, 30% and 28%, respectively (Table 3.1). These contacts anchored S2 to the stable core region of PrP (Figure 3.4B). In most of the mid pH simulations, the hydrogen bond Y162-T183 was not present (<30% occupancy), but the Y162 and Y163 side chains both formed relatively stable hydrogen bonds with E186 and E221, respectively. In mid pH simulation 2, the side chain conformation of E186 was further stabilized by forming a nonnative salt bridge with the doubly protonated H187 (Figure 3.4B). This interaction indirectly stabilized the hydrogen bond between Y162 and E186 (100% occupancy).

The hydrogen bonds, Y162-E186 and Y163-E221, anchored S2 to HB and HC. These two anchors favored a more twisted inter-strand angle, as observed in mid pH simulations (Figure 3C). In low pH simulations, hydrogen bonds Y162-E186 and Y163-E221 were lost, due to the protonation of the glutamic acids, but there was a gain in the hydrogen bond Y162-T183, in most of the low pH simulations. In low pH simulation 1, the hydrogen bond Y162-T183, occupying 84% of the time, was more prevalent than in any neutral or mid pH simulations. The high occupancy for the hydrogen bond Y162-T183 at low pH was also observed in previous MD simulations of human PrP (121). Such high occupancy for the hydrogen bond Y162-T183 at low pH can be explained by the lost of the two anchors Y162-E186 and Y163-E221 at low pH, thus allowing S2 to pack closer to HB, and therefore low pH simulations favored the formation of the hydrogen bond Y162-T183. With the loss of the two anchors, the native strands became less twisted, as indicated by inter-strand angles (Figure 3.3C). Given that the exposed native strand, S1, is at the packing interface between PrP dimers from sheep PrP crystals (31), changes in the native sheet region could modulate intermolecular interactions among PrP. The native strand, S1, is also known for recruiting nonnative β-strands from the flexible N-terminus, as shown in previous MD-derived misfolded structures (44, 50, 51, 88, 96, 121). Therefore, changes of the inter-strand angle may affect the formation of nonnative β-strand, which is an important hallmark for misfolding.

3.3.4 *Solvent Exposure of Hydrophobic Regions*

The hydrophobic core of PrP consists of a set of hydrophobic residues within the globular domain. There are two regions of the hydrophobic core: the HA-HC region and the HB-HC region (Figure 3.5A). The average solvent accessible surface areas (SASA) for hydrophobic regions HA-HC and HB-HC were 88 $Å^2$ and 191 $Å^2$, respectively. The differences in SASA with respect to the neutral pH simulations are shown in Figure 3.5B. The HA-HC hydrophobic core in the mid pH simulations was significantly exposed in four out of five simulations (Figure 3.5B). As for the HB-HC portion, only mid pH simulation 5 had a large difference in SASA with respect to the neutral pH simulations (57 $Å^2$). Among low pH simulations, only simulation 4 had the HA-HC hydrophobic core significantly exposed. Low pH simulations 1, 2 and 5 tended to have a larger HB-HC hydrophobic core SASA than neutral pH simulations do (>42 $Å^2$ difference). Residues that contributed significantly to the increased solvent exposure were M134, F141 and F198, of which both M134 and F141 are part of the HA-HC hydrophobic core and F198 is in the HB-HC hydrophobic core (Figure 3.5C).

NMR studies of human PrP have shown that HA becomes less stable at acidic pH (28). This is in agreement with the disrupted hydrophobic packing and detachment between HA and HC in the mid and low pH simulations. The hydrophobic residue F141 is one of the less stable residues, as identified by unfolding experiments of bovine PrP (111). Such lack of stability was also reflected in our simulations, in which F141 detached from the hydrophobic core and became solvent exposed at low pH. Previous MD simulations have shown that large displacement of HA can be caused by mutations that disrupt the hydrophobic packing between HA and HC (154). In addition, detachment of HA from HC is necessary for PrP^{Sc} fibril formation, as indicated in *in vitro* (106, 107) and *in vivo* (107) disulfide engineering experiments. All of these experimental data suggest that the displacement of HA and the exposure of the HA-HC hydrophobic region are related to PrP misfolding.

In the starting structure, F198 was buried in between HB and HC, with less than 20 $Å^2$ SASA of the side chain exposed. However, in the low pH simulations, the HB-HC loop became highly flexible (Figure 3.2B), and the side chain of F198 was exposed (~50–100 $Å^2$). The change in flexibility of the HB-HC loop and the increase in solvent exposure of F198 side chain are possibly related to the misfolded conformation of residues 187–206 detected by a PrP^{Sc}-specific antibody (112). Furthermore, the F198S human pathogenic mutation causes a void in the HB-HC hydrophobic core and reduces the thermodynamic stability of PrP, which, in turn, increases the propensity of PrP^{Sc} conversion (86, 110), suggesting that the loss of hydrophobic packing with F198 facilitates misfolding.

3.3.5 *Formation of Nonnative β-Strands*

An increase in β-sheet content is evident in the process of PrP^{C} misfolding to PrP^{Sc} (34–36), and therefore, it is expected that misfolding involves the formation of nonnative β-strands. Previous MD simulations have indicated that the flexible N-terminus can form nonnative strands, and they are the putative aggregation sites for PrP^{Sc} oligomerization (51, 52). Although misfolding is rare, some of our simulations captured the misfolding process. Nonnative strands were formed in low pH simulation 3 and mid pH simulation 2. In both simulations, the native strand, S1, served as the nucleation site for recruiting the nonnative strands from the flexible N-terminus. The process of nonnative β-strand formation is described in detail below.

Hydrophobic Contacts at Low pH

In low pH simulation 3, a nonnative strand formed at the flexible N-terminus, in which residues 116-120 docked to the native strand S1 (Figure 3.6A). Hydrophobic contacts between M129 and residues at the N-terminus facilitated the nucleation of the nonnative strand (Figure 3.6B). The starting structure of the N-terminus was extended away from the globular domain, and only A118 and M129 were in contact. After 11.6 ns, the N-terminus collapsed, and V112 was in contact with M129. At 29.1 ns, residues A118, V112 and M109 formed a hydrophobic cluster around M129. At this point, a β-bridge was already formed between the nonnative strand region and S1 (Figure 3.6C). Eventually, the nonnative β-strand was formed at 32.6 ns, with A116 participating in the hydrophobic cluster around M129. This β-strand was stable for approximately 10 ns (Figure 3.6C).

The process of forming the nonnative β-strand was driven by hydrophobic contacts with M129. Prion protective polymorphisms in both human (155) and cervid (156, 157) PrP at residue 129 are found in nature, suggesting that residue 129 play a key role in misfolding, and Chen *et al.*, 2014, addresses the differences between M129 and V129 in human PrP simulations (158). Hydrophobic residues M109, V112, A116 and A118 make contact with M129 and are part of the neurotoxic peptide, PrP 106–126 (94, 159–161), which becomes enriched in β-structure at acidic pH (159, 160). These experimental observations lend support to our MD-derived misfolded structure at low pH, whereby residues 116–120 at the N-terminus formed a nonnative β-strand driven by hydrophobic contacts with M129.

Polar Contacts at Mid pH

In mid pH simulation 2, R164 and Q168 formed hydrogen bonds with the backbone carbonyls of residues 125–127 near the N-terminus of S1 (Figure 3.7A,B). Such hydrogen bonds resulted in the backbone amides of residues 125–127 pointing away from the globular domain of the PrP. This backbone conformation favored the formation of a hairpin turn, which was observed after 11.7 ns in simulation (Figure 3.7A). Residues 121–123 formed stable β-bridges with residues 126 and 127 (Figure 3.7C). At 32.1 ns, residues 118–119 formed another pair of β-bridges with residue 121. The hairpin turn residues 123–127 at the N-terminus of S1 had a similar conformation compared to the turn residues of α-hairpins found in previous MD simulations of the PrP (121) and polyglutamine peptides (162). α-sheet structures represent putative toxic conformers in amyloid disease (92). The terminal turn residues in an α-hairpin have α_L conformations (162). In this mid pH simulation, the α_L backbone conformation at residue 127 was stabilized by backbone hydrogen bonds with the side chains of R164 and Q168. At 39.4 ns, Q168 lost its hydrogen bond with residue 126. Instead, the R164 side chain formed two hydrogen bonds with the backbone carbonyls of residues 126 and 127. This pair of side chain-main chain hydrogen bonds also stabilized the α_L conformation at residue 127, thereby stabilizing the hairpin turn. Furthermore, the side chain conformation of R164 was stabilized by a salt bridge with D178 (occupied throughout the entire simulation).

Residues 168 and 178 are related to prion-susceptible polymorphisms (163) and a human PrP pathogenic mutation (164) respectively. Previous MD simulations have shown that the loss of the native salt bridge, R164-D178, caused by the pathogenic D178N mutation, does not significantly disrupt the structured C-terminal domain of the PrP (165), thus implicating that the misfolding may occur elsewhere in the PrP, such as the flexible N-terminal region. As shown in mid pH simulation 2, the R164-D178 salt bridge contributed to the nonnative strand formation at the N-terminus: the stable salt bridge R164-D178 placed the guanidinium group of R164 in the same plane as S1. Under this conformation, side chain of R164 interacted with the backbone carbonyl of G126 and G127, supporting the hairpin formation at the flexible N-terminus. As for Q168, its side chain also formed hydrogen bonds with the hairpin turn residues, G126 and G127. Since polymorphism at residue 168 modulates the prion susceptibility of sheep (163) and the mouse PrP mutation Q168R completely abolishes PrP^{Sc} formation (166), we hypothesize that Q168 plays an important role in PrP misfolding.

The biological relevance of residues 168 and 178 supports our computational results; both residues 168 and 178 facilitated the nonnative strand formation at the flexible N-terminus. Residues 168 and 178 stabilized the α_L conformation at residue 127, facilitating formation of a new hairpin. This resulted in an increase in β-sheet content, which is a hallmark of misfolding.

3.4 Materials and Methods

The starting structure of the simulations was derived from the NMR structure of bovine PrP obtained at pH 4.5 (PDB code: 1DWY (30)). The missing regions, the flexible N-terminus (residues 90–127) and the C-terminus (residues 228–231), were manually constructed, as described previously (44). It is important to include the N-terminal fragment, because there is strong evidence that it plays an important role in misfolding (77, 115, 120, 167). Briefly, residues

90–127 were constructed using limited Nuclear Overhauser Effect (NOE) restraints from the hamster PrP for the same region. The flexible N-terminus was built such that it lies approximately perpendicular to S1 and S2. The N-terminus was extended away from the globular domain, to minimize interactions that could bias simulations. The C-terminal residues 228–231 were manually built by extending the C-terminus of HC.

The pH environment of the simulation was modeled by altering the protonation state of amino acids. At neutral pH, all glutamates and aspartates were unprotonated (negatively charged). H144 was δ-protonated, whereas all other histidines were ε-protonated, following the results of Langella *et al.* (99). Langella *et al*. have estimated the pKa values of the human PrP. Their results show that H140 prefers the δ tautomeric form, whereas all other histidines preferred the ε tautomeric form at neutral pH. At mid pH, all histidines were doubly protonated (positive charge). Aspartates and glutamates remained unprotonated. Since the lowest pKa among histidine residues in PrP is ~5.5 (99) and the pKa of aspartic and glutamic acids are ~4, the mid pH environment in simulation roughly corresponds to pH 5. At low pH, all aspartic and glutamic acids residues were protonated, and histidines were doubly protonated. Therefore, the pH in which simulations were performed should be lower than the pKa values of Glu and Asp residues (pKa ~4).

MD simulations were performed at 298 K using *in lucem* molecular mechanics (*il*mm) (129). The NVE microcanonical ensemble (constant number of atoms, volume and total energy) was employed. The Levitt *et al.* force field (130) was employed for the protein. Preparation of the simulation followed previously described protocols (132). Briefly, the steepest descent minimization was performed for the starting structure *in vacuo* for 1,000 steps. The minimized structure was placed in an empty rectangular water box with the following dimensions: 88.7 Å by 77.1 Å by 48.1 Å. The system contained 10,100 water molecules, and the box volume was set to reproduce the density of water at 298 K (0.997 g/mL (168)). The F3C water model (131) was implemented. The walls of the periodic box were at least 10 Å away from the protein. Water molecules were minimized for 1,000 steps. After that, 1 ps of water dynamics was performed to heat the system to 298 K. Water molecules were minimized for another 500 steps. The protein was then minimized for 500 steps. For every two steps, a force-shifted non-bonded cutoff of 10 Å was updated (169). A time step of 2 fs was used for performing MD simulations. Five 50 ns simulations were performed at neutral, mid and low pH each, in total amounting to 750 ns of simulations. Random number seeds were used to randomize the initial velocities for atoms in different simulation replicates.

*il*mm (129) was used to perform Cα RMSD, DSSP (Define Secondary Structure of Proteins) (134) and SASA (133) analyses at 10 ps granularity. The Cα RMSF was measured using 1 ns windows throughout the simulations and averaged across all five simulations for each pH regime. Native sheet angles were measured at 100 ps granularity. Briefly, a vector was used to fit the Cα atoms on each native strand (residues 128–131 for S1 and 161–164 for S2). The angle between the two vectors were calculated using Visual Molecular Dynamics (VMD) (170). Atomic contacts were classified as salt bridges (N-O distances ≤4.6 Å between oppositely charged residues), hydrogen bonds (H-acceptor distance ≤2.6 Å and donor-H-acceptor angle >135°) and hydrophobic contacts (C-C distance ≤5.4 Å). Polar contacts included both salt bridges and hydrogen bonds formed between atoms. For the neutral pH simulations, the averaged values were over four simulations. This is because neutral pH simulation 4 had a large conformational change at HA (average HA Cα RMSD = 8 Å). Due to the significant deviation from the native structure, neutral pH simulation 4 was considered an outlier.

3.5 Conclusions

We have identified common misfolding events of bovine PrP at mid and low pH, such as: (1) detachment of HA from HC; (2) an increase in solvent exposure of the hydrophobic core; and (3) the formation of nonnative strands in the flexible N-terminus. The HB and HC helices remained largely intact, in agreement with the experiment (54). Although putative misfolded structures in both the mid and low pH simulations had nonnative strands at the flexible N-terminus, the mechanisms by which nonnative strands formed at mid and low pH simulations were significantly different. At mid pH, a network of polar contacts involving the Q168 and D178 side chains stabilized the hairpin turn at the N-terminus of S1, thus favoring the formation of a stable nonnative strand at the flexible N-terminus. At low pH, M129 formed hydrophobic contacts with residues at the N-terminus, facilitating the formation of a nonnative strand. The presence of different misfolding pathways of bovine PrP is consistent with the heterogeneous nature of PrP^{Sc}. The key residues involved in misfolding are related to single-nucleotide polymorphisms M129 and Q168 associated with prion disease susceptibility, and the pathogenic mutation D178N, thereby supporting the biological relevance of our simulation results. These simulations provide further insight into how PrP^{C} misfolds into a β-sheet rich structure under acidic pH conditions. Furthermore, the identified misfolded structures may help with the construction of oligomeric bovine PrP^{Sc} models and provide much-needed clues to understand the molecular mechanism of disease transmission.

Table 3.1 Population of polar contacts between pairs of residues

All polar contacts listed are between residue side chains, except for Y162-T183, in which the side chain of T183 formed a hydrogen bond with the backbone amide of Y162. Contacts were calculated for the last 25 ns in simulations

pH	Simulation	HA relevant contacts					S2 relevant contacts			
		Y149-D202	R156-D202	E146-R208	K194-E196	H155-E196	Y162-T183	Y162-E186	Y163-E221	E186-H187
Neutral	Average	90.7	51.4	73.7	52.8	0.0	29.7	28.1	70.9	0.0
Mid	1	0.0	100.0	100.0	100.0	100.0	20.1	29.3	99.9	0.0
	2	0.3	100.0	100.0	3.9	100.0	2.6	100.0	99.2	89.3
	3	0.0	100.0	100.0	0.0	0.0	30.7	15.0	66.5	0.0
	4	0.0	100.0	100.0	0.3	7.2	0.5	94.2	99.3	0.0
	5	0.0	16.2	0.0	70.1	0.0	0.5	48.2	100.0	0.0
Low	1	0.0	0.0	0.0	0.0	0.0	84.4	0.0	2.9	0.0
	2	0.1	0.0	0.0	0.0	0.0	74.6	0.0	1.0	0.0
	3	0.0	0.0	0.0	0.0	0.0	0.2	0.0	1.2	0.0
	4	0.0	0.0	0.0	0.0	0.0	57.1	0.0	0.0	0.0
	5	0.0	0.0	0.0	0.0	0.0	66.4	0.1	0.5	0.0

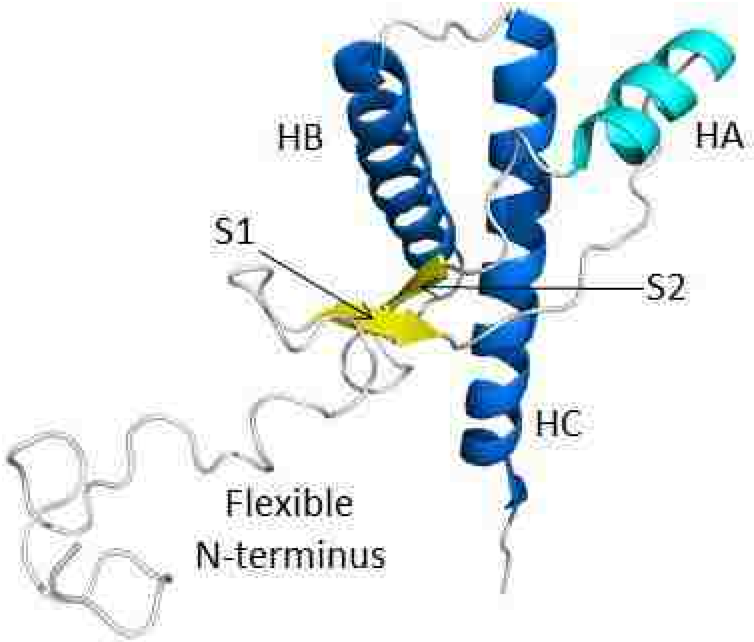

Figure 3.1 Native structure of bovine PrP^{C} (residues 90–231)

HA (residues 144–154), HB (residues 173–194) and HC (residues 200–228), S1 (residues 128–131) and S2 (residues 161–164) are colored in cyan, blue and yellow, respectively. Loop regions are colored in gray. The flexible N-terminal residues 90–127 and C-terminal residues 228–231 were manually constructed. The structure for residues 128–227 was obtained from the bovine PrP NMR structure (Protein Data Bank (PDB) code: 1DWY) (30).

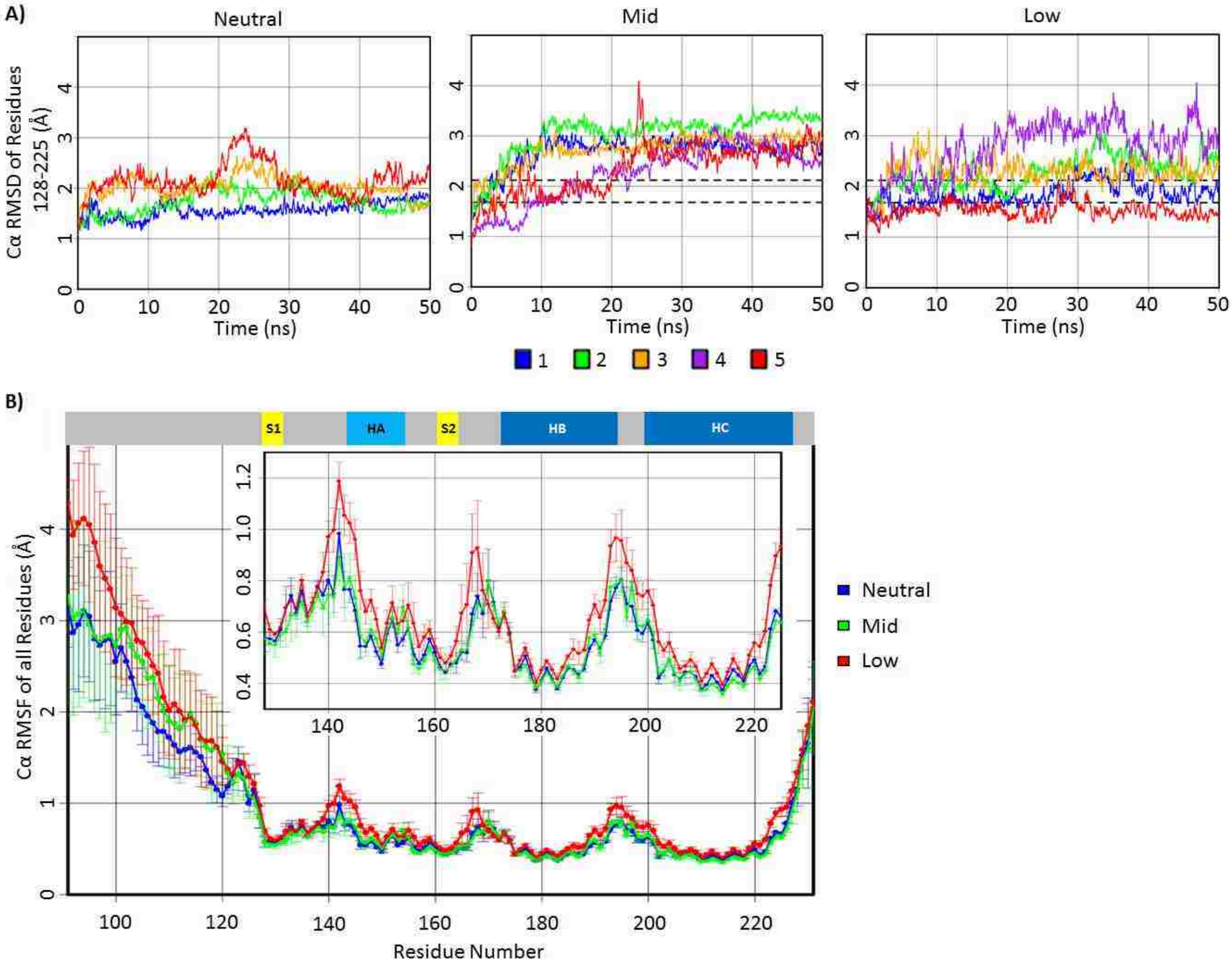

Figure 3.2 Cα root-mean-square deviation (RMSD) and root mean square fluctuations (RMSF) of the bovine PrP simulations

(A) Residue 128–225 Cα RMSD of the neutral, mid and low pH simulations plotted over time. The area in between the dotted lines is within one standard deviation of the 25–50 ns averaged Cα RMSD of the neutral pH simulations. (B) Averaged Cα RMSF plotted for all residues in neutral, mid and low pH simulations. The inset plot shows Cα RMSF for residues 128–225 in a magnified scale. Native secondary structures of the PrP are shown at the top of the Cα RMSF plots.

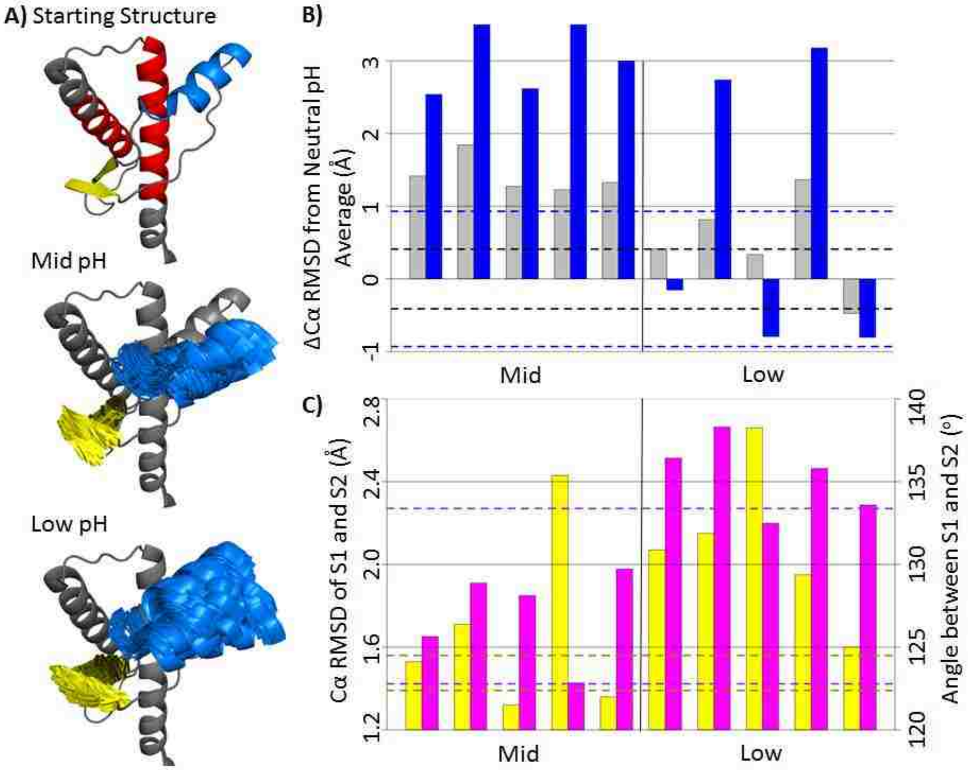

Figure 3.3 Conformational changes of bovine PrP at mid and low pH

(A) Starting structure of the globular domain (residues 128–228) is shown in gray. HA (residues 144–156) and the native sheet (residues 128–131 and 161–164) are colored in blue and yellow, respectively. Top: the starting structure of the globular domain of the PrP. The stable core region (residues 174–186 and 200–219) is in red. Middle and Bottom: the starting structure of the globular domain overlapped with frames from 25–50 ns of mid and low pH simulations for HA and the native sheet. The structures are aligned to the stable core region. (B) Cα RMSD difference (ΔCα RMSD) from the average value (last 25 ns) of the neutral pH simulations. The ΔCα RMSD of the globular domain and HA are colored in gray and blue, respectively. The dotted lines indicate Cα RMSD standard deviations of the neutral pH simulations. (C) Average Cα RMSD of the native sheet (yellow) and inter-strand angle between S1 and S2 (magenta) for the last 25 ns in each simulation. The area within the yellow dotted lines indicates values within one standard deviation of the averaged Cα RMSD of the neutral pH simulations. Dotted lines in magenta indicate the extreme angles in neutral pH simulations.

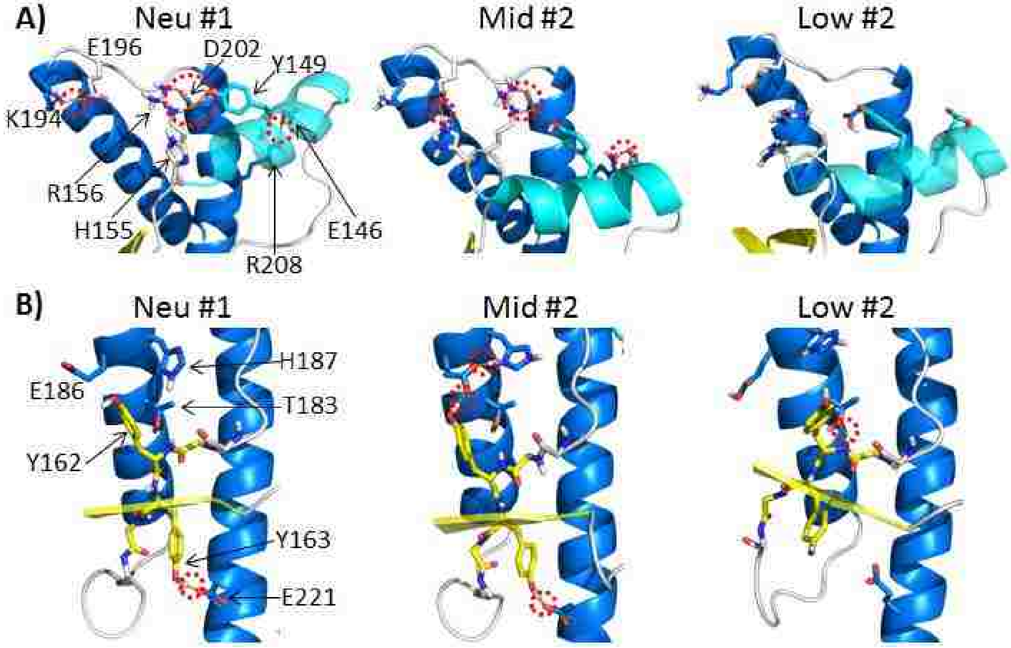

Figure 3.4 Changes in polar contacts at different pH

Structures from neutral pH simulation 1, mid pH simulation 2 and low pH simulation 2 at 30 ns are shown in (A) and (B). Red dotted circles indicate polar contacts. Relevant polar residues are shown as sticks. (A) Relevant polar contacts around HA. HA is colored in cyan. (B) Relevant polar contacts around S2. The backbone of S2 is shown as sticks with carbon atoms colored in yellow.

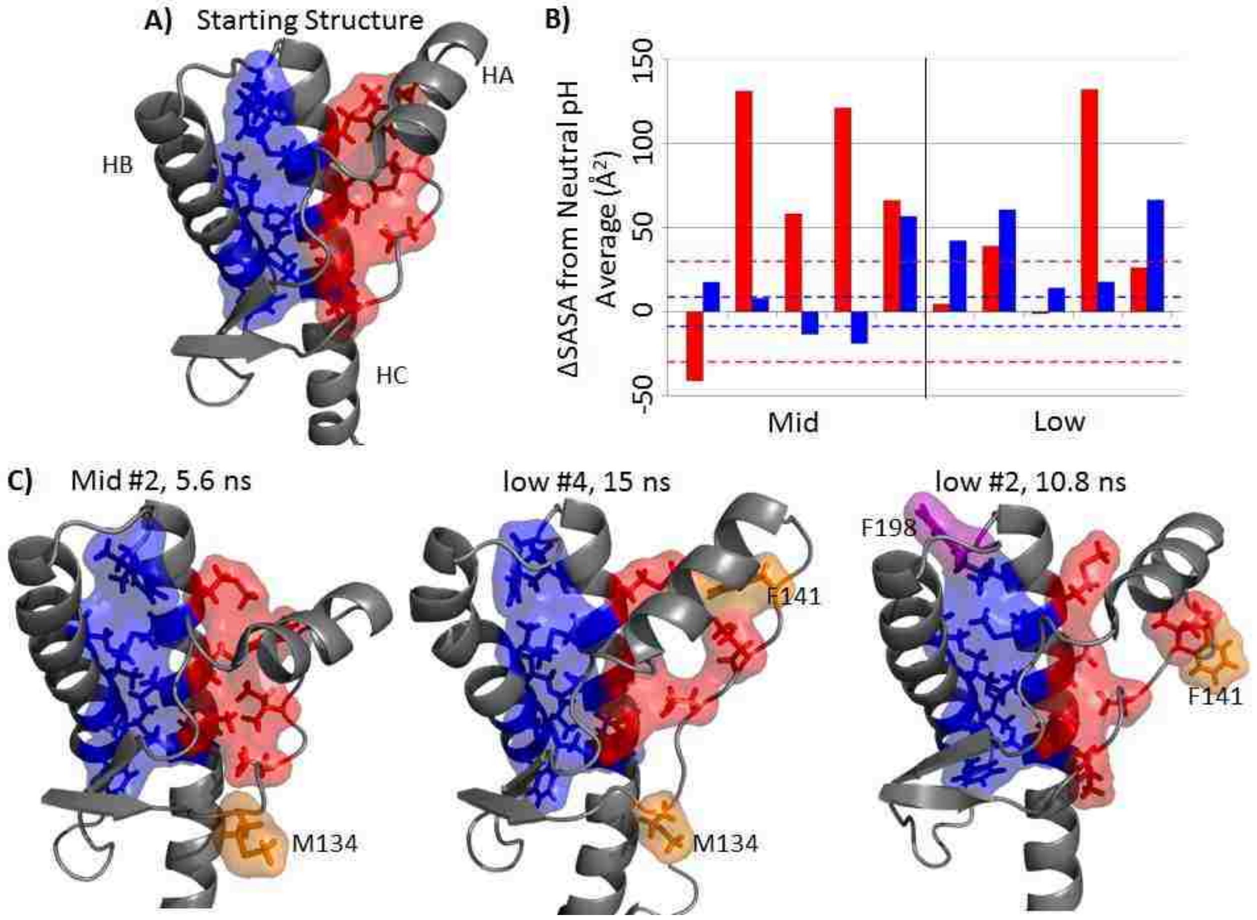

Figure 3.5 Disruption of the hydrophobic core

(A) Two regions of the hydrophobic core: HA-HC (red) includes residues 134, 137, 139, 141, 205, 209 and 213; HB-HC (blue) includes residues 175, 176, 179, 180, 184, 198, 203, 206, 210, 214 and 215. (B) Side chain solvent accessible surface area (SASA) deviation from the averaged neutral pH simulation for the last 25 ns. Red and blue bars correspond to the HA-HC and HB-HC hydrophobic core region, respectively. The area within a pair of dotted lines indicates values within one standard deviation of the averaged SASA of the neutral pH simulations. (C) Representative structures in which significant SASA increased in mid and low pH simulations. Magenta and orange residues are residues that become significantly exposed in the HB-HC region and the HA-HC region, respectively.

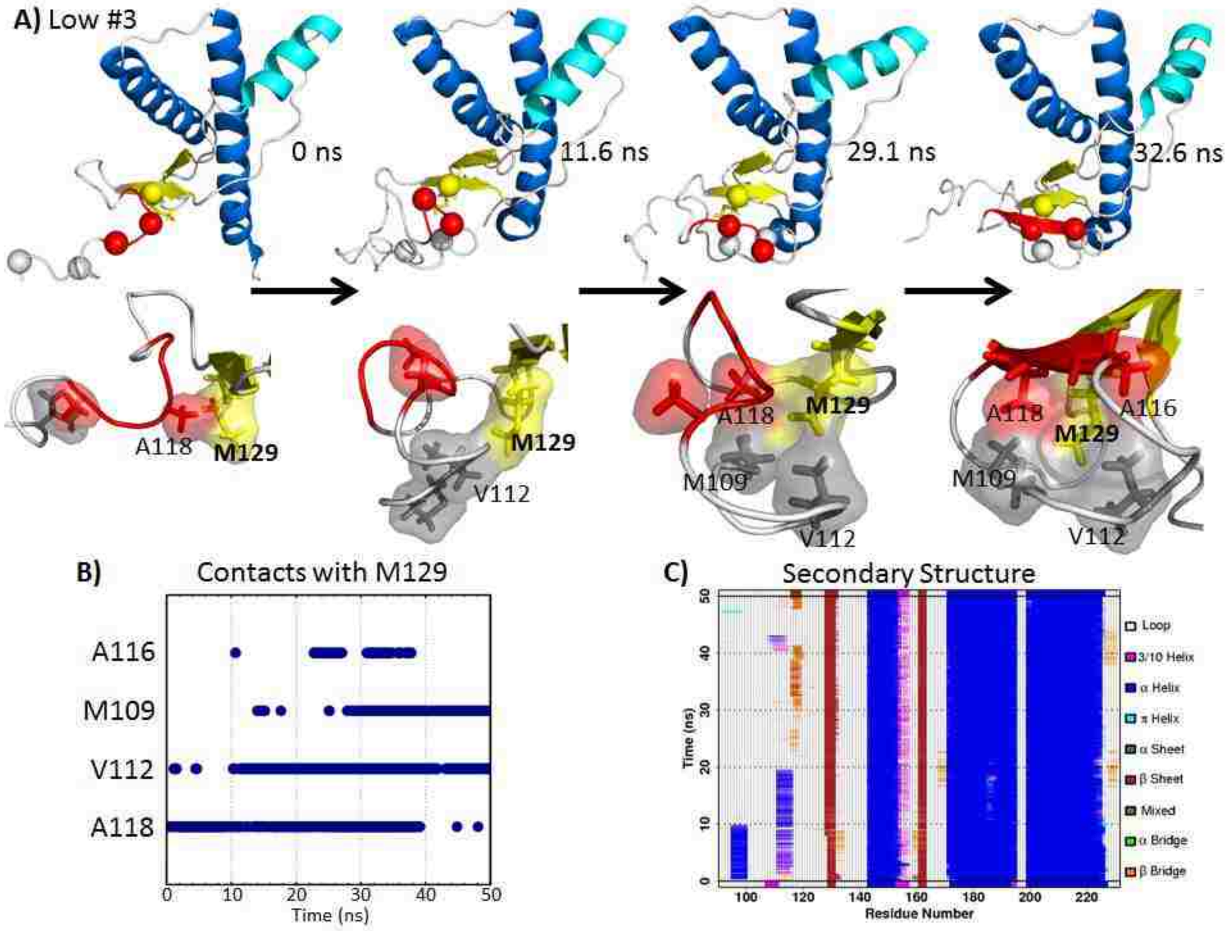

Figure 3.6 Illustration of nonnative β-strand formation at the N-terminus facilitated by N-terminal hydrophobic contacts with M129 in low pH simulation 3

(A) The top panel shows the bovine PrP, with important hydrophobic residues indicated by spheres. Residues in red participate in the nonnative β-strand. The lower panel shows the close-up view of M129 and its neighboring residues. (B) Hydrophobic contacts with M129 over time. (C) PrP secondary structure. Orange and red regions indicate β-structures. A nonnative strand was formed during 30–42 ns.

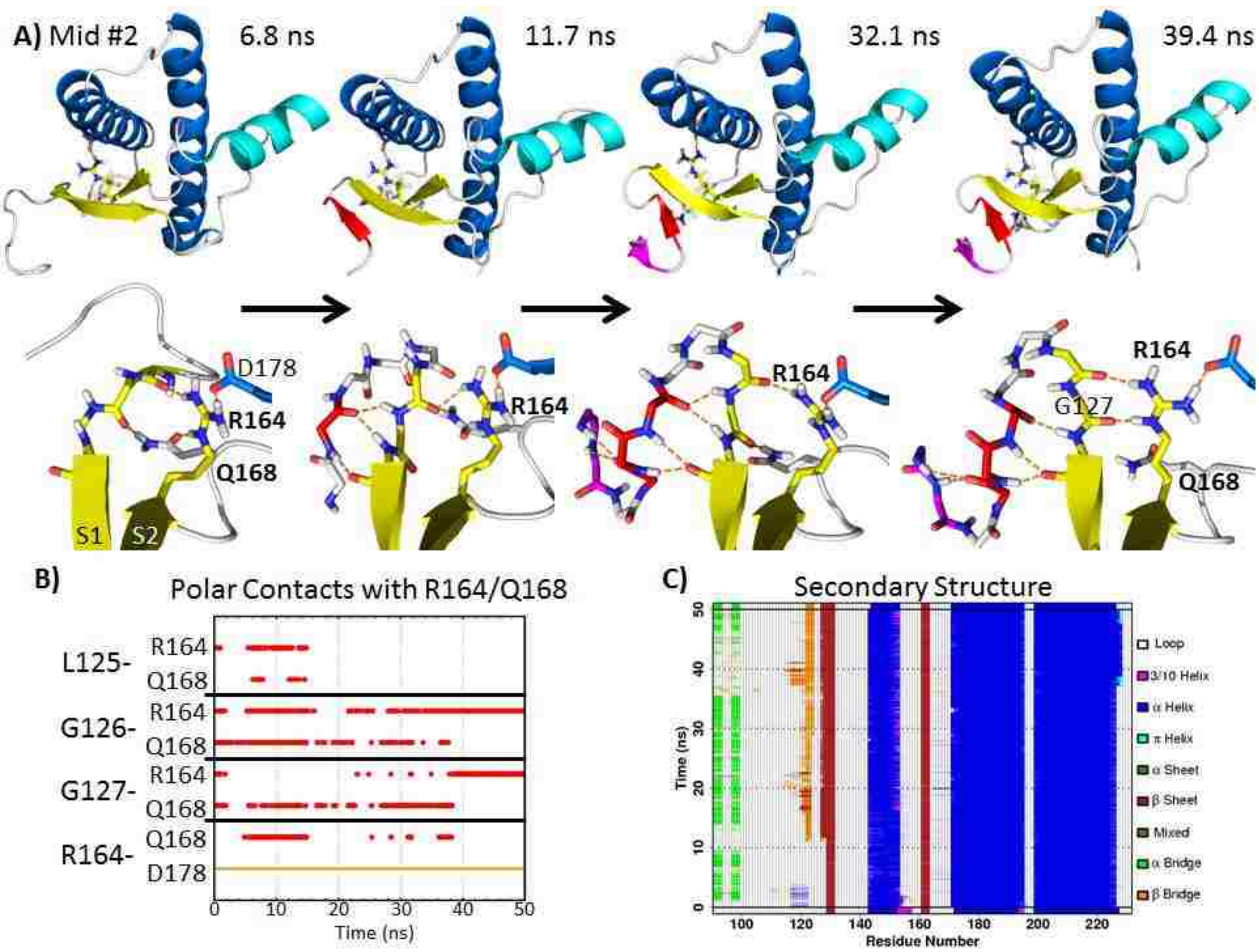

Figure 3.7 Illustration of nonnative strand formation at the N-terminus facilitated by N-terminal polar contacts with side chains of R164 and Q168 in mid pH simulation 2

(A) The top panel shows the PrP construct with the nonnative strands colored in red and magenta. Side chains of R164, Q168 and D178 are shown as sticks. The lower panel shows the close-up view of R164, Q168 and relevant N-terminal residues. (B) Hydrogen bonds and salt bridge formed with R164 or Q168 over time. (C) Analysis of PrP secondary structure. Orange and red regions indicate β-structures. A nonnative strand was formed during 11.7–50 ns.

Chapter 4

SIMULATIONS OF MEMBRANE-BOUND DIGLYCOSYLATED HUMAN PRION PROTEIN

4.1 Summary

Prion diseases are associated with the misfolding of the prion protein (PrP) from its normal cellular form (PrP^C) to its infectious scrapie form (PrP^{Sc}). Posttranslational modifications of PrP *in vivo* can play an important role in modulating the process of misfolding. To gain more insight into the effects of posttranslational modifications on PrP structure and dynamics, we have performed molecular dynamics simulations of diglycosylated human PrP^C bound to a lipid bilayer via a glycophosphatidylinositol anchor. Multiple simulations were performed at three different pH ranges to explore pH effects on structure and dynamics. In contrast to simulations of protein-only PrP^C, no large effects were observed upon lowering the pH of the system. The protein tilted toward the membrane surface in all of the simulations and the putative PrP^{Sc} oligomerization sites became inaccessible, thereby offering a possible protective mechanism against PrP^{Sc}-induced misfolding of PrP^C.

4.2 Introduction

Transmissible spongiform encephalopathies (TSEs) are fatal neurodegenerative diseases in mammals associated with misfolding of the prion protein (PrP). TSEs include a range of diseases in humans and other mammals, such as Creutzfeldt-Jakob disease (CJD) and bovine spongiform encephalopathy (BSE or mad cow disease). These diseases are caused by the misfolding of the prion protein from its native conformation (PrP^C) to a disease-related form

(PrP^{Sc}) (82, 135, 171). PrP^{C} is a glycosylphosphatidylinositol (GPI) anchor membrane-bound protein and it is usually diglycosylated at Asn181 and Asn197 (172, 173). The native structure of PrP^{C} consists of a flexible N-terminal region (residues 23-127) and a structured C-terminal globular domain (residues 128-228). There are three helices - HA (residues 144-154), HB (residues 173-194), and HC (residues 200-228) - and two β-strands – S1 (residues 128-131) and S2 (residues 161-164) - in the structured globular domain (Figure 1.1). PrP^{C} is presented at the cell surface of neurons, and it has been implicated in signal transduction (116, 174, 175) and metal metabolism (19, 176–178).

The central hypothesis of prion diseases is that they are a protein-only disease, whereby the prion protein is the only agent required for propagation and transmission of the disease. Recombinant PrP, which lacks glycans and the GPI anchor, is the primary construct used in experimental studies. However, non-protein moieties affect the disease process *in vivo*. The N-linked glycans influence PrP expression, distribution (within regions of the brain and among different types of neuronal cells) and deposition of PrP^{Sc} *in vivo* (172, 173). The glycans have also been observed to modify the conformation of PrP^{C} and/or affect the affinity of PrP^{C} for a particular strain of PrP^{Sc} (124, 179–181). Nonetheless, based on the protein structure alone, recombinant PrP^{C} appears to be a good model for biologically relevant forms of PrP^{C}, because the structures of diglycosylated human PrP^{C} and recombinant PrP^{C} are similar, as indicated by circular dichroism (CD) and NMR (182).

Most of the molecular dynamics (MD) simulation studies of PrP only focus on the protein-only portion (PrP_{prot}), i.e. the simulations include neither the posttranslational modifications nor the membrane environment. Various computational studies have been performed on PrP_{prot} at acidic pH ranges (44, 64). Experiments indicate that low pH cellular environments, such as endocytic organelles, play a role in misfolding (147, 148). In order to provide a realistic simulation environment of PrP^{C} to determine the pH effects on misfolding, it is necessary to include the non-protein moieties in simulations.

So far there has been only one membrane MD simulation study of the GPI-anchored diglycosylated PrP^{C} (152), in which both PrP_{prot}, and the full construct including the membrane, glycans and GPI anchor (PrP_{mem}) were simulated at neutral and low pH. The simulation began with the protein perpendicular to the membrane to allow for interactions between the two to evolve naturally. However, only a total of 30 ns simulation of PrP_{mem} system was performed at that time. Here we build upon on that work by performing multiple, longer PrP_{mem} simulations that include the glycans, GPI anchor and lipid membrane, so that we can explore the conversion pathway of PrP^{C} and its structural dynamics under physiological conditions. We performed simulations of the PrP_{mem} system in triplicate at low, mid, and neutral pH. Each simulation was 80 ns long, increasing our sampling time from 30 ns to 720 ns. As a result, we have confirmed our earlier findings and observed interactions between the protein and non-protein moieties that potentially modulate conversion of PrP^{C}. We found that the structured C-terminal domain of PrP is more stable with glycans and membrane than without such non-protein moieties. The glycans did not form contacts with the membrane, but the Asn181 glycan formed contacts with the flexible N-terminus of PrP. In addition, PrP in the PrP_{mem} simulations tilted in an angle such that the putative oligomerization sites on PrP were buried against the membrane surface. Our findings shed light on why conversion of PrP^{C} to PrP^{Sc} is more efficient with the bare recombinant protein than with membrane-bound PrP^{C}.

4.3 *Results and Discussion*

The starting structure of the PrP_{prot} system was created using the NMR human PrP^C structure (PDB:1QLX). The missing N-terminal residues 90-127 were added to the structure such that the N-terminus extended away from the structured globular domain to avoid bias in sampling the N-terminus conformation, as described previously (44, 152). The PrP_{mem} system, in addition to the NMR structure, was created by placing the PrP on a phosphatidylcholine (POPC) lipid bilayer (Figure 1.1). The GPI anchor was embedded in the lipid bilayer and attached to the C-terminus of the PrP. Glycans were attached to the glycosylation sites at Asn181 and Asn197. Simulations of both PrP_{prot} and PrP_{mem} systems were performed at neutral, mid and low pH. The pH environment was modeled by altering the protonation states of charged residues (see Materials and Methods). All simulations were performed at 37 $^{\circ}$C.

4.3.1 *Misfolding in Protein-only PrP^C simulations*

PrP_{prot} simulations (without glycans and membrane) at neutral, mid and low pH yielded structures that deviate significantly from the starting structure. Cα root-mean square deviation (RMSD) was used to detect gross conformational changes in simulations. The average Cα RMSD for the globular domain (residues 128-228) for neutral, mid and low pH simulations were 2.12 ± 0.5 Å, 2.59 ± 0.38 Å and 2.96 ± 1.27Å, thus indicating a trend in which the lower the pH, the more the structure changed. One of the major contributors to the increase in Cα RMSD at low pH was the HA helix region: the HA helix along with its preceding loop (S1-HA loop) was displaced from its native position and resulted in significant disruption in hydrophobic contacts (Figure 4.2A,B). Such a conformational change was also observed in previous simulations on human PrP pathogenic mutants (63, 88) and low pH simulations of the human PrP (44). Hydrophobic packing is crucial to protein stability, and disruption of the S1-HA loop packing increases the aggregation tendency of PrP. In addition, detachment of the S1-HA loop from the HC helix is necessary for PrP^{Sc} fibrillation, as indicated in both *in vitro* (106, 107) and *in vivo* (107) disulfide engineering experiments. These experiments support our earlier hypothesis that PrP^{C} misfolding involves the exposure of the hydrophobic S1-HA loop, with the formation of a new hydrophobic strand that is a site for PrP^{Sc}-oligomerization. We denoted this oligomerization site as the E4 strand, since it consistently forms an extended structure in simulations of various PrP species at low pH (51, 52, 54).

In addition to the E4 strand, another nonnative strand (denoted E1) forms at the N-terminus in the PrP_{prot} simulations (Figure 4.2C). The E1 strand was recruited by the native strand S1, and our previous simulations also have formed this E1 strand, which ranges from residues 113-122 (50–52). We have hypothesized that the formation of the E1 strand is another hallmark of PrP misfolding, and that the E1 strand is also a site for PrP^{Sc}-oligomerization. Our results are in agreement with experiments indicating that the PrP peptides within residues 106-127 of the N-terminus aggregate and form β-sheet-rich oligomers and fibrils (183–186). Interestingly, a recent crystal structure of a PrP (in complex with a PrP^{Sc}-inhibitory nanobody) also has an E1 strand consisting of N-terminal residues 118-122 (Figure 4.2C) (53), thus lending further support to our MD-derived misfolded structures.

In order to interpret our MD-derived misfolded PrP^{Sc} structures in the context of the oligomerization process, we have previously proposed the spiral model. In the spiral model, simulated misfolded PrP^{Sc} structures were assembled by docking the E1 strand of one monomer to an adjacent neighbor at the E4 strand, and thus the monomers are arranged along a three-fold screw-axis (Figure 4.3A,B). The spiral model has been previously validated by various experimental data (51, 54), and recent experimental data on PrP^{Sc} soluble oligomers lend further support to our model (63).

Although misfolding was observed in the PrP_{prot} simulations, the experimental data suggest that the membrane-bound PrP^{C} are more resistant to misfolding, since neither acidic treatment (187) nor denaturants (188) have been shown to induce misfolding or oligomerization of membrane-bound PrP^{C}. Furthermore, unlike the bare recombinant PrP, membrane-bound PrP^{C} is resistant to PrP^{Sc}-induced misfolding unless it is released from membranes by phospholipase C digestion (187, 189). We hypothesize two possible mechanisms by which the posttranslational modifications and the membrane environment contribute to the misfolding-resistance: (1) the glycans and membrane environment provide contacts that stabilize the native structure of PrP^{C}; and (2) the glycans and membrane environment shield the putative oligomerization sites, strands E1 and E4, thereby providing a steric barrier to misfolding and oligomerization. In the following results from our PrP_{mem} simulations, we evaluate the stability of the PrP using Cα RMSD, NOE satisfaction and contact analyses. After that, we also detail the contacts and relative positions between PrP and the glycans, and between PrP and the membrane. We conclude by theorizing how the glycans and the membrane contribute to the protective mechanisms against PrP misfolding.

4.3.2 *Conformational changes in PrP$_{mem}$ simulations*

Gross conformational changes of PrP in the PrP$_{mem}$ simulations are reflected in the Cα RMSD relative to the starting structure. In all pH regimes, the average Cα RMSDs of the globular domain of PrP (residues 128-228) were within the range of 1.5-2.0 Å (Figure 4.4), reflecting the retention of the native-like globular domain structure. The Cα root-mean square fluctuations (RMSF) about the average structure after equilibration reflect the mobility for each residue in the protein. The Cα RMSF values of the residues in the globular domain were less than 2.0 Å in all pH regimes, whereas those of the residues in the flexible N-terminus fall in the range of 2.0 – 5.0 Å (Figure 4.5).

4.3.3 *NOE satisfaction by PrP$_{mem}$ simulations*

Using our previously described method (44), the PrP structures in the PrP$_{mem}$ simulations were compared to the Nuclear Overhauser Effect (NOE) restraints of the human PrP E200K mutant (190), which is structurally similar to wild type human PrP. The NOE restraints are available for residues 125-230, which cover the structured, helical domain of PrP. Structures from the neutral, mid, and low pH PrP$_{mem}$ simulations satisfied 88% of the 2641 NOEs, in all pH regimes. Therefore, PrP structures from our PrP$_{mem}$ simulations are similar to the NMR structures of the human recombinant PrP regardless of the pH environment. This is in agreement with CD experiments that confirm that PrP^{C} retains a helix-rich native structure when bound to POPC vesicles (191).

4.3.4 *Acidic pH effects on PrP$_{mem}$ simulations*

A few contact differences were observed in mid and low pH simulations compared to the neutral pH simulations (Table 3.1). The mid pH simulations lost the contact Glu152-His155, but gained His140-Asp147. These two contact changes were caused by the protonation of histidine residues at mid pH. As for the low pH simulations, only two residue contacts were significantly disrupted: Leu125-Ile182 and Tyr157-Phe198. The contact Leu125-Ile182 was affected primarily due to the loss of a hydrogen bond between side chains of Tyr128 and Asp178. As for the contact Tyr157-Phe198, Phe198 became more exposed and lost hydrophobic packing with Tyr157. Other than changes in contacts, residues 154-157 at the C-terminal of HA lost helicity in both the mid and low pH simulations compared to neutral pH (Table 3.1). These minor structural and intramolecular contact changes were all directly affected by the protonated residues at mid and low pH. These contact changes were localized and did not have a significant impact on the structural, as indicated by globular Cα RMSD (Figure 4.4). Our results are consistent with experiment, which indicates that low pH misfolding is inefficient for membrane-bound PrP (187).

4.3.5 *PrP$_{mem}$ vs PrP$_{prot}$: Major difference in intramolecular interactions*

There were three PrP regions with significant contact differences between PrP$_{mem}$ and PrP$_{prot}$: the Phe198 hydrophobic pocket, the native sheet packing with the HB and HC helices, and the packing between HC and the S1-HA loop. A list of relevant contact occupancies are shown in (Table 4.2). Overall, the contacts in the PrP$_{mem}$ simulations were much more stable than those in PrP$_{prot.}$ These three areas that differ are discussed in detail below.

In the PrP_{mem} simulations, Phe198 was buried and its average side chain solvent accessible surface areas (SASAs) for neutral, mid, and low pH simulations were only 4, 13, and 19 Å^2, respectively. On the other hand, the SASAs of Phe198 in the PrP_{prot} simulations were at least three to four times greater (Figure 4.6). As Phe198 became exposed, the contacts between Phe198 and Met206 were lost in the mid and low pH PrP_{prot} simulations (Table 4.2). The exposure of Phe198 was accompanied by the formation of the nonnative His187-Asp202 salt bridge. The side chains of His187 and Asp202 occupied the native side chain position of Phe198 (Figure 4.7A). This nonnative salt bridge kept the side chain of Phe198 in a solvent exposed conformation, which is consistent with our previous PrP_{prot} simulations (44). On the other hand, in all PrP_{mem} simulations, Phe198 retained stable core contacts with neighboring residues, including His187 and Met206. The side chain motion of Phe198 was deterred by the bulky glycan attached to Asn197. As a result, the side chain of Phe198 was always buried in between HB and HC in all PrP_{mem} simulations.

In all PrP_{mem} simulations, the native S2 sheet was tightly packed to HB and HC, such that Thr183 formed a stable contact with Gln160 (Figure 4.7B). The residue contact between Gln160 and Met213 on HC was populated on average >80% of the time in the neutral and mid pH PrP_{mem} simulations (Table 3.1), but such contact was less stable in the low pH simulations (36% occupancy). On the other hand, all of the PrP_{prot} simulations, regardless of pH, showed a significant loss in both Gln160-Thr183 and Gln160-Met213 contacts. Other than the packing between S2 and the helices HB and HC, there were two hydrogen bonds that contributed to the stability of this region: Tyr128-Asp178 and Tyr162-Thr183. The side chain of Tyr128 on S1 stabilized the native sheet by hydrogen bonding to the side chain of Asp178 on HB (Figure

4.7B). As for the side chain of Thr183, it hydrogen bonded with the backbone amide of Tyr162 (Figure 4.7B). These hydrogen bonds were more prevalent in PrP_{mem} simulations than PrP_{prot} simulations. Overall, the native sheet in PrP_{mem} formed stable packing interactions and hydrogen bonds while such interactions were lost in PrP_{prot} simulations.

Contacts in the S1-HA loop were more variable due to the conformational flexibility of this loop. One of the relatively robust contacts formed in PrP_{mem} simulations was Arg136-Val209, in which the hydrophobic portion of the side chain of Arg136 packed against the side chain of Val209 on HC (Figure 4.7C). In PrP_{prot}, however, this contact was diminished and highly variable across simulations. Such loss of contacts between S1-HA loop and HC was expected, since the HA helix of the low pH PrP_{prot} simulations was highly mobile and occasionally detached from HC (Figure 4.8).

4.3.6 *Interactions between the membrane and the flexible N-terminus*

In all PrP_{mem} simulations (except for the third neutral pH run), the flexible N-terminus (residues 90-127) formed contacts with the membrane surface (Figure 4.9). In two separate simulations, His96 and Lys101 each formed long-lasting salt bridges with the phosphate groups on the membrane surface (Figure 4.10A and B). These two positively charged residues are within the residues 90-110, which are one of the charged clusters of PrP (192). Charge clusters of PrP are important for electrostatic interactions involved in membrane association (193). At acidic pH, PrP binds to anionic lipids with higher affinity (194). The pH effect was reflected in our mid pH simulation in which the doubly-protonated His96 formed a stable salt bridge with a phosphate group on the membrane (Figure 4.10A), whereas the ε-protonated histidine residues in the neutral pH simulations did not form such long-lasting contacts with the phosphates on the membrane surface.

4.3.7 *Interactions between the glycans and the flexible N-terminus*

The N-terminus of PrP interacted with the Asn181 glycan via Lys residues, but not with the Asn197 glycan. For example, in neutral pH simulation 3, Lys101 formed stable contacts with the Asn181 glycan (Figure 4.11A), preventing the N-terminus from forming contacts with the membrane (Figure 4.9). At mid pH, Lys104 also formed stable contacts with the Asn181 glycan in a similar conformation (Figure 4.11B). At low pH, Lys104 bound to the Asn181 glycan in a conformation different from that of the neutral and mid pH simulations, but with the same effect (Figure 4.11C).

Such consistent interactions between lysine residues and the Asn181 glycan were surprising findings and heretofore unrecognized. However, it is known that the charge clusters at the flexible N-terminus of PrP are important for binding glycosaminoglycans (GAGs), such as heparin, chondroitin sulfate, and hyaluronic acid (195). Given the similar constituents of GAGs and glycans, it is reasonable to expect that the charge cluster of the flexible N-terminus can bind to the glycans, as indicated in our simulations. Glycosylation of PrP impedes the conversion efficiency in *in vitro* conversion assays (196). While these large glycans can sterically inhibit PrP^{Sc}-induced misfolding, our results suggest that glycans can also bind to N-terminal lysine residues, thereby deterring the N-terminus from forming the E1 strand, which is a hallmark for misfolding. Other than retardation of the misfolding process, glycans also play a complicated role in prion propagation (196). Given that the glycans can form stable interactions with the flexible N-terminus of PrP, different glycans may induce different N-terminal conformations, thus influencing strain-specific prion propagation, which is sensitive to conformational changes in PrP^{Sc}.

4.3.8 *Tilting of the structured C-terminal domain on the membrane*

In all of the PrP_{mem} simulations, PrP tilted toward the membrane. For example, the angle between HC and the membrane surface dropped from 90 to ~30° by the end of the simulations (Figure 4.12A and Figure 4.13). This tilting motion buried the putative E1 and E4 oligomerization sites on the membrane surface. Exposure of residues 135-140 (the E4 region) was probed, and in low pH simulation 1, as an example, its exposure dropped from ~500 $Å^2$ to < 200 $Å^2$ by 45 ns (Figure 4.12A). This significant reduction was due to the tilting motion of PrP, which buried the E4 epitope (Figure 4.12B). The distance between the E4 region and the membrane surface was also measured (Figure 4.12A). This tilted conformation was stable and buried the E4 epitope around 45 ns and remained as such until the end of the simulation. The other putative oligomerization site, the E1 strand, was formed only in low pH simulation 3 (Figure 4.14). However, with a 30° tilt, the E1 strand was buried on the membrane surface. We hypothesize that the tilting motion of the membrane-bound PrP^C retards PrP^{Sc}-induced misfolding by masking putative oligomerization sites on PrP^C (Figure 4.15). Experiments broadly support this hypothesis, given that membrane-bound PrP is more resistant to misfolding than free PrP (187, 188), but more direct experimental studies of these regions would be helpful.

4.4 *Conclusions*

Overall, the $\mathrm{PrP_{mem}}$ simulations were extremely stable and preserved a native-like $\mathrm{PrP^C}$ structure in all pH regimes, unlike the $\mathrm{PrP_{prot}}$ simulation of free unglycosylated $\mathrm{PrP^C}$. In most of $\mathrm{PrP_{mem}}$ simulations, the flexible N-terminus formed sporadic contacts with the membrane except for a few lysine and histidine residues in the N-terminus that formed stable salt bridges with the phosphate groups on the membrane. The glycans may modulate the misfolding process by interfering with the E1 formation at the N-terminus through direct contacts with lysine residues at the N-terminus. The tilting motion of membrane-bound PrP buried the E4 and E1 regions, both of which are putative oligomerization sites. This led us to hypothesize that the tilted conformation of membrane-bound $\mathrm{PrP^C}$ protects critical regions of $\mathrm{PrP^C}$ and deters $\mathrm{PrP^{Sc}}$-induced misfolding.

4.5 *Materials and Methods*

4.5.1 *Starting structures of PrP_{prot} and PrP_{mem}*

For $\mathrm{PrP_{prot}}$, the starting coordinates for the globular region (residues 125-228) were obtained from the human NMR structure (73) (PDBID: 1QLX). The NMR structure was then extended to include residues 90-230, because this construct consist of regions that are critical to capture misfolding, especially at the N-terminus. In order to model residues 90-230 of PrP, the missing N-terminal residues were added to the structure such that the N-terminus extended away from the protein to avoid bias, as described previously (44, 152). To construct $\mathrm{PrP_{mem}}$, non-protein moieties of the system were added to $\mathrm{PrP_{prot}}$ system as described previously (152). Briefly, two 13-residue glycans were attached to Asn181 and Asn197, and the GPI anchor was attached to the C-terminus of PrP. The GPI anchor was embedded in the POPC membrane bilayer, which consists of 335 lipid-molecules. The lipid bilayer was modelled based on the structure built by the Schulten group (197).

4.5.2 *MD simulation*

For both $\mathrm{PrP_{prot}}$ and $\mathrm{PrP_{mem}}$ simulations, the starting structures were solvated in a pre-equilibrated rectangular water box (131) with a density of 0.993 g/ml, which is the experimental density for water at 37 °C (168). Detailed methods of the $\mathrm{PrP_{prot}}$ simulations have been described previously (44, 63). For the $\mathrm{PrP_{mem}}$ system simulations, the periodic box, which extended >20 Å from any solute atom above and below, had the following dimension: 94 × 98 × 147 Å. Neutral, mid, and low pH ranges were modelled by altering protonation states of histidine, aspartate, and glutamate residues, as described previously (44). The Levitt et al. force field (130) was employed for all MD simulations, and simulations were performed at 37 °C using *in lucem* molecular mechanics (*il*mm) (129) and standard procedures (132). For the $\mathrm{PrP_{mem}}$ system, triplicate simulations were performed for each pH, and each simulation was performed for 80 ns. For the $\mathrm{PrP_{prot}}$ system, five simulations were performed for each pH regime, and each simulation was 50 ns long.

4.5.3 *MD simulation analysis*

Analyses such as, solvent accessible surface area (SASA), definition of secondary structure of proteins (DSSP), Cα root-mean square deviation (RMSD), and Cα root-mean square fluctuation (RMSF) were performed with *il*mm as previously described (44). NOE restraint data (BMRB 4641) were obtained from human PrP E200K (190). NOE restraint satisfaction of

PrP_{mem} simulations was measured for the combined simulations in each pH regime with *il*mm. An NOE restraint was considered satisfied if the $<r^{-6}>$ weighted distance between the nearest protons associated with the NOE was less than the upper bound or 5 Å, whichever is greater. The HC tilt angle was measured between a vector fit through Cα atoms of residues 200-214 on HC and the x-y plane. The x-y plane was an approximation of the membrane surface. Heavy atom contacts were considered intact when two carbon atoms were ≤ 5.4 Å apart or when other interacting heavy atoms were ≤ 4.6 Å apart. The population of a contact (percentage time present over the simulation) was averaged across simulation replicates for each pH regime. The 40-80 ns of PrP_{mem} simulations and the 10-50 ns of PrP_{prot} simulations were used to calculate the average contact occupancies.

Table 4.1 Population of contacts between residues, and helicity of C-terminal residues of HA

Contacts	Neutral	Mid	Low
140sc-147sc*	0% ± 1%	100% ± 0%	14% ± 17%
152-155	91% ± 15%	3% ± 3%	41% ± 38%
125-182	100% ± 0%	70% ± 52%	12% ± 20%
128sc-178sc*	90% ± 18%	84% ± 27%	32% ± 55%
157-198	100% ± 1%	33% ± 58%	1% ± 1%
Helicity	Neutral	Mid	Low
154	75% ± 8%	26% ± 35%	41% ± 48%
155	22% ± 12%	2% ± 3%	0% ± 0%
156	20% ± 13%	1% ± 2%	0% ± 0%
157	16% ± 12%	1% ± 2%	0% ± 0%

* Polar contacts between side chain (sc) residues only.

Table 4.2 Population of contacts for PrP$_{mem}$ and PrP$_{prot}$ simulations

Contacts		PrP$_{mem}$			PrP$_{prot}$		
		Neutral	Mid	Low	Neutral	Mid	Low
Phe198 hydrophobic pocket	198-156	100 ± 0%	34 ± 57%	82 ± 19%	67 ± 42%	36 ± 46%	1 ± 1%
	198-187	100 ± 1%	100 ± 0%	99 ± 1%	78 ± 28%	13 ± 16%	40 ± 39%
	197-192	48 ± 45%	90 ± 17%	100 ± 0%	60 ± 49%	25 ± 36%	1 ± 1%
	198-206	100 ± 0%	100 ± 0%	99 ± 1%	79 ± 30%	30 ± 42%	23 ± 17%
	187sc-202sc*	0 ± 0%	0 ± 0%	0 ± 0%	1 ± 2%	46 ± 46%	23 ± 29%
	187sc-156mc*	100 ± 0%	100 ± 0%	73 ± 24%	78 ± 12%	30 ± 44%	54 ± 50%
Native sheet packing with HB and HC	179-128	96 ± 8%	62 ± 54%	33 ± 58%	6 ± 13%	9 ± 14%	0 ± 0%
	128sc-178sc*	78 ± 38%	64 ± 56%	22 ± 38%	9 ± 20%	28 ± 38%	0 ± 0%
	183-160	90 ± 12%	95 ± 8%	82 ± 13%	17 ± 13%	5 ± 5%	20 ± 13%
	183sc-162mc*	83 ± 8%	80 ± 9%	87 ± 14%	54 ± 22%	56 ± 24%	73 ± 41%
	160-213	83 ± 15%	85 ± 8%	36 ± 56%	42 ± 15%	15 ± 13%	21 ± 16%
S1-HA loop contacts	134-131	41 ± 51%	100 ± 0%	66 ± 57%	31 ± 32%	10 ± 11%	40 ± 30%
	134-160	54 ± 51%	97 ± 4%	65 ± 57%	34 ± 19%	10 ± 9%	31 ± 29%
	136-209	90 ± 17%	100 ± 0%	67 ± 58%	57 ± 29%	10 ± 11%	35 ± 43%

* Contacts between side chain (sc) or main chain (mc) of the residues.

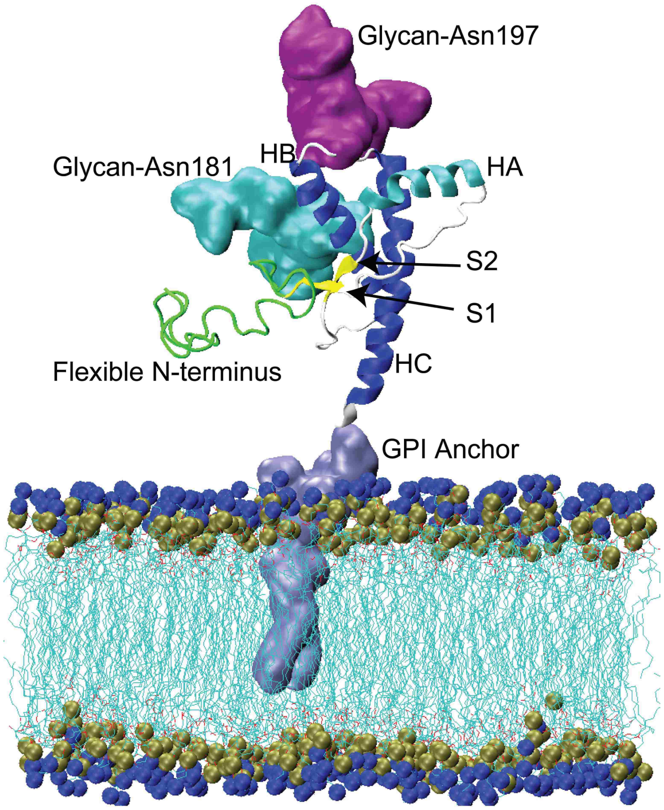

Figure 4.1 PrP$_{mem}$ system used for MD simulations

Cyan and purple colored surfaces are the glycans attached to Asn181 and Asn197, respectively. The GPI anchor is represented as the light-blue surface. HA (residues 144-154), N-terminus (residues 90-127), S1 and S2 (residues 128-131 and 161-164) are colored in cyan, green, and yellow, respectively. The HB (residues 173-194) and HC (residues 200-228) helices are in blue. Remaining loop regions are colored in gray. The carbon and oxygen atoms of the phosphatidylcholine (POPC) molecules are indicated as thin cyan and red lines, respectively. Nitrogen and phosphorus atoms are indicated as blue and brown spheres respectively.

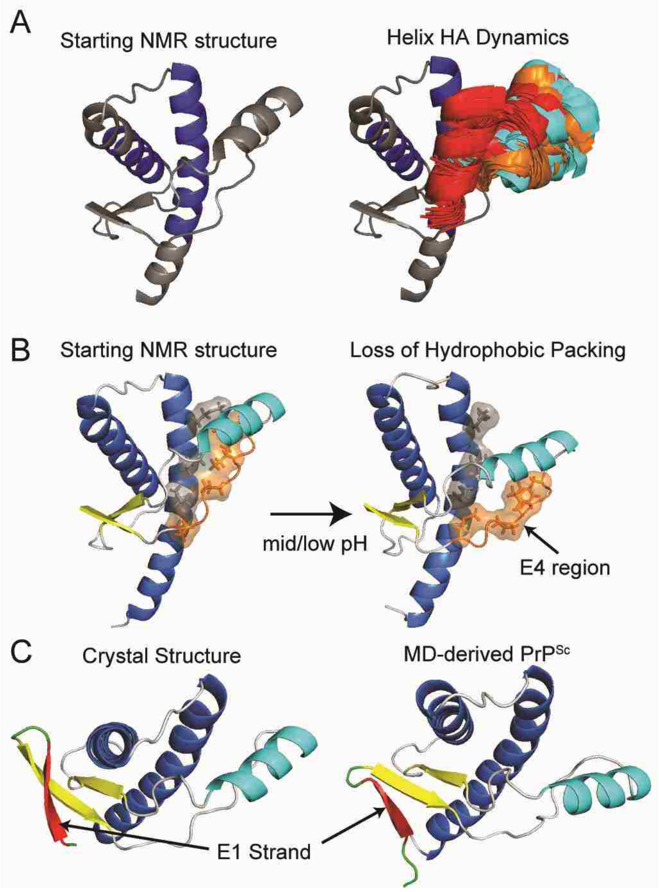

Figure 4.2 Misfolding in PrP$_{prot}$ simulations

(A) Left: starting structure; Right: helix HA structure for the last 25 ns of all PrP$_{prot}$ simulations at 1 ns granularity. Structures were aligned to the starting structure at the stable core residues 174-186 and 200-219, as shown in blue. Cyan, orange, and red cartoons represents structures from neutral, mid and low pH simulations, respectively. (B) Hydrophobic residues 134, 137, 139, 141, 205, 209 and 213 are shown with translucent surface and stick representations of the side chains. E4 region is colored in orange. Left: starting structure; Right: mid pH simulation 3 at 49.9 ns. (C) Formation of the E1 strand (in red). Left: crystal structure (PDBID: 4KML (53)); Right: a representative MD-derived misfolded structure from PrP$_{prot}$ simulations.

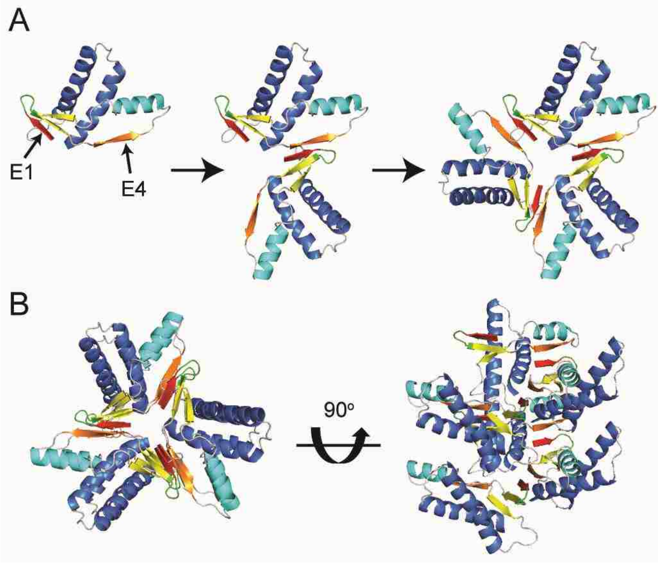

Figure 4.3 The spiral model

The spiral model. (A) Using an MD-derived PrP^{Sc} to construct a threefold screw-axis spiral model. The oligomerization site occurs between the E1 and E4 strands of the adjacent monomer. (B) Vertical and horizontal views of a hexameric spiral model.

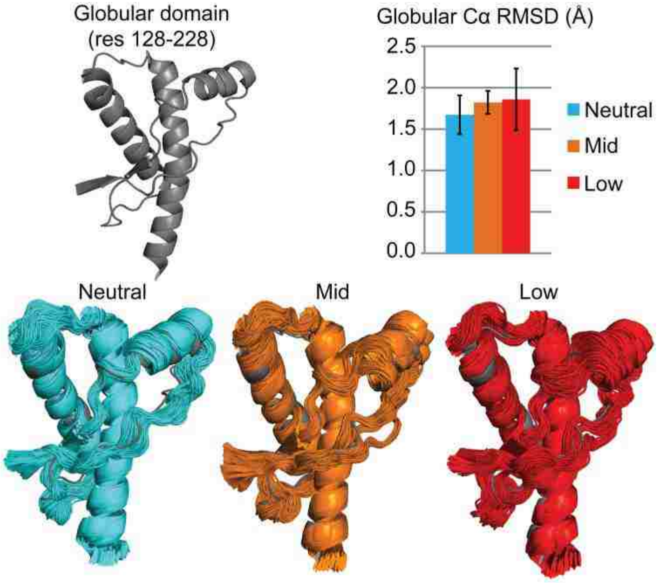

Figure 4.4 Average Cα RMSD of the globular domain

Average Cα RMSD of the globular domain (residue 128-228) from 40-80ns for all $\mathrm{PrP}_{\mathrm{mem}}$ simulations at neutral (cyan), mid (orange), and low (red) pH. Standard deviation is shown for each average Cα RMSD (n = 3 for each pH). Structures from all $\mathrm{PrP}_{\mathrm{mem}}$ simulations (every 1ns frame from 40-80 ns) are aligned to the starting globular domain structure.

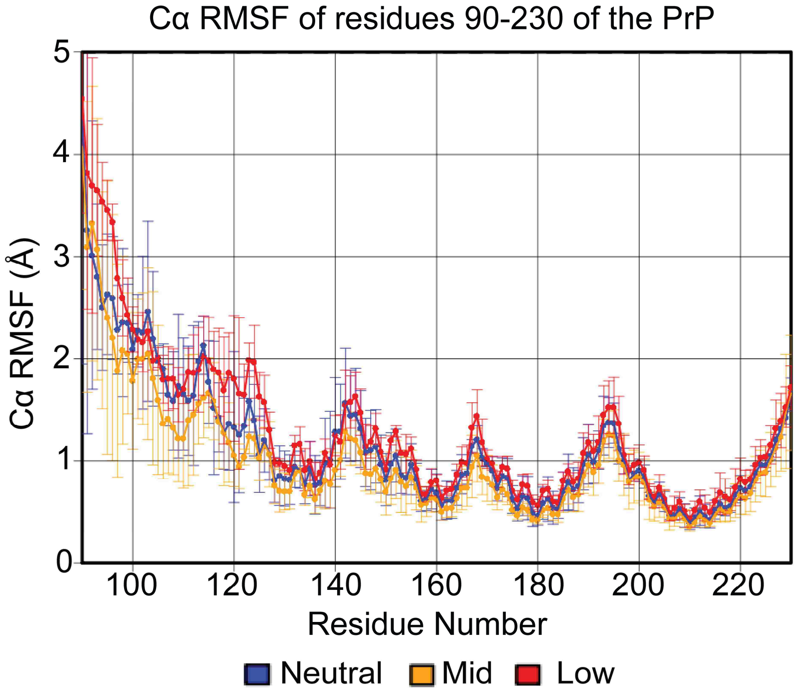

Figure 4.5 Cα RMSF of PrP$_{mem}$ simulations

Cα RMSF of neutral, mid, and low pH PrP$_{mem}$ simulations. Standard deviations are computed over the triplicate simulations for each pH.

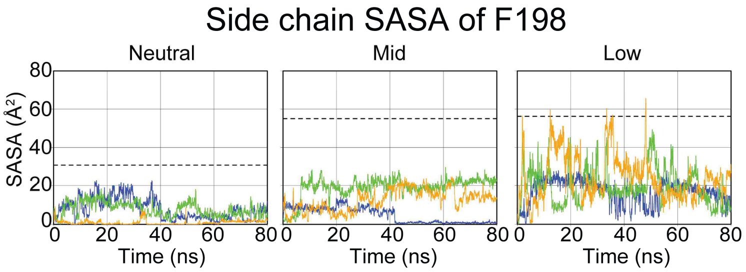

Figure 4.6 Side chain SASA of Phe198 for PrP$_{mem}$ simulations

Side chain SASA of Phe198 for PrP$_{mem}$ simulation 1 (blue), 2 (green), and 3 (orange). The dotted lines are average values (25-50 ns) of PrP$_{prot}$ simulations at neutral, mid, and low pH (for each pH, n = 3 for PrP$_{mem}$, and n = 5 for PrP$_{prot}$).

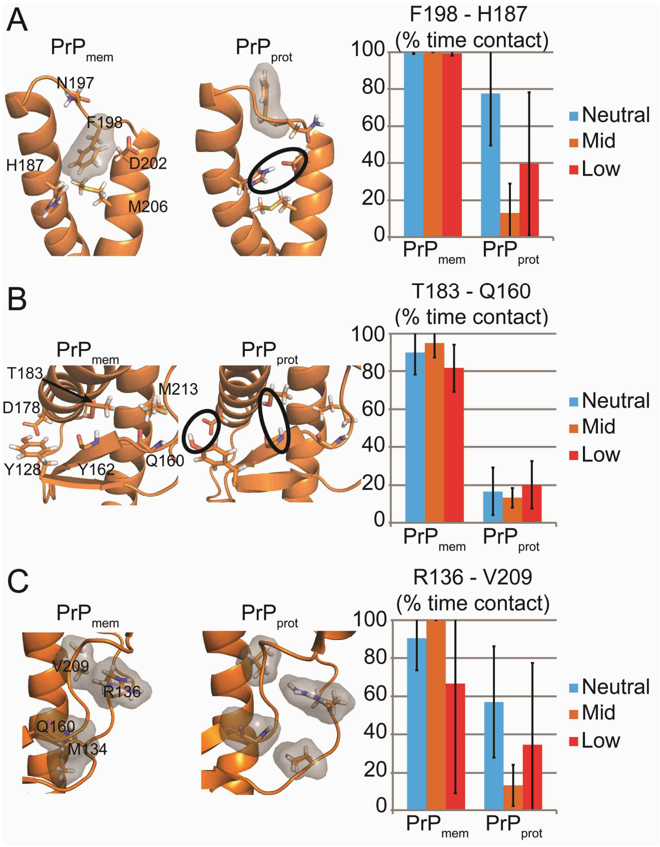

Figure 4.7 Differences between PrP$_{mem}$ and PrP$_{prot}$ simulations

Structures are taken from mid pH simulations. Relevant residue contact occupancies are displayed. Standard deviations are computed for both PrP$_{mem}$ and PrP$_{prot}$ (For each pH, n = 3 for PrP$_{mem,}$ and n = 5 for PrP$_{prot}$). (A) Phe198 hydrophobic pocket. The black oval indicates the nonnative salt bridge that formed in PrP$_{prot}$ simulation. (B) Native sheet packing with HB and HC. The black ovals indicate the loss of hydrogen bonds in PrP$_{prot}$ simulations. (C) S1-HA loop packing with HC. The S1-HA loop detaches from HC and loses hydrophobic packing in PrP$_{prot.}$

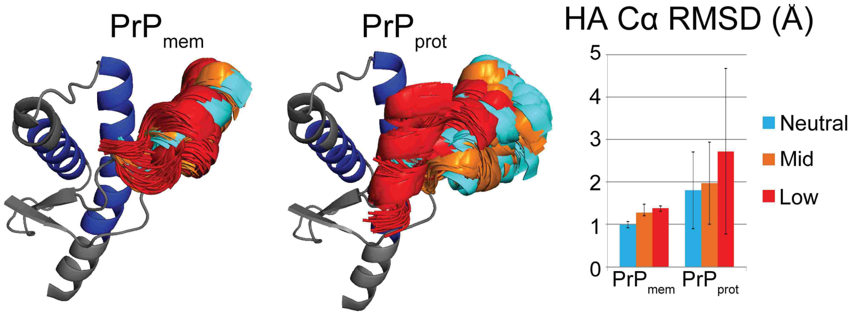

Figure 4.8 HA displacement from the native structure

Structures from 40-80 ns of the PrP_{mem} simulations and 25-50 ns PrP_{prot} simulations were aligned to the dark blue region (residues 174-186 and 200-219) of the neutral pH starting structure. Average Cα RMSD of HA was calculated for PrP_{mem} and PrP_{prot} simulations (for each pH, n = 3 for PrP_{mem}, and n = 5 for PrP_{prot}). Overall, HA displacement was more variable in PrP_{prot} simulations than in PrP_{mem} simulations.

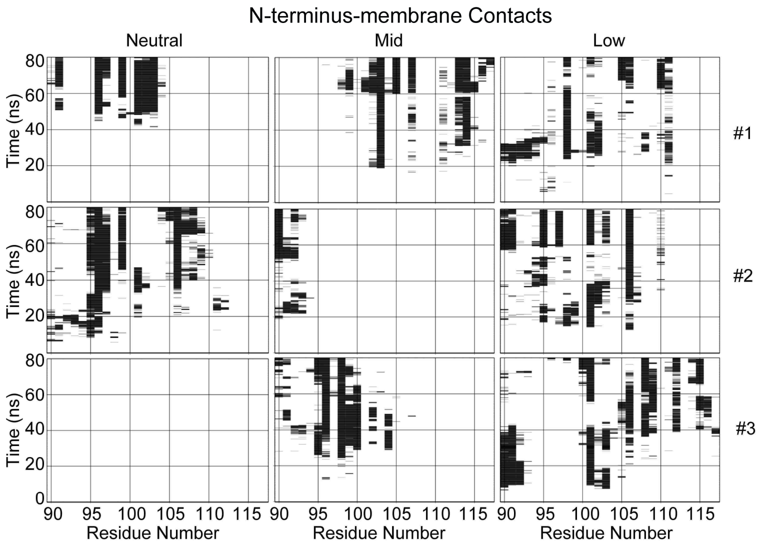

Figure 4.9 Contacts between N-terminus and the membrane surface

Contacts between N-terminal residues 90-117 and the membrane surface for all PrP_{mem} simulations.

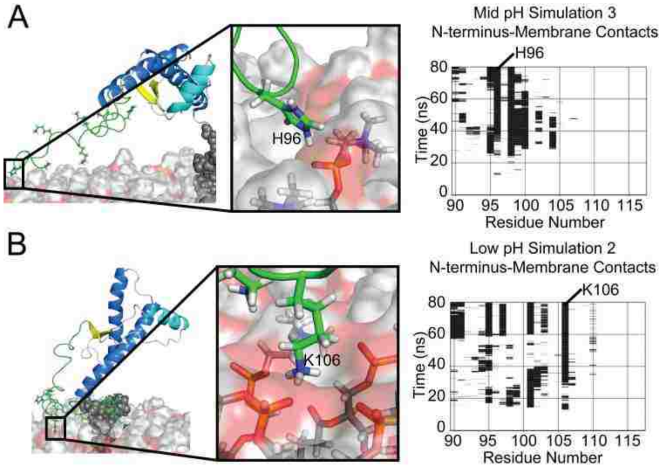

Figure 4.10 Contacts between N-terminus and the membrane surface at mid and low pH

Contacts between residues 90-117 and the membrane are shown on the right. (A) Structure of membrane-bound PrP in mid pH simulation 3 at 80 ns. His96 formed a stable salt bridge with phosphate head group on the membrane. (B) Structure of membrane-bound PrP in low pH simulation 2 at 80 ns. Lys106 formed stable salt bridge with phosphate head group on the membrane.

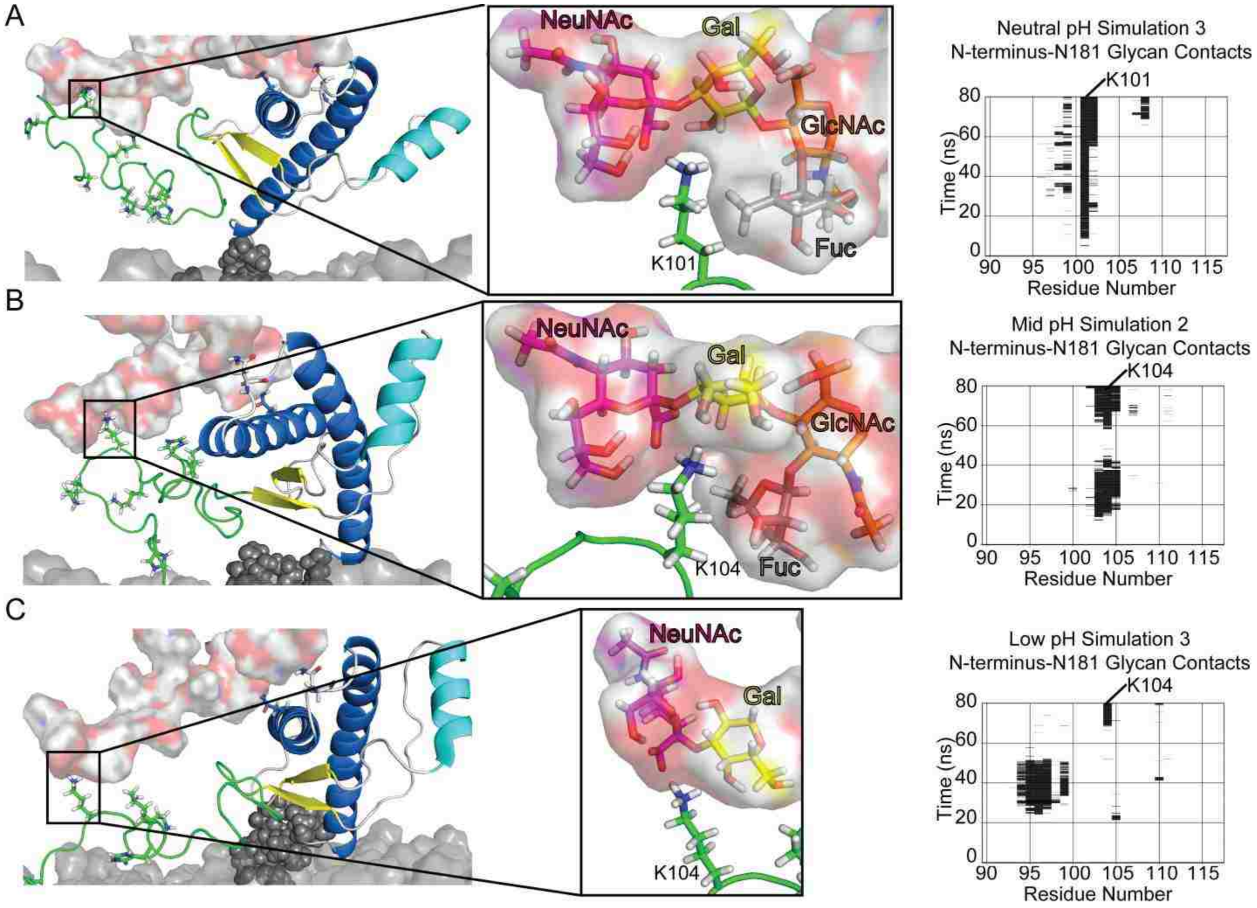

Figure 4.11 Contacts between the Asn181 glycan and lysine residues at the flexible N-terminus

Contacts between residues 90-117 and the Asn181 glycan are shown in the right column. Relevant lysine residues, *N*-acetylneuraminate (NeuNAc), galactose (Gal), *N*-acetylglucosamine (GlcNAc), and fucose (Fuc) are shown as sticks. (A) Neutral pH simulation 3 at 80 ns. (B) Mid pH simulation 2 at 80 ns. (C) Low pH simulation 3 at 80 ns.

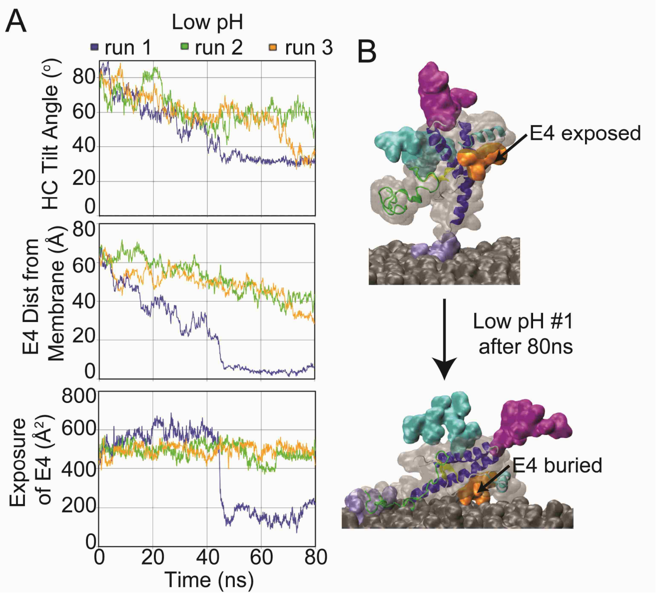

Figure 4.12 PrP tilting on the membrane burying the E4 putative oligomerization site

(A) HC tilt angle, distance between the center of mass of E4 and the membrane surface, and exposure of E4 measured with a probe with a 4 Å radius, for all low pH PrP_{mem} simulations. The HC tilt angle was measured between a vector that fits through Cα atoms of residue 200-214 of HC and the membrane surface. (B) Before and after the tilting motion in low pH simulation 1.

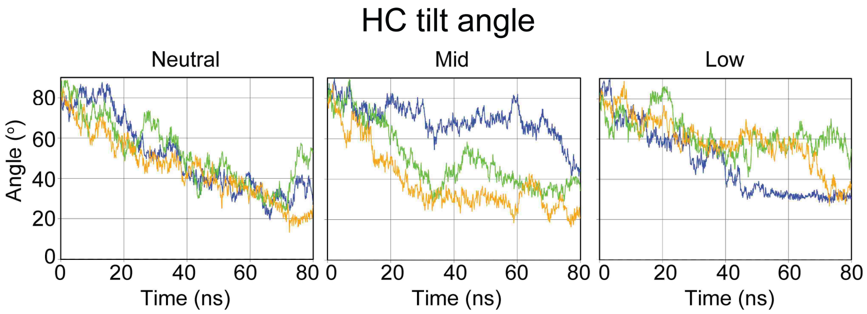

Figure 4.13 HC tilt angle for $\mathrm{PrP}_{\mathrm{mem}}$ simulations

HC tilt angle for $\mathrm{PrP}_{\mathrm{mem}}$ simulation 1 (blue), 2 (green) and 3 (orange) at neutral, mid and low pH.

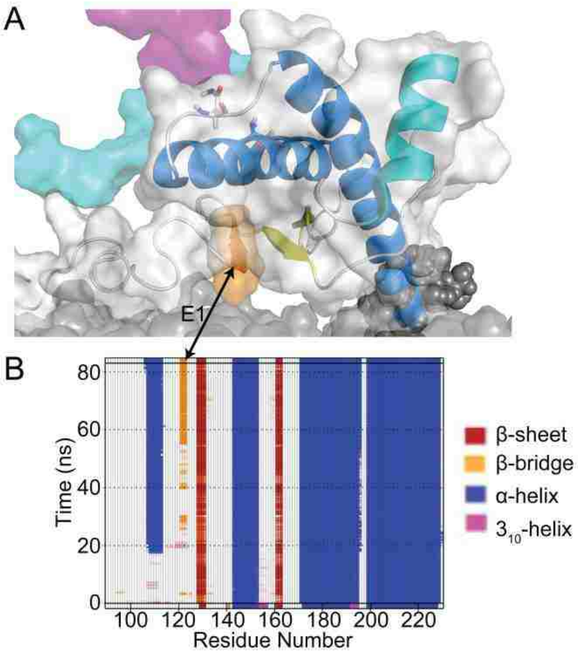

Figure 4.14 Buried E1 epitope in low pH simulation 3

(A) Structure of the membrane-bound PrP in low pH simulation 3 at 80ns. The orange epitope is E1, which is buried on the membrane surface. (B) Secondary structure of the simulation over time.

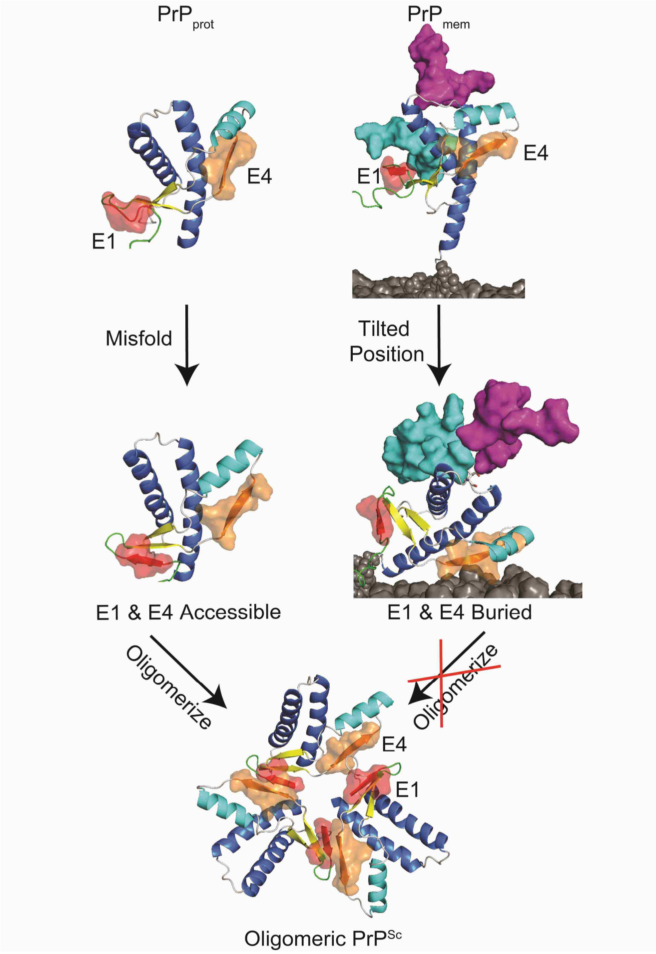

Figure 4.15 Schematic of PrP conversion

Without glycans and the membrane environment, PrP_{prot} misfolds and both E1 and E4 strands are accessible, allowing for oligomerization. As for PrP_{mem}, the oligomerization sites E1 and E4 are buried and on the membrane surface, thus preventing oligomerization.

Chapter 5

COMPARISON OF STRUCTURAL MODELS OF THE PRION OLIGOMER

5.1 Summary

Prion diseases are associated with the misfolding and aggregation of the prion protein (PrP). PrP can exist in two different isoforms: the cellular prion protein (PrP^C), which is innocuous and primarily consists of α-helices, and the scrapie-form PrP^{Sc}, which is infectious and rich in β-sheet structure. PrP^{Sc} is aggregation-prone and forms soluble oligomers that are neurotoxic and infectious. However, the structures of PrP^{Sc} soluble oligomers are often overlooked and most structural characterization efforts focus on PrP^{Sc} fibrils, which like most fibrils are relatively inert and nontoxic. Here we examined the three prevailing models of PrP^{Sc} – the β-helix, spiral and in-register parallel β-sheet model – with a variety of experimental structural data pertinent to PrP^{Sc} soluble oligomers, including hydrodynamic radii, epitope mapping data, engineered disulfide bond constraints, solution NMR data, residue exposure measured by tyrosine-nitration, and secondary structure content. The spiral model is consistent with the bulk of the experimental data, but the β-helix and the β-sheet models do not satisfy several critical constraints. In particular, the β-helix model lacks the flexible N-terminus indicated in NMR studies and several antibody epitopes, and the β-sheet model does not preserve any native helices, putting it at odds with antibody mapping, circular dichroism (CD) and Fourier transformed infrared (FTIR) spectroscopy studies. This study lays the groundwork for future determination and validation of atomistic models of PrP^{Sc} oligomers. As more structural

information is acquired, further development of atomistic models is essential to improve our understanding of prion diseases and assist rational therapeutic development.

5.2 Introduction

Transmissible spongiform encephalopathies, or prion diseases, are associated with the misfolding and aggregation of the prion protein (PrP). PrP is expressed ubiquitously in mammalian cells and can exist in two different forms: the cellular prion protein (PrP^{C}), and the disease-associated, aggregation-prone PrP^{Sc}. Conversion from PrP^{C} to PrP^{Sc} involves misfolding of the PrP^{C} in the low-pH environment of endosomes (71, 148, 149). PrP^{Sc} can aggregate and form soluble oligomers, which can further aggregate and develop into insoluble deposits and amyloid fibrils. There is increasing evidence that soluble oligomeric intermediates, but not fibrils, are responsible for the infectivity and neurotoxicity in prion diseases (198–200). The most infectious oligomer has 14-28 subunits, while the smallest infectious oligomer is a hexamer (200). While the structure of the C-terminal globular domain of the PrP^{C} has been solved by NMR and X-ray crystallographic methods, no experimentally determined high-resolution structure of soluble oligomers of PrP^{Sc} are available.

PrP^{C} has a flexible N-terminal region and a structured C-terminal globular domain with three helices HA, HB and HC, and two short native strands S1 and S2 (Figure 1.1A). Using low-resolution structural information, researchers have proposed various atomistic models for the structure of PrP^{Sc} (201). The three prevailing models are the β-helix, spiral and in-register parallel β-sheet model (referred to as the β-sheet model) (Figure 1.1 and Figure 5.2).

The β-helix model consists of threefold symmetric trimers stacked along the fibril axis (Figure 1.1B) (41, 42). The core consists of β-helices, while the exterior consists of the native helices HB and HC. The β-helix portion was modeled by threading the PrP N-terminal residues to the left-handed β-helix conformation of N-acetylglucosamine-1-phosphate uridyltransferase (PDB ID: 1G97). The β-helix model was built to fit the electron microscopy image of the 2D crystals of prion rods purified from prion-infected hamster brain homogenates (42); these prion rods are infectious and have threefold symmetry. Cross-β architecture was present in these prion rods as indicated in X-ray diffraction studies (42, 43).

The spiral model (Figure 1.1C) was also checked against the 2D electron microscopy images of prion rods by Govaerts et al. (42). In addition to validation by various experimental data (51, 54), the subunits of the spiral model were derived from low pH molecular dynamics (MD) simulations, thus providing a plausible model in which the misfolding pathway is captured in simulations. Other structural differences between the β-helix and spiral models are the axis of symmetry and the preservation of the native helix HA. The spiral model has a space group of $P3_1$, i.e. threefold rotation around the screw-axis (51). All three native helices are preserved, but two nonnative strands, E1 and E4, consistently formed in simulation. These two non-native strands form the binding interface between neighboring monomers.

The β-sheet model (Figure 1.1D), is based on various experimental data for recombinant PrP^{Sc} fibrils, including structural constraints inferred from electron paramagnetic resonance (EPR) (202, 203) and hydrogen/deuterium exchange (40, 204). This model drastically differs from the other two models: the subunits of the model lack native helices and consist of mostly β-strands allowing for the formation of in-register parallel β-sheets along the fibril axis. Residues

159-219 form the β-sheet rich core of the fibril, whereas the remaining portions of the N-and C-terminal residues are unstructured.

Previous efforts to review models focus on structural information on $\mathrm{PrP^{Sc}}$ fibrils, but not on PrP soluble oligomers (201, 205) and they typically ignore the important distinction between the models – they represent different states. As such, one does not necessarily expect an oligomer model, such as the spiral model, to be consistent with data from fibrils, nor will fibrils models such as the β-sheet model necessarily accurately represent oligomeric states preceding mature fibril formation. In this study, we compiled a list of experimental data pertinent to the structure of soluble oligomers of $\mathrm{PrP^{Sc}}$. Using this set of experimental data, we compared the three prevailing atomistic models of $\mathrm{PrP^{Sc}}$ to experiment and evaluated them for consistency. Our work addresses the critical gap in our understanding of the structure of $\mathrm{PrP^{Sc}}$ oligomers and lays the foundation for future work in modeling and validating models for $\mathrm{PrP^{Sc}}$ soluble oligomers.

5.3 *Materials and Methods*

Residue sequence numbers reported are relative to the Syrian hamster sequence. All models were constructed using hamster PrP residues.

5.3.1 *PrP^{Sc}models*

Since the smallest infectious prion unit is a hexamer (200), we have constructed hexamer models for the β-helix, spiral and the β-sheet model. Atomic coordinates of the trimeric unit of the β-helix model were provided by Govaerts et al. (41). Residues were mutated to match that of hamster sequence. A hexameric β-helix model was generated by stacking two trimeric units with one being translated by 20 Å along the fibril axis. The hexameric hamster PrP spiral model from our previous study was extended: flexible regions of N- and C-terminal residues 90-108 and 220-231 were added using Modeller (206) along with manual adjustments to avoid severe steric clashes. Next, *in lucem* molecular mechanics (*il*mm) (129) was used to further minimize steric clashes. The hamster PrP β-sheet model was constructed manually to match the model proposed by Cobb et al. (202). Only the core residues 159-219 were modeled since the remaining residues are unstructured in this model. A hexameric β-sheet model was generated by stacking monomeric units along the fibril axis with a separation of 5 Å between adjacent monomers.

5.3.2 *Hydrodynamic radii*

To compare with the experimentally determined hydrodynamic radii of decamers by Gerber et al. (60), all models were extended from hexamers to decamers. Using the atomic coordinates as the input to WinHydroPro (207), hydrodynamic radii for structured regions of the models were calculated. Using a previously developed method (60), we estimated the contribution to the overall hydrodynamic radius by unstructured regions of a $\mathrm{PrP^{Sc}}$ model. Briefly, we used an empirical equation that describes the relationship between hydrodynamic radius and the number of unstructured residues in a protein (208) and Flory's scaling law (209) to estimate the hydrodynamic radii contribution by the unstructured residues in a decameric unit. The β-helix model does not have any unstructured residues. However, both the spiral and β-sheet models have unstructured residues: residues 90-108 for the spiral model, and residues 90-158 and 220-231 for the β-sheet model.

5.3.3 *Solvent accessible surface area*

Solvent accessible surface area (SASA) was calculated by *il*mm using the Lee and Richards method (133) to compare to the experimental data on the exposure of tyrosine residues in PrP (37). The native SASA of the tyrosine residues was calculated by averaging the SASA measured in the NMR ensemble in PDB ID 1B10 (29). The SASAs for relevant tyrosine residues in the three PrP^{Sc} models were calculated by averaging the SASA across all subunits in each hexameric model.

5.4 Results and Discussion

5.4.1 *PrP^{Sc} Oligomer Dimensions*

Hydrodynamic radii of recombinant PrP^{Sc} oligomers were measured by light scattering and NMR methods, and such radii for PrP^{Sc} decamers are in the range of 56 – 66 Å (Table 3.1) (60, 210–212). The infectivity of these recombinant PrP^{Sc} oligomers is confirmed by experiments (213, 214), suggesting that these oligomers are biologically relevant to the disease process. We calculated the hydrodynamic radii for each model (Table 5.2). The hydrodynamic radius of the spiral model (57.3 Å) gave the best estimate of the hydrodynamic radius measured by NMR (57.4 ± 3.4 Å) (60). On the other hand, the hydrodynamic radius estimated of the β-sheet model was 20 Å over the experimentally determined value. This overestimation was attributed to the unstructured residues 90-158 and 220-231, which contributed another 46 Å on top of the hydrodynamic radius of the core residues 159-219 (39.3 Å). As for the β-helix model, all residues from 90-231 are highly-compact and structured, and therefore the experimental hydrodynamic radius of the β-helix model was underestimated by 9 Å.

5.4.2 *Antibody Epitope Mapping*

A number of strategies were used to map epitopes in the PrP^{Sc} soluble oligomer. These results are summarized together in Table 5.3 and discussed in turn below.

Epitope Mapping on PrP^{Sc} Oligomers

Antibodies with known PrP^{Sc} oligomer binding epitopes can be used to assess the accessible regions on the PrP^{Sc} models, so we hypothesized that a reasonable PrP^{Sc} oligomer model should have such detectable epitopes exposed. PRIOC2 and PRIOC3 (215) bind specifically to oligomers, but not to monomeric PrP^{C} and PrP^{Sc} amyloid fibrils. The epitopes for PRIOC2 and PRIOC3 are PrP residues 90-109 and 170-189, respectively. Similarly, a modified ELISA assay, using the antibody SAF-84 (epitope: residue 160-170) recognizes recombinant sheep PrP oligomers (216). The antibody V5B2 recognizes oligomers of peptides consisting of PrP residues 214-226 (217). Kosmač et al. later discovered that V5B2 binds to C-terminal truncated forms (truncated at residue 226) of both recombinant PrP^{C} and brain-derived PrP^{Sc} (218), suggesting that both truncated forms of PrP^{C} and PrP^{Sc} share the same exposed epitope at residues 214-226.

The spiral model is in overall good agreement with this set of antibodies that recognize the PrP^{Sc} oligomers , because the detectable epitopes are located at the N-terminus, X-loop, helices HB and HC, all of which are solvent exposed and thus accessible to this set of antibodies (Figure 5.3). The β-helix model also shares similar exposure for its X-loop, helices HB and HC, except for residues 90-109, which form the major the binding interface between the trimeric units of the β-helix. However, since the N-terminal end of the β-helix lacks a binding partner, residues 90-109 are thus exposed and may serve as a binding epitope for the PRIOC2 antibody.

The β-sheet model is extended and exposed, and thus is consistent with this set of antibody mapping data.

PrP^{Sc} Inhibitory Antibodies

Smioneau et al. discovered that the antibody Pri303, which binds to the N-terminal residues 106-126, inhibits PrP^{Sc} formation (199). Another PrP^{Sc} inhibitory antibody, 95-R1, also binds to the N-terminal region (residues 95-123) and inhibits PrP^{Sc} conversion (219). Other than the N-terminal region, the helix HA and its preceding loop are also common targets for antibodies that clear PrP^{Sc} accumulation. Such antibodies include 6H4, D18, ICSM18, and ICSM19 (220–222) (Figure 5.4). These PrP^{Sc} inhibitory antibodies suggest that the N-terminus and the helix HA play important roles in the process of oligomerization of the PrP. This is reflected in both the spiral and β-helix models, in which residues of both the N-terminus and helix HA form intermolecular interactions with neighboring monomers. However, in the β-sheet model suggests that residues of helices HB and HC are primarily responsible for the intermolecular interactions between monomers. Therefore, these PrP^{Sc} inhibitory antibodies do not support the β-sheet model.

Motif-grafted Antibodies

Inspired by the inhibitory antibodies, motif-grafted antibodies were generated to study the molecular interactions of the N-terminus and the helix HA region of PrP: mouse PrP residues 89-112 and 136-158 were grafted to the HCDR3 region of a human recombinant antibody to generate the PrP^{Sc}-specific antibodies IgG(89-112) and IgG(136-158) (223). Both antibodies bind to both recombinant β-oligomers and fibrils (224) and precipitate PrP^{Sc} from brain-homogenates of scrapie-infected mice (223, 225). Determined by alanine-scanning, critical grafted PrP residues for PrP^{Sc} recognition are 136-140 and 149-158 in IgG(136-158) and 98-105 in IgG(89-112) (225) (Figure 5.5). Although the binding epitopes of the PrP^{Sc}-specific antibodies IgG(89-112) and IgG(136-158) are still unknown, these two antibodies suggest that the motif-grafted residues are potentially important for PrP^{Sc} binding and oligomerization.

In the spiral model, residues 136-140 are part of the nonnative E4 strand, which forms an intermolecular strand with the nonnative N-terminal strand E1 (residues 116-119). The critical residues 149-158, part of the HA helix, are also in the vicinity of strands E1 and E4 (Figure 5.5). Therefore the oligomerization interface of the spiral model is in good agreement with the putative oligomerization interface indicated by these two motif-grafted antibodies. Furthermore, the conformations of these segments in the oligomer model are different from that in PrP^{C}. For the β-helix model, the grafted residues 89-112 and 136-158 forms the intermolecular binding interface between the trimeric units of the β-helix model, consistent with the predicted oligomerization interface. According to the β-sheet model, residues outside of the core (residues 159-219) are unlikely to play an important role in oligomerization, and therefore it is inconsistent with the motif-grafted antibody results.

Discontinuous Epitopes

While antibody 15B3 was previously thought to detect only infectious PrP^{Sc}, Biasini et al. discovered that the antibody also recognizes various forms of misfolded PrP aggregates including noninfectious neurotoxic PrP aggregates from brain-homogenates (226–228). Nonetheless, this antibody is important for differentiating oligomers from soluble monomeric PrP^{C} and therefore, the discontinuous epitope (residues 142-148, 162-170, and 214-226) of 15B3 is still an important feature to consider when designing PrP^{Sc} oligomer models. The β-helix is not consistent with the discontinuous epitope (Figure 5.6), because residues 142-148 are buried in the core of the structure, making such residues inaccessible to the antibody 15B3. The discontinuous epitope in the spiral model, however, forms a continuous surface that allows for the recognition by the 15B3 antibody (Figure 5.6B). As for the β-sheet model, it intentionally lacks the residues 142-148 (Figure 5.6C).

Antibody DRM1-31 on the other hand recognizes both PrP^{C} and PrP^{Sc}. Peptide scanning indicated three PrP regions to which DRM1-31 binds (229): residues 159-165, 174-180, and 211-218. Therefore, it is possible that the antibody DRM1-31 binds to a discontinuous epitope involving such residues. In the spiral model, the discontinuous epitope forms a continuous surface and maintains a native like conformation (Figure 5.7), consistent with the fact that DRM1-31 recognizes both PrP^{C} and PrP^{Sc}. However, neither β-helix nor the β-sheet model preserves the native conformation of the discontinuous epitope. Thus, antibody DRM1-31 does not support those two models.

Preserved Native Helices

The following antibodies bind to both PrP^{C} and PrP^{Sc} fibrils: 6H4 (230), ICSM4 (231), 94B4 (232), and 4G11 (233) at residues 144-152, 171-190, 187-194, and 199-216, respectively (Figure 5.8). Such antibodies that recognize native helices in both PrP^{C} and PrP^{Sc} fibrils suggest that the helices are preserved in oligomeric intermediates that are precursors of PrP^{Sc} fibrils. Since the β-helix model does not preserve the HA helix and the β-sheet model does not have any helical content, this set of antibodies does not support either model. On the contrary, the spiral model, which preserves the bulk of the native helices HA, HB, and HC, is consistent with this set of antibodies.

5.4.3 *Engineered Disulfide Bonds*

The rates of fibrillation of various PrP with engineered disulfide bonds were measured (106, 107) to identify regions in which dissociation or significant conformation changes are necessary for fibrillation to occur (Figure 5.9). Combining results from Hafner-Bratkovič et al. and Eghiaian et al. (Table 5.4), we have compiled a list of engineered disulfide bonds that stop or slow conversion, or have no effect on conversion.

Four of the engineered disulfide bonds that stop conversion tether the S1-HA-S2 domain to the HC helix, suggesting that conversion requires the S1-HA-S2 domain to detach from HC. Four other engineered disulfide bonds that tether residues within the S1-HA-S2 or the HB-HC domain slow the rate of fibrillation. One of the engineered disulfide bonds that tethers residue 140 and 145, which are in the loop region at the N-terminus of the HA helix, had no effect on the rate of fibrillation.

In order to assess the three models, Cα-Cα distances within monomeric subunits of each PrP^{Sc} model were measured for pairs of residues involved in engineered disulfide bonds. We hypothesize that disulfide bonding a pair of residues with a long Cα-Cα distance stops conversion. Therefore, we expect that all residue pairs in which the engineered disulfide bonds stop conversion have longer Cα-Cα distances than that of residue pairs in which the engineered disulfide bonds either slow conversion or have no effect.

For the spiral model, all Cα-Cα distances of the residue pairs, in which the engineered disulfide bonds stop conversion, are greater than 10 Å. The other Cα distances of the remaining residue pairs, in which the engineered disulfide either slow fibrillation or had no effect, are all less than or equal to 10 Å. Therefore, this set of engineered disulfide bond data support the spiral model. The β-helix model, however, does not show a clear trend of Cα-Cα distances that discriminates the engineered disulfide bonds that stop conversion from the others. The β-sheet model lacks most of the pertinent residues preventing a proper assessment.

5.4.4 *Solution NMR Studies*

NMR Data on Soluble Oligomers

By comparing the $^1H^{15}N$ HSQC spectra of the native and soluble oligomers of PrP, Gerber et al. identified flexible residues in oligomers (60, 140). The oligomers detected are ~200 kDa (decamers). Therefore, residues in the rigid core of oligomers have slow rotational reorientation, resulting in severe peak broadening and failure to detect a large number of resonances for residues 127-227 in the HSQC spectra. The only detectable resonances for the oligomer are within the narrow random coil region between 7.8 and 9.0 ppm and share significant overlap with the 30 resonances for the residues in the unstructured N- and C-terminal regions (residues 92-126 and 226-230) of the native PrP^C. The presence of these visible resonances suggests that the N- and C- terminal residues are also unstructured in the oligomer.

The β-helix model is not consistent with the NMR result, because all residues 90-228 are structured, thus lacking a significant portion of the flexible N-terminus. While the β-sheet has both flexible N- and C- termini, the model has a smaller core (residues 159-219) than the core identified by Gerber et al. (residues 127-227). As for the spiral model, it includes a flexible N-terminal region including residues 90-114 and 120-128 and a flexible C-terminus including residues 221-231. The spiral model also has structured core residues 129-220, consistent with the core predicted by Gerber et al. Overall, the spiral model is more consistent with the flexible/rigid regions identified by this NMR data than are the β-sheet and the β-helix models.

Solution NMR data on fibrillation

Kumar et al. monitored changes to the $^{1}H^{15}N$ HSQC spectra as soluble recombinant PrP converted into fibrils (234). While such information does not directly provide structural information on oligomers, it does provide insight on conformational changes to the PrP during conversion. The overall fast decrease in NMR peak intensities over time for residues 145-223 suggests that most of those residues are part of the rigid core of fibrils. However, a slow decrease in NMR signal was observed for residues 149-151, suggesting that such residues are more mobile and probably more solvent-exposed than the other rigid core residues. Interestingly, residues 149-151 form the YYR epitope detected by a PrP^{Sc}-specific antibody (153), and therefore residues 149-151 are likely surface epitopes accessible to the such antibody. Residues 149-151 are solvent exposed in both the spiral and β-sheet models, but such residues are buried in the core of the β-helix model.

The C-terminal residues 224-230 not only had a slow decrease in NMR signal, indicating flexibility and possibly solvent exposure, but also had changes in chemical shifts, suggesting structural rearrangement of the C-terminus upon fibrillation. C-terminal conformational change is expected since PrP^{C} is attached to the bulky GPI anchor. Exposing the C-terminus upon aggregation therefore minimizes steric clashes by the bulky GPI anchor as aggregation proceeds. While all three models can accommodate the GPI anchor, both the spiral and β-sheet models have flexible C-termini undergoing conformational changes, but the β-helix model preserves the native conformation of the C-terminus.

Residues 90-138 in the N-terminal region show a slow decrease in NMR peak intensity due to the inherent flexibility of the N-terminus in PrP aggregates/fibrils, but there were a few exceptions: more than half of the residues 99-110 displayed a fast decrease in NMR peak intensities similar to that of the rigid core residues, indicating that some N-terminal residues became less mobile upon fibrillation. As fibrillation progresses, these less mobile N-terminal residues might be involved in the aggregation interface and therefore became structured, consistent with the previous motif-grafted PrP^{Sc}-specific antibody IgG(89-112), in which critical PrP residues 98-105 were necessary for PrP^{Sc}-specific binding. However, according to Gerber et al., residues 90-126 at the N-terminus are flexible in oligomers. The reason for the discrepancies between the results of Gerber et al. and Kumar et al. is not clear, but the involvement of residues 99-110 in fibrillation may have to do with the later stage of fibrillation, in which oligomers aggregate and form mature fibrils.

5.4.5 *Exposure of PrP^{Sc} Residues*

Chemical modification is a common method in probing surface-exposed residues in PrP^{Sc} (37, 38, 235). Lennon et al. used tyrosine-nitration to probe for exposed residues in recombinant β-oligomers. In order to compare the experimental findings to the three models, solvent accessible surface areas (SASAs) of the relevant tyrosine residues were measured for the three PrP^{Sc} models and for the NMR structure of hamster PrP^{C} (PDB: 1B10) (Figure 5.10, Table 5.5). We expect that the difference between PrP^{C} and PrP^{Sc} models in side chain SASA correlates with the difference between PrP^{C} and PrP^{Sc} in the intensity of nitration of the respective tyrosine residues. Note that the resolution of the experimental data is limited by the peptide fragments produced by protease digestion. Therefore, the nitration intensity of a peptide fragment in some cases reflects the collective intensity of nitration of multiple tyrosine residues within the peptide fragment.

Table 5.5 compares the PrP^{Sc} models to the experimental data. The sidechain SASA values of the tyrosine residues in the spiral model are consistent with experiment. For the β-helix model, residues 225 and 226 are exposed as they are part of the C-terminus of the helix HC. Therefore, the exposure of these residues in the β-helix model is inconsistent with experiment. The β-sheet model had significant portions of the N- and C- terminus missing, but the β-sheet model agrees with experiment for Tyr169 and Tyr218.

5.4.6 *Helices in Oligomers*

CD and FTIR measurement of secondary structure in oligomers

Circular dichroism (59–61) and FTIR spectroscopy (62) have been used to estimate the secondary structural content of oligomers. Consistent with the previous antibody mapping data, helical residues were detected. Vendrely et al. estimated 14% helix and 18% β-sheet in oligomers (consists of mouse PrP23-231), corresponding to 30 helical residues and 38 β-sheet residues per monomeric subunit. Depending on the deconvolution algorithm, circular dichroism data predict 3-16% of helical residues in oligomers, corresponding to 6 - 33 helical residues in each monomer subunit (59). Despite large errors in deconvolution, Gerber et al. (60) and Bjorndahl et al. (61) estimated 28-32% helix, i.e. 40-46 helical residues per monomeric subunit, in oligomers. Table 5.6 shows the secondary structure comparison among the experimental data and oligomer models. Overall, the spiral model slightly overestimates the helical content and underestimates the β-sheet content (Table 5.6). The β-helix model is roughly in agreement with the experimental data, whereas the β-sheet model lacks helices and therefore is not supported by these experimental results.

Crystal structure of a putative PrP^{Sc} monomer

A crystal structure of a human PrP bound to an inhibitory nanobody contains a putative misfolded structure with a nonnative β-strand at the N-terminus of the human PrP (53). This crystal structure highly resembles our MD-derived misfolded PrP structures (50–52) that we used to construct the spiral model. Both the crystal structure of the misfolded human PrP and our MD-derived misfolded hamster PrP structure have the three native helices intact and a nonnative strand formed at the flexible N-terminus. This crystal structure supports our predictions of the misfolded PrP structure as the building block for nascent PrP^{Sc} oligomers, and such oligomers consists of misfolded PrP with most native secondary structures (such as helices) preserved.

5.5 Conclusions

While major effort has been spent on building PrP^{Sc} models using structural data pertinent to fibrils (202, 236), the oligomer-related structural evidence is often overlooked. Here, we evaluated the consistency of the three prevailing PrP^{Sc} models with a focus on using experimental structural evidence for soluble oligomers instead of PrP^{Sc} fibrils. We have compared the three models to a variety of experimental data, such as hydrodynamic radii, epitope mapping data, engineered disulfide bond constraints, flexibility measured by NMR, residue exposure measured by tyrosine-nitration, and experimentally determined helix content in soluble oligomers. The spiral model is in good agreement with the majority of the data, while the β-helix and β-sheet models are in disagreement with some critical experimental data. In particular, the β-helix model lacks a flexible N-terminus indicated in NMR studies, and the β-sheet model does not preserve any native helices, putting it in disagreement with antibody mapping, CD and FTIR studies. For a summary of comparisons, see Table 5.7.

As our knowledge of soluble oligomers expands, so will our list of experimental structural information with which we can use to build and validate our $\mathrm{PrP^{Sc}}$ models. Here we establish the foundation for future efforts in modeling and validating the structure of $\mathrm{PrP^{Sc}}$ oligomers that are essential to our understanding of prion diseases. While experimental evidence suggests that the spiral model is a plausible model for nascent $\mathrm{PrP^{Sc}}$ oligomers, we do not exclude the possibility of other atomistic models that are also supported by experiments. Given the heterogeneity of soluble oligomers and prion strain diversity, future work is required to expand atomistic models such that they capture the diverse conformations of $\mathrm{PrP^{Sc}}$ oligomers.

Table 5.1 Comparison of hydrodynamic radii measured for oligomers of PrP^{Sc}

	#subunits	hydrodynamic radius (Å)	PrP fragment	method of measurement	Reference
Experiments	10	65	hamster 90-231	light scattering	(212)
	9	66	hamster 90-232	light scattering	(210)
	10	56	human 90-231	light scattering	(211)
	8	60	hamster 90-231	light scattering	(237)
	10	57.4	human 90-231	NMR (DOSY)	(60)
Models	10	57.3	hamster 90-231	spiral model	N/A
	10	85.1	hamster 90-231	β-helix model	N/A
	10	48	hamster 90-231	β-sheet model	N/A

Table 5.2 Contribution to the hydrodynamic radii by the structured and unstructured regions in each model

	Models			Experiment
	β-helix	Spiral	β-sheet	Gerber et al., 2007 JBC (60)
structured residues	90-231	109-231	159-219	N/A
structured R_h (Å)	48.0	46.6	39.3	N/A
unstructured residues	N/A	90-108	90-158, 220-231	N/A
unstructured R_h (Å)	N/A	10.7	45.8	N/A
total R_h (Å)	**48.0**	**57.3**	**85.1**	**57.4**

Table 5.3 Summary of antibody mapping data

			Comments for each model			
	Antibodies	**Epitopes**	**β-helix**	**Spiral**	**β-sheet**	**References**
Antibodies that bind to oligomers	PRIOC2	90-109	Epitopes accessible in all models			(215)
	PRIOC3	170-189				(215)
	SAF-84	160-170				(216)
	V5B2	214-226				(217, 218)
Motif-grafted Antibodies: bind to both recombinant oligomers and fibrils	IgG(136-158)	grafted PrP residues 137-159	Epitopes involved in intermolecular binding interfaces		Epitopes not in model	(223–225)
	IgG(89-112)	grafted PrP residues 90-113				(223–225)
PrP^{Sc}-inhibitory Antibodies	Pri303	106-126	Epitopes involved in intermolecular binding interfaces		Epitopes not in model	(199)
	95-R1	95-123				(219)
	6H4, D18, ICSM18, and ICSM19	around the helix HA (res 132-158)				(220–222)
Antibody with discontinuous epitope: recognize only oligomers, not monomers	15B3	residues 142-148, 162-170, and 214-226	Disontinuous epitopes are seperated	Discontinuous epitopes form a continuous surface	One of the epitopes not in model	(228, 230)
Antibody with discontinuous epitope: recognize both PrP^{C} and PrP^{Sc} fibrils	DRM-31	residues 159-165, 174-180, and 211-218	Does not preserve native conformation	Preserved native epitopes	Does not preserve native conformation	(229)
Antibodies that bind to native helices: recognize both PrP^{C} and PrP^{Sc} fibrils	6H4	144-152	Lack the native helix HA	Preserved all native helices	Loss all native structure	(230)
	ICSM4	171-190	Preserved native helices HB and HC			(231)
	94B4	187-194				(232)
	4G11	199-216				(233)

Table 5.4 Cα-Cα distances between residues which engineered disulfide bonds were made

				Cα-Cα Distances (Å)		
References	resA	resB	β-helix	Spiral	β-sheet	Effect
(107)	136	154	24	9	?	slows conversion
(107)	191	196	5	6	16	
(107)	128	162	21	6	?	
(106)	127	164	22	7	?	
(107)	134	217	13	16	?	stops conversion
(107)	137	212	13	15	?	
(107)	161	213	32	13	52	
(106)	157	206	42	15	?	
(107)	140	145	10	10	?	no effect

Red cells indicate Cα-Cα distances that exceed 10 Å for disulfide engineered residue pairs that slow conversion.

Table 5.5 Percentage tyrosine sidechain SASA difference (relative to hamster PrP^{C}) in spiral, β-sheet, and β-helix models

Tyrosine residues	Difference in SASA (PrP^{Sc}-PrP^{C})		
	β-helix	Spiral	β-sheet
225,226	20%	-61%	N/A
149,150	40%	26%	N/A
157,162,163	168%	64%	N/A
169	31%	6%	76%
218	558%	205%	77%

Residues are sorted by PrP^{Sc}-buried (orange) and PrP^{Sc}-exposed (blue), according to experimental data. The red cell indicates discrepancy between the β-helix model and the experimental data.

Table 5.6 Comparison of secondary structures among oligomer models and experimental data

	Method	percentage		# of residues		PrP construct	**References**
		helix	β-sheet	helix	β-sheet		
Experiments	FTIR	14	18	30	38	mouse PrP23-231	(62)
	CD, K2D	3	31	6	65	mouse PrP23-231	(59)
	CD, CDSSTR	16	31	33	65		
	CD	28	N/A	40	N/A	human PrP 90-231	(60)
	CD	32	20	46	29	hamster PrP90-232	(61)
Models	Spiral	33	13	47	19	hamster PrP90-231	
	β-helix	32	28	45	40	hamster PrP90-231	
	β-sheet	0	67	0	41	hamster PrP159-219	

Table 5.7 Summary of comparisons between models and experimental data

	Model in agreement?		
Experiment	β-helix	Spiral	β-sheet
Hydrodynamic Radius			
NMR and light scattering	no	yes	no
Antibody epitope mapping			
Oligomer binding antibodies	yes	yes	yes
Inhibitory antibodies	yes	yes	no
Motif-grafted antibodies	yes	yes	no
Discontinuous epitope	no	yes	no
Native helices	no	yes	no
Engineered disulfide bonds			
Constraints that are conversion inhibitory	no	yes	?
Constraints that have no effect or slow conversion	no	yes	?
NMR data			
Flexible and rigid regions in oligomers	no	yes	no
Flexibility and exposure at the YYR epitope	no	yes	yes
Structured residues in N-term: 99-110	no	yes	no
Conformational changes at C-term: resi 224-230	no	yes	yes
Chemical modification			
Residues exposed in PrP^{Sc}	yes	yes	?
Residues buried in PrP^{Sc}	no	yes	?
Helices in oligomers			
CD and FTIR of oligomers	yes	yes	no
Crystal structure of a misfolded PrP monomer	no	yes	no

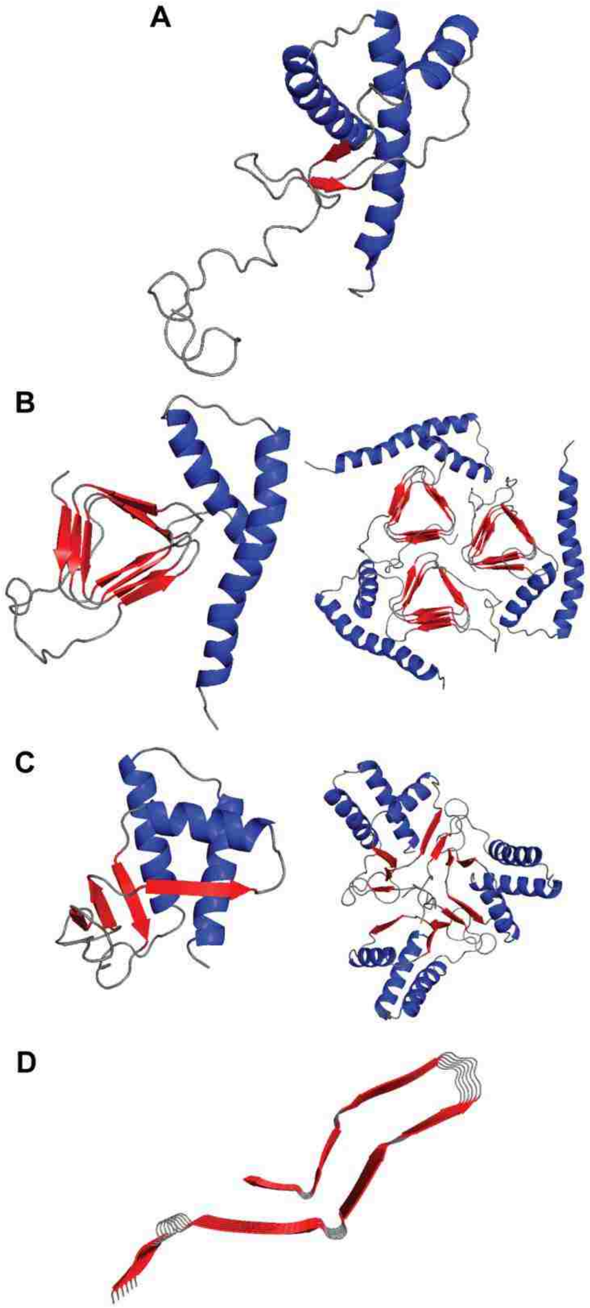

Figure 5.1 The Three models of PrP^{Sc}

Helices and β-strands are shown in blue and red cartoon representations respectively. (A) Residues 90-231 of hamster PrP^{C}. (B) Residues 90-231 of the monomer and trimer of the β-helix model. (C) Residues 109-219 of the monomer and trimer of the spiral model. (D) Residues 159-219 of the hexameric β-sheet model.

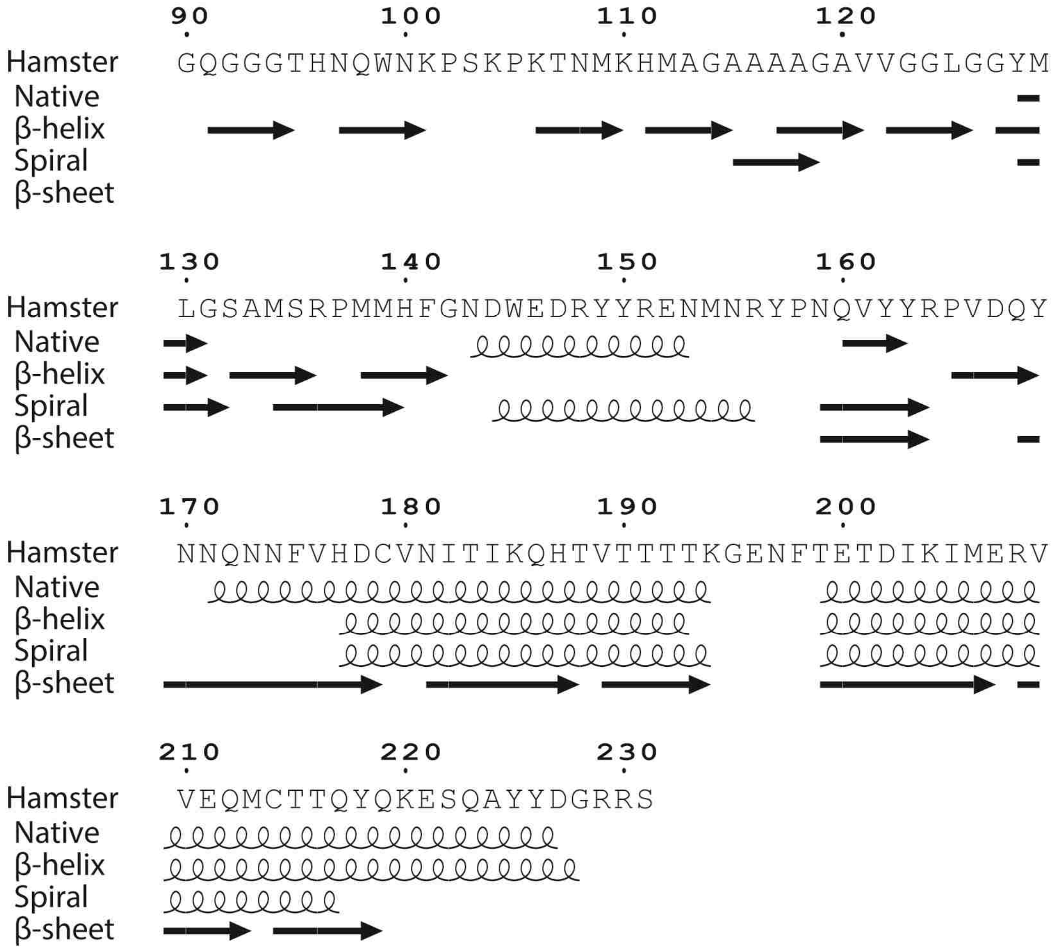

Figure 5.2 Comparison of secondary structures for the native hamster PrP and oligomer models

Secondary structure for the native hamster PrP, β-helix model, spiral model and the β-sheet model.

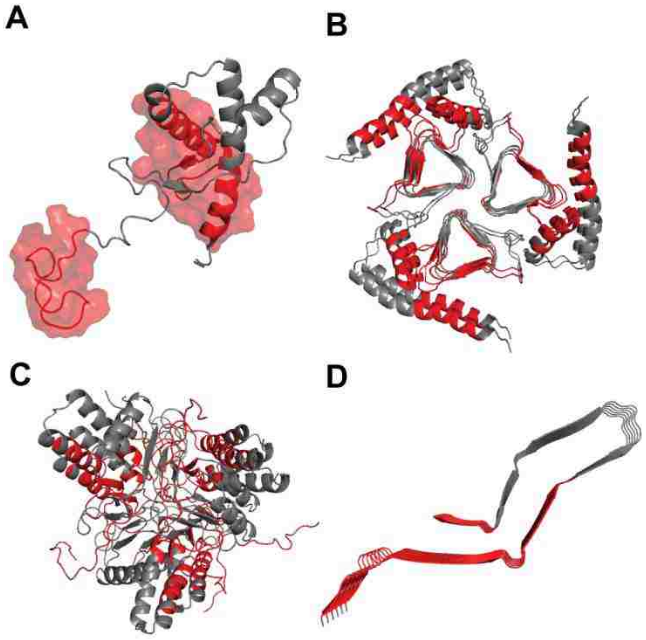

Figure 5.3 Antibodies that recognize oligomers of PrP^{Sc}

(A) Native hamster PrP^{C}, (B) β-helix, (C) Spiral, and (D) β-sheet models of PrP^{Sc} are shown with red epitopes indicating residues 90-109, 170-189, 160-170, and 214-226 recognized by antibodies PRIOC2, PRIOC3, SAF-84 and V5B2 respectively.

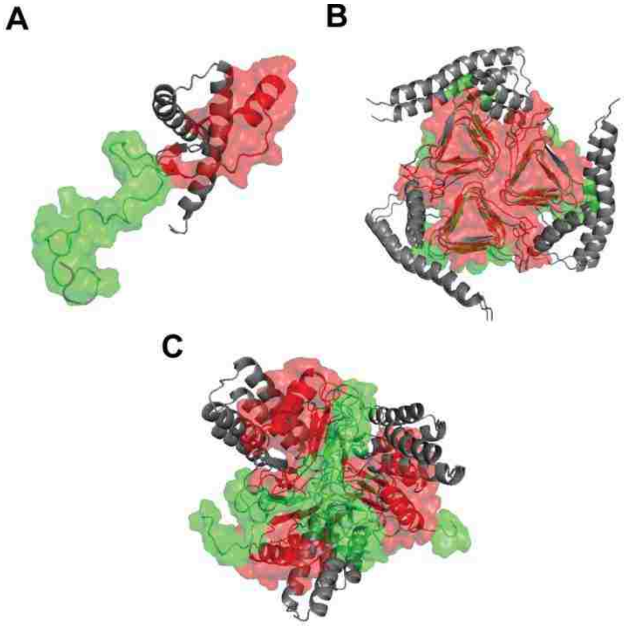

Figure 5.4 PrP^{Sc} inhibitory antibodies

(A) Native hamster PrP^{C} and (B) hexameric β-helix and (C) spiral model of PrP^{Sc} are shown with green epitopes indicating overlapping epitopes: residues 106-126 and 95-123 for antibodies Pri303 and 95-R1 respectively. Red colored regions are residues 132-158, representing the epitope to which PrP^{Sc} inhibitory antibodies 6H4, D18, ICSM18, and ICSM19 bind.

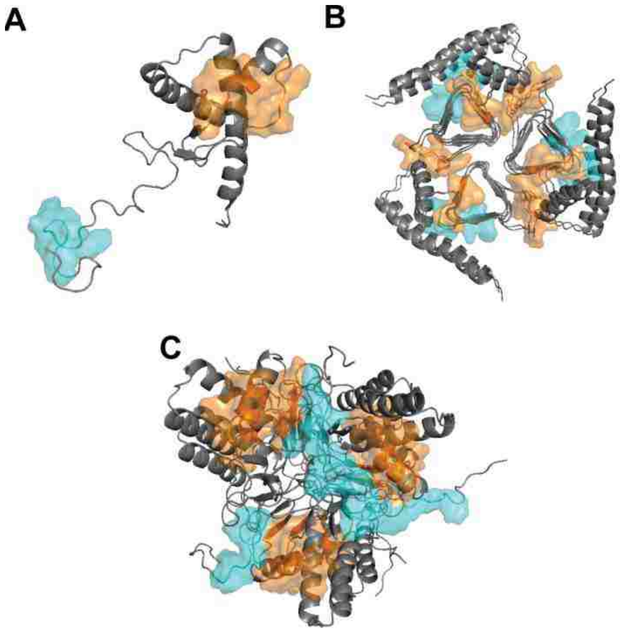

Figure 5.5 Critical residues for PrP^{Sc}-recognition in motif-grafted antibodies

(A) Native hamster PrP^{C} and (B) β-helix and (C) spiral hexameric PrP^{Sc} models are displayed. Cyan residues indicate critical residues 98-105 for IgG(89-112) and orange residues indicate critical residues 136-140 and 149-158 for IgG(136-158).

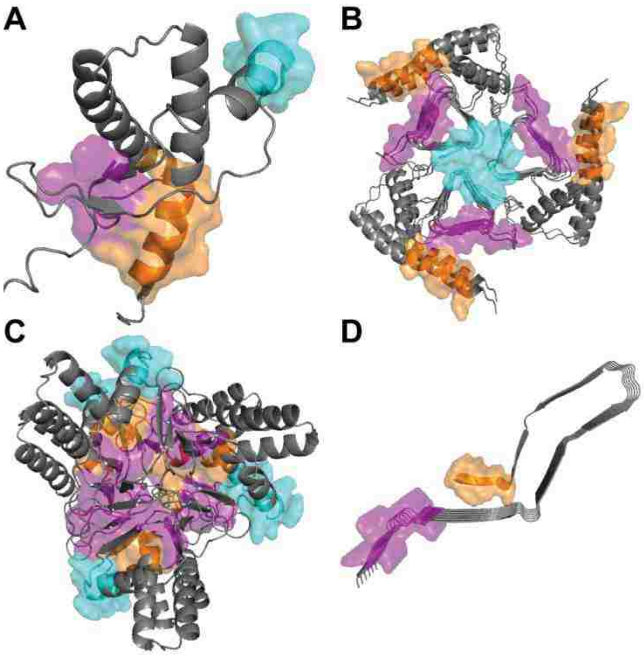

Figure 5.6 Discontinuous epitope of 15B3 antibody

(A) Native hamster PrP^{C}, (B) β-helix, (C) spiral and (D) β-sheet models of PrP^{Sc} are displayed. Cyan (residues 142-148), purple (residues 162-170), and orange (residues 214-226) regions form the discontinuous epitope of the 15B3 antibody. Cartoon representation for residues 90-108 in the spiral model are omitted for clarity purposes.

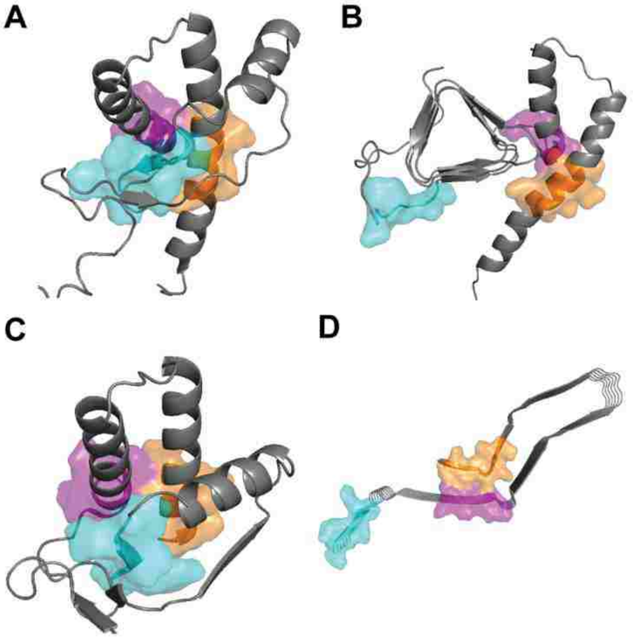

Figure 5.7 Discontinuous epitope of the antibody DRM1-31

Cyan (residues 159-165), purple (residues 174-180), and orange (residues 211-218) regions form the discontinuous epitope of the antibody DRM1-31. (A) Native hamster PrP^{C} NMR structure PDB ID: 1B10 with extended N- and C- terminal residues. (B) Monomeric unit of the hamster PrP^{Sc} β-helix model, residues 90-231 are shown in the figure. (C) Monomeric unit of the hamster PrP^{Sc} spiral model, only residues 109-219 are shown for clarity. (D) Hamster PrP^{Sc} β-sheet model, which has only residues 159-219 modeled.

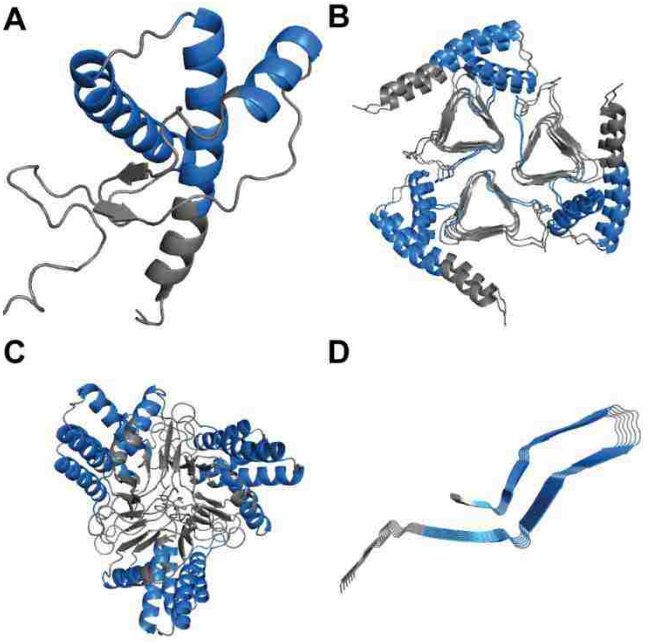

Figure 5.8 Antibody mapping of native helices

(A) Native hamster PrP^{C}, (B) β-helix, (C) spiral and (D) β-sheet models of PrP^{Sc} are shown. Blue regions cover residues 144-152, 171-190, 187-194, and 199-216, which are recognized by antibodies 6H4, ICSM4, 94B4, and 4G11, respectively. Only residues 109-219 are shown for clarity for the hexameric spiral model.

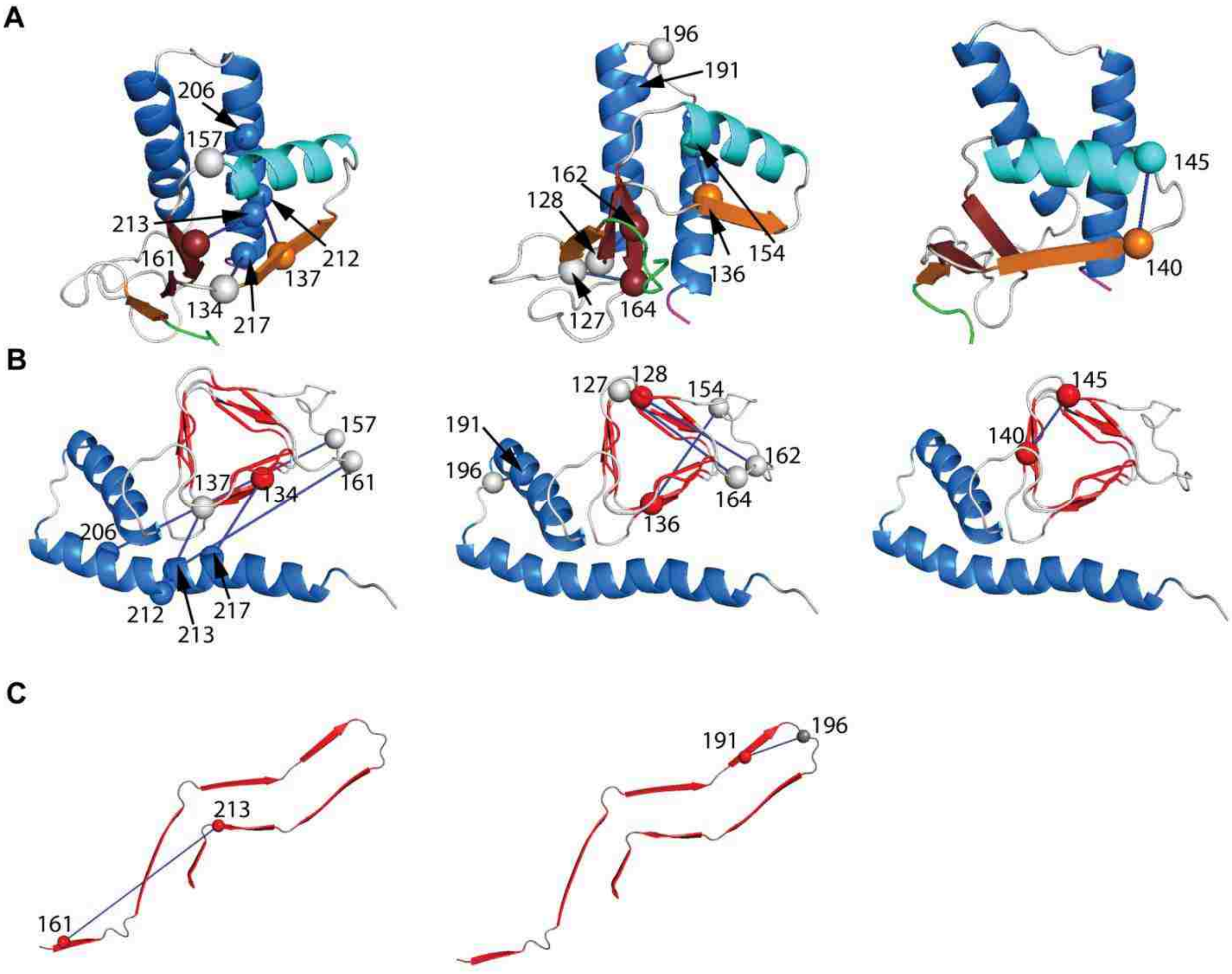

Figure 5.9 Engineered disulfide bonds mapped on PrP^{Sc} models

Engineered disulfide bonds for (A) spiral, (B) β-helix and (C) β-sheet models. Blue lines link pairs of Cα atoms of residues which engineered disulfide bonds were made. Left: disulfide residue pairs which stop conversion. Middle: disulfide residue pairs which slow the rate of fibrillation. Right: disulfide residue pairs which has no effect on the rate of fibrillation.

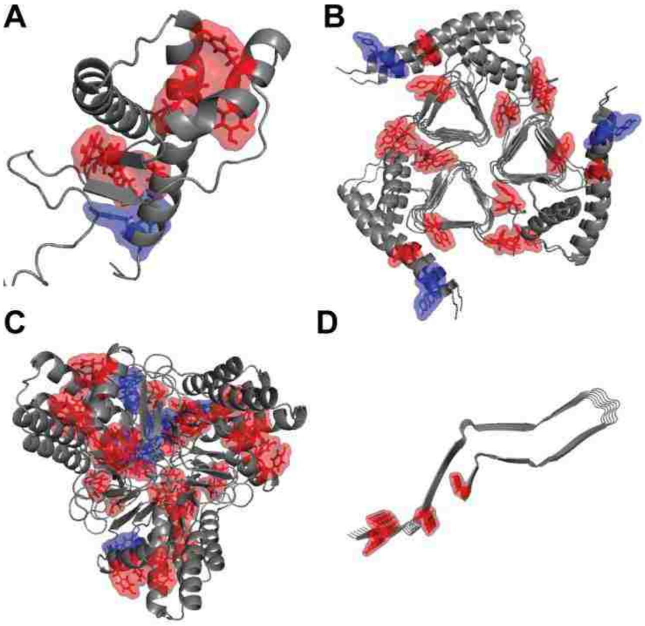

Figure 5.10 Exposure indicated by tyrosine nitration

Exposure indicated by tyrosine nitration shown for (A) native hamster PrP^C, (B) β-helix, (C) spiral, and (D) β-sheet models. PrP^{Sc}-exposed residues 149, 150, 157, 162, 163, 169, and 218 are colored in red and PrP^{Sc}-buried residues 225 and 226 are colored in blue. Only residues 109-219 are shown for clarity of the hexameric spiral model.

Chapter 6

MODEL SYSTEM FOR PRION PROPAGATION

6.1 Summary

After performing simulations on the human membrane-bound PrP^C (Chapter 4), the bovine PrP at low pH (Chapter 3), and validating the spiral model with current experimental data on soluble oligomers (Chapter 5), I have constructed a system to study the PrP^{Sc}-induced structural changes on PrP^C. In this system, the membrane-bound human PrP^C construct was based on the system from Chapter 4, except that the membrane was extended from 335 lipid molecules to 719 lipid molecules. Such extended membrane was large enough to accommodate a hexameric bovine PrP^{Sc} spiral model, which was constructed with the low pH misfolded structure from Chapter 3. The goal of simulating this large and complex system (> 277,000 atoms) is to identify the molecular mechanism of PrP^{Sc}-induced misfolding in a membrane environment. Albeit the limited time scale of our simulations (a triplicate of 22 ns simulations), we have observed conformational changes in PrP^C, and also consistent, significant disruption of the POPC membrane as a result of the bovine hexamer binding to the membrane surface. Our results confirm previous experimental findings on the membrane-binding affinity of the PrP^{Sc} oligomer and provide an explanation to the misfolding mechanism in a membrane environment. This work serves as the steppingstone for future studies on PrP^{Sc}-induced misfolding in a membrane environment.

6.2 *Material and Methods*

6.2.1 *Hexameric bovine spiral model for bovine PrP^{Sc}*

The bovine hexameric spiral model was constructed with the low pH misfolded structure at 32.6 ns of simulation 3 in Chapter 3. The oligomer model was constructed using previously described methods (51, 52). Briefly, the E1 strand of every monomer was docked to its adjacent neighbor's E4 strand, resulting in 120° turn per monomer and 10 Å raise for every monomer added. The intermolecular backbone hydrogen bonds between E1 and E4 strands were then constrained using a flat-bottom well potential energy function and molecular dynamics was performed to allow for equilibration of the oligomer model in water at 310K. Simulation with constraints was performed for 32 ns and then the constraints were released for a final 10 ns of simulation to ensure that the flat-bottom well potential did not result in an unstable oligomer model. The 37.9 ns structure of the oligomer was then used as a docking structure for building the PrP^{C} + PrP^{Sc} system.

6.2.2 *Membrane extension and periodic box for simulation*

In Chapter 4, the POPC lipid bilayer consists of 335 lipid molecules with a periodic box of the following dimension: 94 × 98 × 147 Å. In order to accommodate for the bovine PrP^{Sc} with at least 20 Å buffer from the edges of the periodic box in MD simulation, the 335 lipid bilayer was extended to 719 lipid molecules. Extension was done by repeating the lipid molecules along the x and z axes as a periodic box would. The periodic box dimension for the PrP^{C} + PrP^{Sc} system was x (width) = 121.4 Å, y (height) = 139.2 Å, z (length) = 163.6 Å, where the membrane was extended along the x-z plane.

6.2.3 *MD simulation of the PrP^C + PrP^{Sc} system*

The design of the PrP^C + PrP^{Sc} system was done such that the E4 region of the PrP^C is in contact with the E1 strand of the PrP^{Sc} oligomer and that the PrP^{Sc} is in contact with the membrane surface. It is important to place PrP^{Sc} in contact with the membrane, because previous experiments have shown that exogenous PrP^{Sc} are incapable of converting membrane-bound PrP^C, but by fusing PrP^{Sc} and PrP^C both to the same membrane surface, misfolding and aggregation was observed (187).

The membrane-bound human PrP^C, POPC lipid bilayer, glycans, GPI anchor were derived from the low pH membrane-bound PrP^C simulation in Chapter 4. The E1 strand of the bovine PrP^{Sc} was manually docked to the E4 region of the membrane-bound PrP^C. Multiple docking attempts were made to minimize the steric clashes between bovine PrP^{Sc} and the membrane. Solvation was then performed on the PrP^C + PrP^{Sc} system; 54830 water molecules were added to the system. Water density was set at 0.993 g/cm^3 for simulation at 310K. After solvation, a series of minimizations were performed: 1) 1000 steps of minimization was performed on the entire system; 2) 500 steps of minimization performed on the hydrophobic tail of the GPI anchor; 3) 2500 steps of minimization was performed on water molecules only; 4) 3000 steps of minimization was performed on water molecules and lipid molecules. After these minimization steps, a series of dynamics, followed by energy minimization, were performed. 1) water and lipid dynamics were performed for 5 ps followed by 500 steps of minimization of the entire system; 2) 10 ps of water and lipid dynamics were performed followed by 1000 steps of minimization of the entire system. After performing dynamics on lipid and water molecules, a triplicate of 22 ns MD simulation was performed at 310K.

6.2.4 *Membrane Analyses*

In order to study the membrane properties, the membrane was split into bins such that each bin has on average 4 lipid molecules for both upper and lower leaflets of the membrane. Each bin has the following dimension: x = 13.5 Å and z = 16.4 Å. Given that there are 719 lipid molecules in the system, the membrane was divided into 90 bins with 10 bins along the z-axis and 9 bins along the x-axis (Figure 1.1). Membrane properties were calculated for each bin. Membrane properties include: 1) membrane height, which is the difference between the average y-coordinates of the phosphorus atom of the upper lipid molecules and the y-coordinate of the phosphorus atom of the GPI anchor, 2) membrane thickness, which is the average distance between the phosphorus atoms between upper and lower membrane lipid molecules; 3) lipid separation, which is the minimal y-coordinate difference between atoms of the top and bottom lipid molecules, and 4) membrane contacts with bovine PrP^{Sc} and PrP^{C}.

The void volume of the membrane was calculated for bins that have lipid separation > 4 Å, because such lipid separation indicates loss of contact between the upper and lower lipids, and therefore indicates the presence of a void volume in the bin. Void volume was calculated by multiplying the lipid separation distance by the dimensions of the bin.

In order to obtain a rough baseline for normal membrane dynamics without the disruption caused by the PrP^{Sc}, I used the low pH membrane-bound human PrP^{C} simulations from Chapter 4 as a control for the membrane dynamics and properties. For the control simulations, membrane analysis was done by splitting the membrane into 42 bins, with 6 bins along the z-axis and 7 bins along the x-axis (Figure 1.1). Dimension of the bin is the same as that of the PrP^{C} + PrP^{Sc} system.

6.2.5 *Definition of atomic contacts*

In order to qualify as a contact, a pair of carbon atoms must be less than 5.4 Å apart and for carbon-noncarbon contacts and noncarbon-noncarbon contacts, the two atoms must be less than 4.6 Å apart. Hydrogen atoms were not considered in measuring atomic contacts.

6.3 Results and Discussion

6.3.1 *Monitoring conformational changes in simulations with Cα RMSD*

Cα RMSD was used to monitor structural changes of proteins in simulations. The increasing overall Cα RMSD (Figure 6.2) indicates that protein dynamics have yet to reach equilibrium by the end of simulations. The overall Cα RMSD ranged from ~4 Å - 6 Å by the end of 22 ns of the simulations. Cα RMSD of the human PrP^C and the bovine hexamer were also monitored separately. The Cα RMSD for the bovine hexamer was stable and reached equilibrium at around 3 Å (Figure 6.2). The stability of the bovine hexamer was expected since the starting structure of the oligomer was an MD-derived structure (see methods for details on preparation of the oligomer model). On the other hand, the structured globular domain (residues 128-228) of the human PrP^C was disrupted in simulation 3. Previously in Chapter 4, we have shown that the membrane-bound PrP^C is stable and the average globular domain Cα RMSD was no more than 2 Å. Here we show that in simulations 3, the structured globular domain of human PrP^C underwent noticeable conformational change (Figure 6.4). Cα RMSD by atom indicated regions in which large conformational changes were observed. In simulation 3, high Cα RMSD regions include residues 142-146 (E4 region), 191-197 (Loop between helices HB and HC), and 224-228 (C-terminal of helix HC).

6.3.2 *Contacts between bovine PrP^{Sc} and membrane-bound human PrP^{C}*

In order to further understand conformational changes observed in the membrane-bound PrP^{C}, contact analyses between human PrP^{C} and the bovine PrP^{Sc} were performed (Figure 6.3). At the starting structure, there were 181 atomic contacts between the human PrP^{C} and the bovine PrP^{Sc}. While both simulation 1 and 2 had relatively steady number of contacts, simulation 3 reached >400 contacts within the first 2 ns and the contacts dropped down to 275 contacts by the end of the simulation. Major regions involved in intermolecular interactions of PrP^{C} and PrP^{Sc} were helix HA and E4 in PrP^{C}, and helix HB, strands E1, S1 and S2 in PrP^{Sc}. Direct contacts between PrP^{Sc} and PrP^{C} may explain the regions in which high Cα RMSD were observed. However, I also hypothesize that drastic membrane dynamics may also contribute to the bending of C-terminus of helix HC, given that the C-terminal is linked to the GPI anchor, which is embedded in the membrane (Figure 6.4).

6.3.3 *Membrane disruption induced by PrP^{Sc}*

Low pH membrane-bound human PrP^{C} simulations from Chapter 4 served as a control for the membrane dynamics and properties (Figure 6.5). Membrane height of the control simulations were slightly positive, indicating that lipids tended to be positioned slightly higher than the GPI anchor did. The average membrane thickness of control simulations was 38 Å (Table 3.1). The membrane-bound PrP^{C} formed some contacts on the membrane surface without causing significant disruption on the membrane height or thickness.

On the other hand, the membrane of the PrP^{C} + PrP^{Sc} system was affected by PrP^{Sc}. Membranes of all three simulations of the PrP^{C} + PrP^{Sc} system consistently had decreased membrane height for the region to which PrP^{Sc} bound (Figure 6.6, Figure 6.7, and Figure 6.8). Other than the consistent reduction of membrane height, the thickness of the membrane by the end of the simulations were on average 48 Å (Table 3.1), which is 10 Å greater than that of the control simulations. The thickness of the membrane increased significantly at the lower-right area of the membrane, which is adjacent to the PrP^{Sc}. Membrane thickness by the end of the simulation was >70 Å at the lower right area of the membrane, thus indicating a void volume in the membrane. The void volume of the membrane was further analyzed by measuring the separation of the upper and lower lipid molecules (Table 6.2). By the end of the simulations, lipid molecules were separated by ~12 Å across 8-10 bins, resulting in a pocket roughly ~20000 $Å^3$. Contacts between the PrP^{Sc} and the membrane increased over time. In the beginning, there were a total of 1000 atomic contacts between PrP^{Sc} and the membrane, but by the end of the simulation, the number of atomic contacts increased by ~500 in both simulation 1 and 3, and by > 300 in simulation 2 (Table 3.1). It was interesting to observe that, despite the large increase in membrane contacts, the conformation of PrP^{Sc} was stable by the end of the simulation as indicated by Cα RMSD (Figure 6.2).

The significant disruption of the membrane in all three simulations of the PrP^C + PrP^{Sc} system was in agreement with experimental findings: although PrP^C have weak binding affinity to small unilaminar vesicles, the PrP^{Sc} oligomer binds strongly to such vesicles and depending on the type of lipid molecule, the PrP^{Sc} oligomer may affect the membrane integrity, thus causing pores and leakage of such vesicles (238). PrP^{Sc} is known to bind to planar lipid membranes at a higher affinity than PrP^C do (239). Screening of electrostatic interaction by NaCl has been shown to significantly reduce membrane binding for both PrP^C and PrP^{Sc}, suggesting that salt bridges are crucial to membrane interactions (239). Each PrP^{Sc} monomer carries 19 positively charged residues, allowing significant contacts with the membrane anionic phosphate groups. The interactions of the PrP^{Sc} and the membrane not only affected the membrane integrity, but also caused drastic changes in the membrane height which may contribute to the bending of the helix HC at the C-terminal of the PrP^{C}, especially since the C-terminal of PrP^{C} is tethered to the membrane via a GPI anchor. Such membrane dynamics may facilitate misfolding of the PrP^{C}.

Table 6.1 Average values for control and PrP^{C}+PrP^{Sc} simulations

Simulation		Membrane height (Å)	Membrane thickness (Å)	Number of PrP^{C} contacts	Number of PrP^{Sc} contacts
Control (40-80ns)	1	4.6 ± 2.3	37.6 ± 2.7	29 ± 11	N/A
	2	3.4 ± 2.3	37.6 ± 2.3	29 ± 18	N/A
	3	2.9 ± 2.3	37.7 ± 2.3	37 ± 16	N/A
PrP^{C}+PrP^{Sc} (20-22ns)	1	-2.6 ± 8.7	48.1 ± 8.6	65 ± 12	1481 ± 64
	2	-13.1 ± 8.2	48.2 ± 10	90 ± 12	1357 ± 52
	3	-14.1 ± 10.7	48.1 ± 9.6	115 ± 16	1522 ± 51

Table 6.2 Lipid separation and void volume calculated for last 2 ns of the simulations

Simulation	Number of bins > 4 Å	Average lipid separation (Å)	Void volume ($Å^3$)
1	8	11.7	19923
2	10	11.8	25227
3	8	12.6	21081

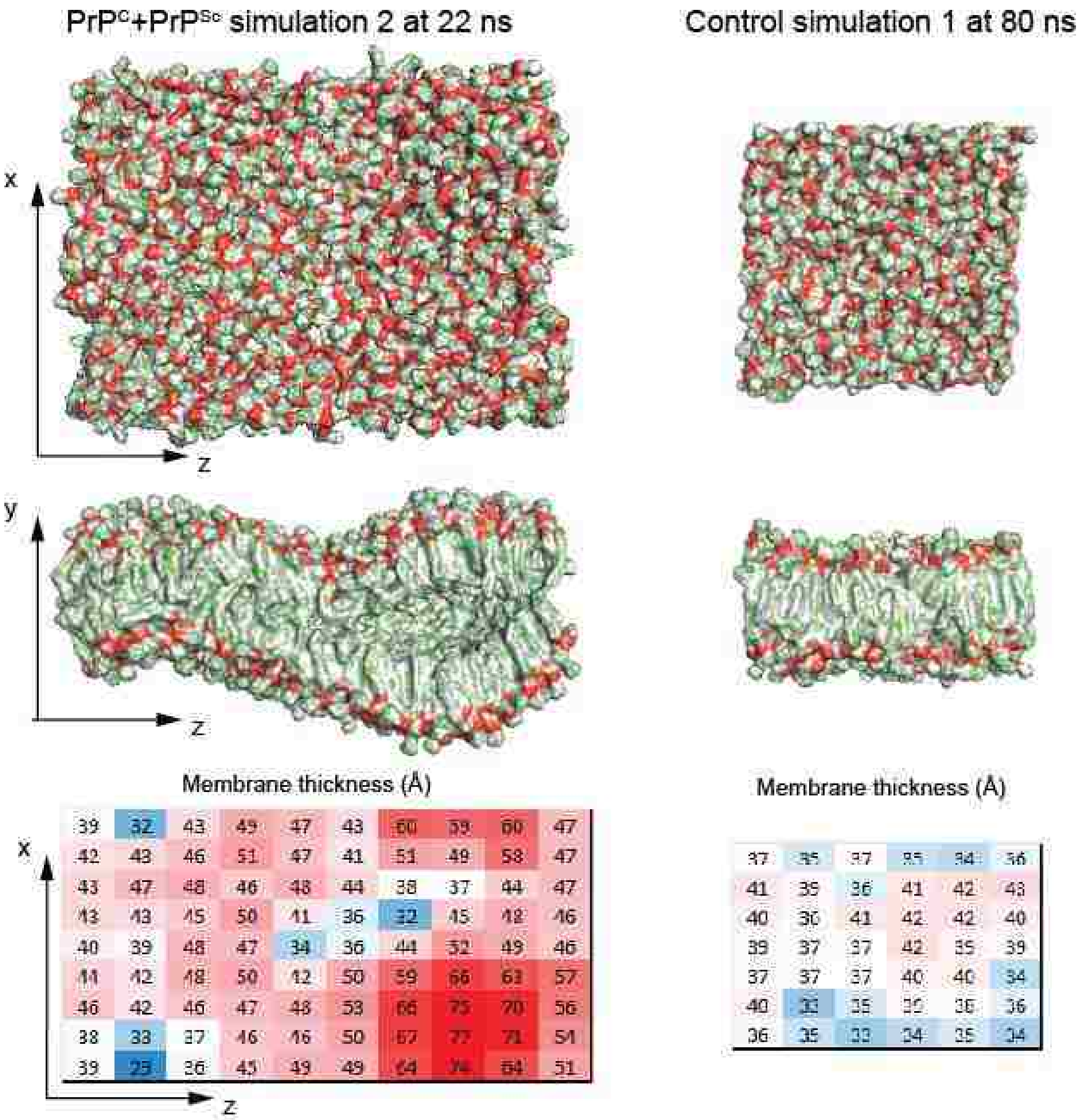

39	32	43	49	47	43	60	59	60	47
42	43	46	51	47	41	51	49	58	47
43	47	48	46	48	44	38	37	44	47
43	43	45	50	41	36	32	45	42	46
40	39	48	47	34	36	44	52	49	46
44	42	48	50	42	50	59	66	63	57
46	42	46	47	48	53	66	75	70	56
38	33	37	46	46	50	67	77	71	54
39	25	36	45	49	49	64	74	64	51

37	35	37	35	34	36
41	39	36	41	42	43
40	36	41	42	42	40
39	37	37	42	35	39
37	37	37	40	40	34
40	33	35	39	38	36
36	35	33	34	35	34

Figure 6.1 Binning and calculation of membrane properties

Left: PrP^C + PrP^{Sc} simulation. Right: Control simulation (membrane-bound human PrP^C simulation from Chapter 4) Top and side view of the membranes are shown (proteins and glycans excluded). The tables at the bottom serve as an example to show how membrane properties (in this case being membrane thickness) were calculated for each bin.

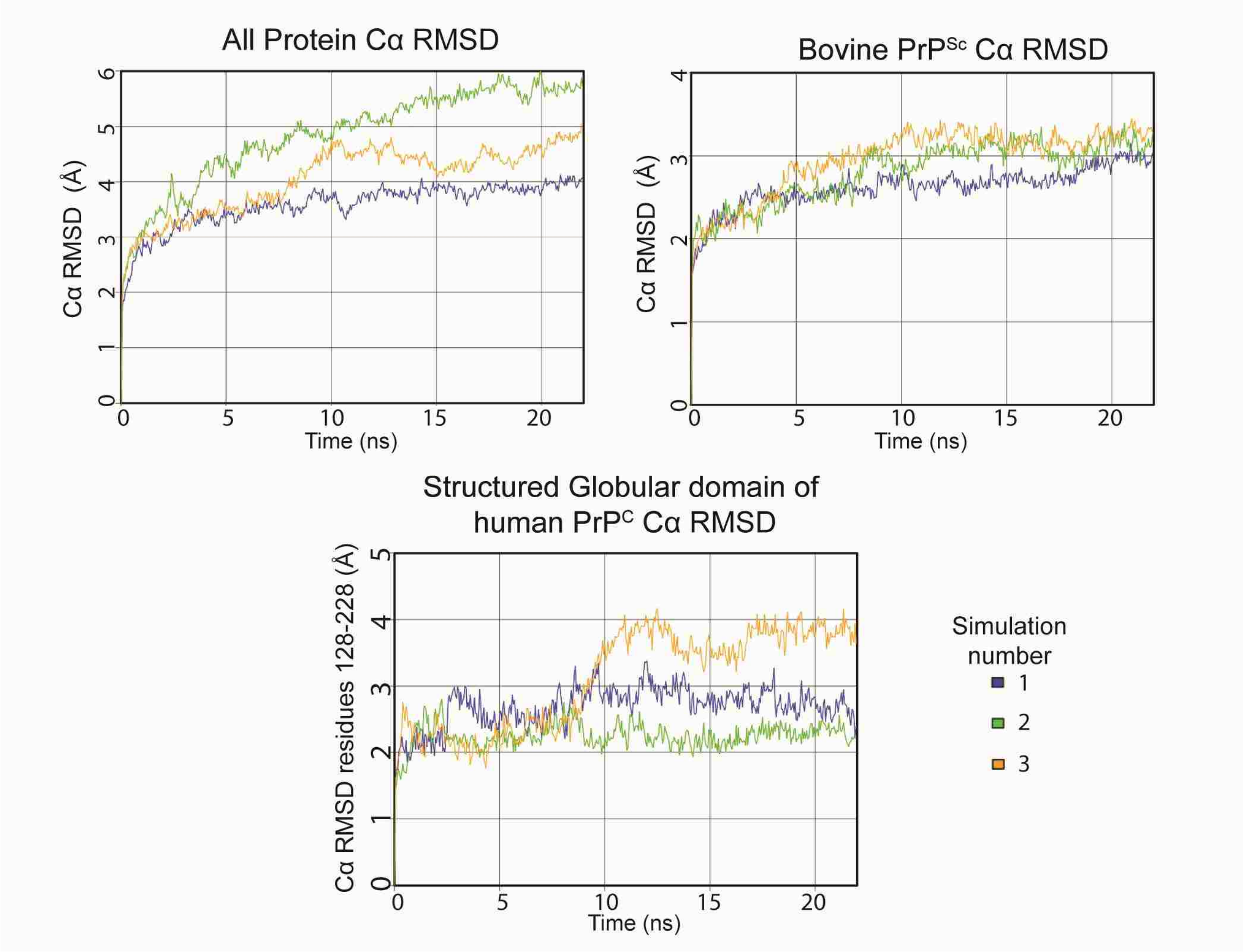

Figure 6.2 Cα RMSDs for proteins, bovine PrP^{Sc} and structured globular domain of PrP^{C}

Cα RMSDs were measured for all proteins, bovine PrP^{Sc} and residues 128-228 of the human membrane-bound PrP^{C}.

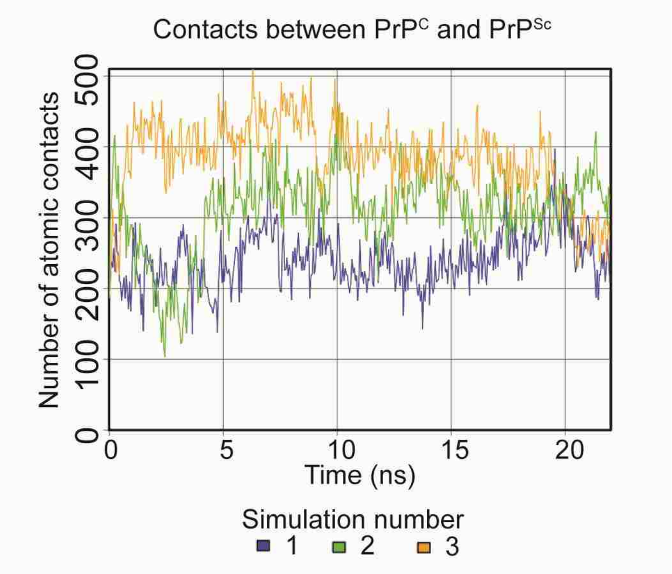

Figure 6.3 Contacts between PrP^{C} and PrP^{Sc}

Total contacts were measured between PrP^{C} and PrP^{Sc}.

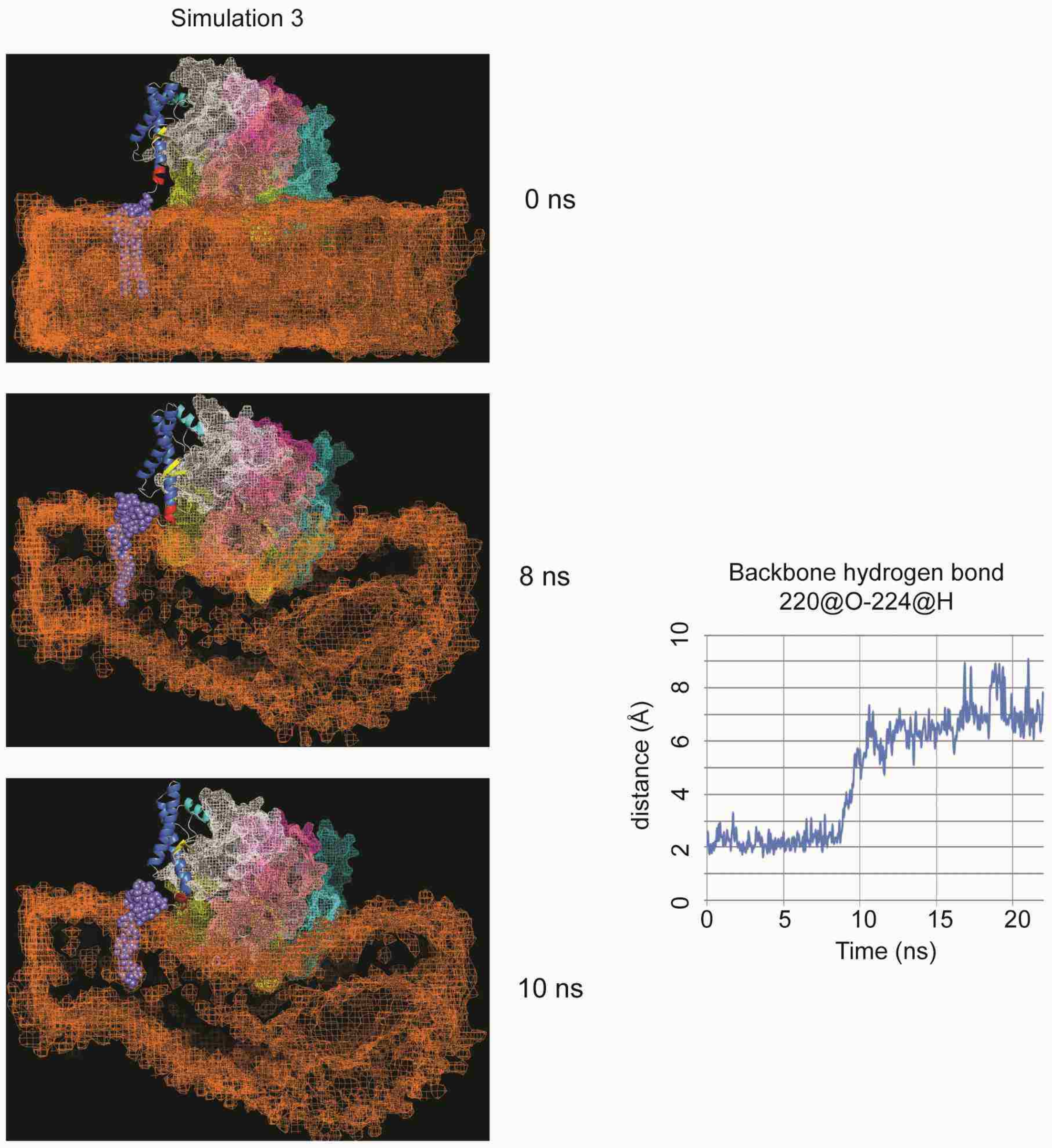

Figure 6.4 Simulation 3 of PrP^{C} + PrP^{Sc} system

Snapshots of the simulations are shown on the left panel. PrP^{C} is represented with cartoon ribbons. The PrP^{Sc} and the membrane are shown as mesh. Residues 220-224 are colored in red to show the region of helix HC that became bent at ~10 ns. Also notice the significant changes in the membrane topology and the formation of a void volume at the lower right corner of the membrane. Right panel shows the loss of the native backbone hydrogen bond at around 10 ns.

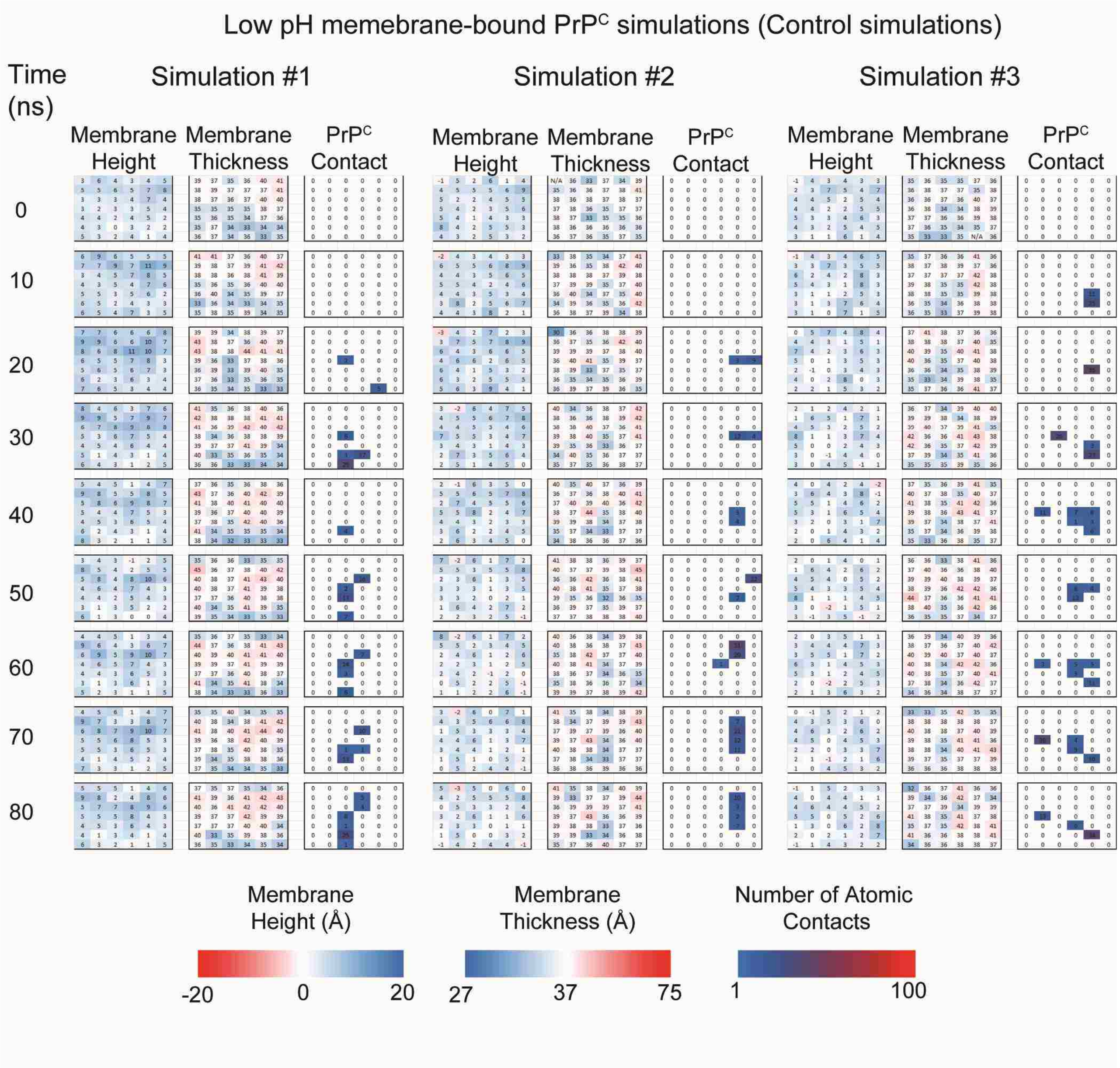

Figure 6.5 Membrane properties for control simulations

Membrane height, thickness and contacts with PrP^C were measured for every bin at 10 ns granularity. The subsequent figures also share the same color scale.

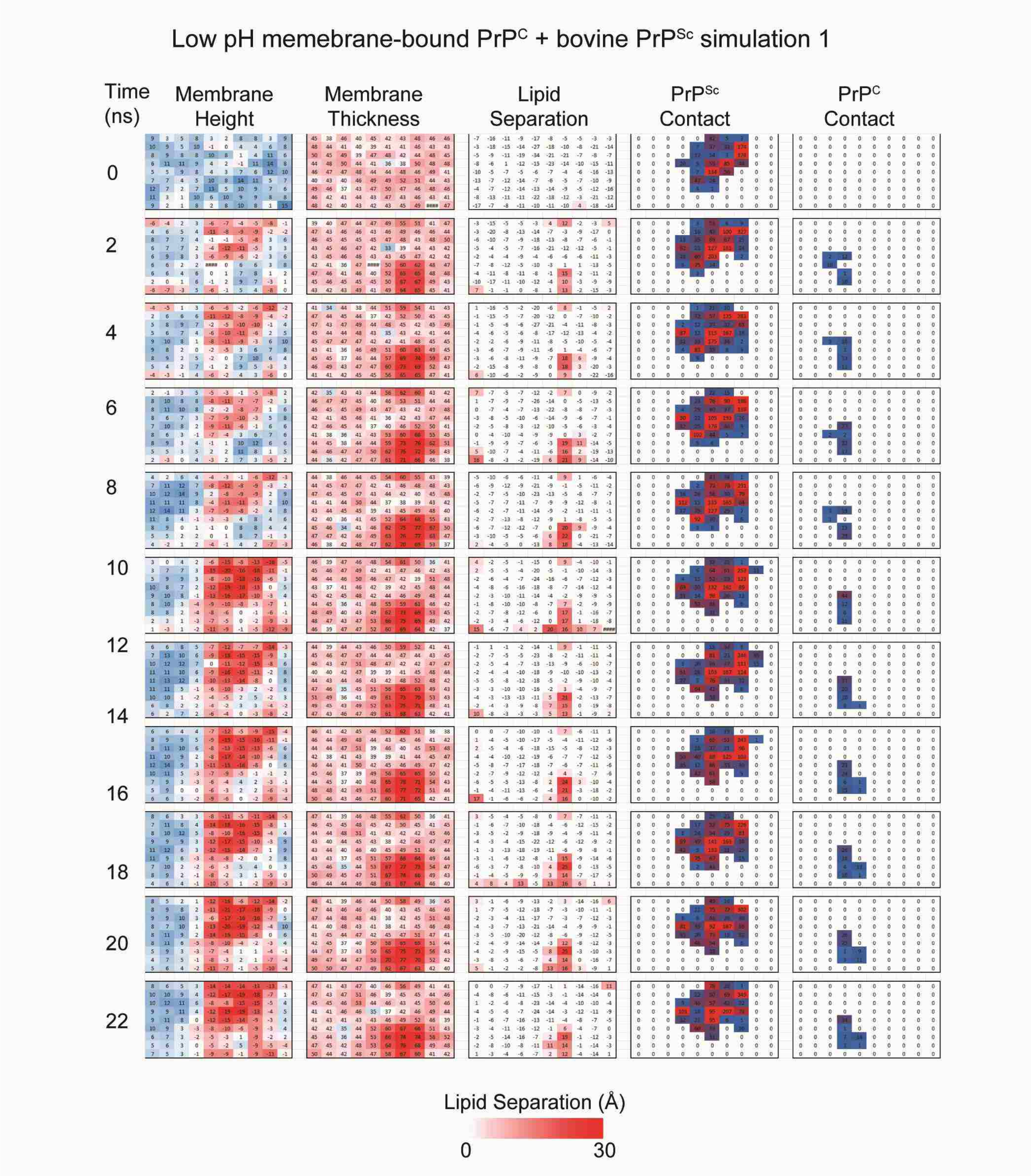

Figure 6.6 Membrane properties for simulation 1

Color scale is the same as that in Figure 6.5.

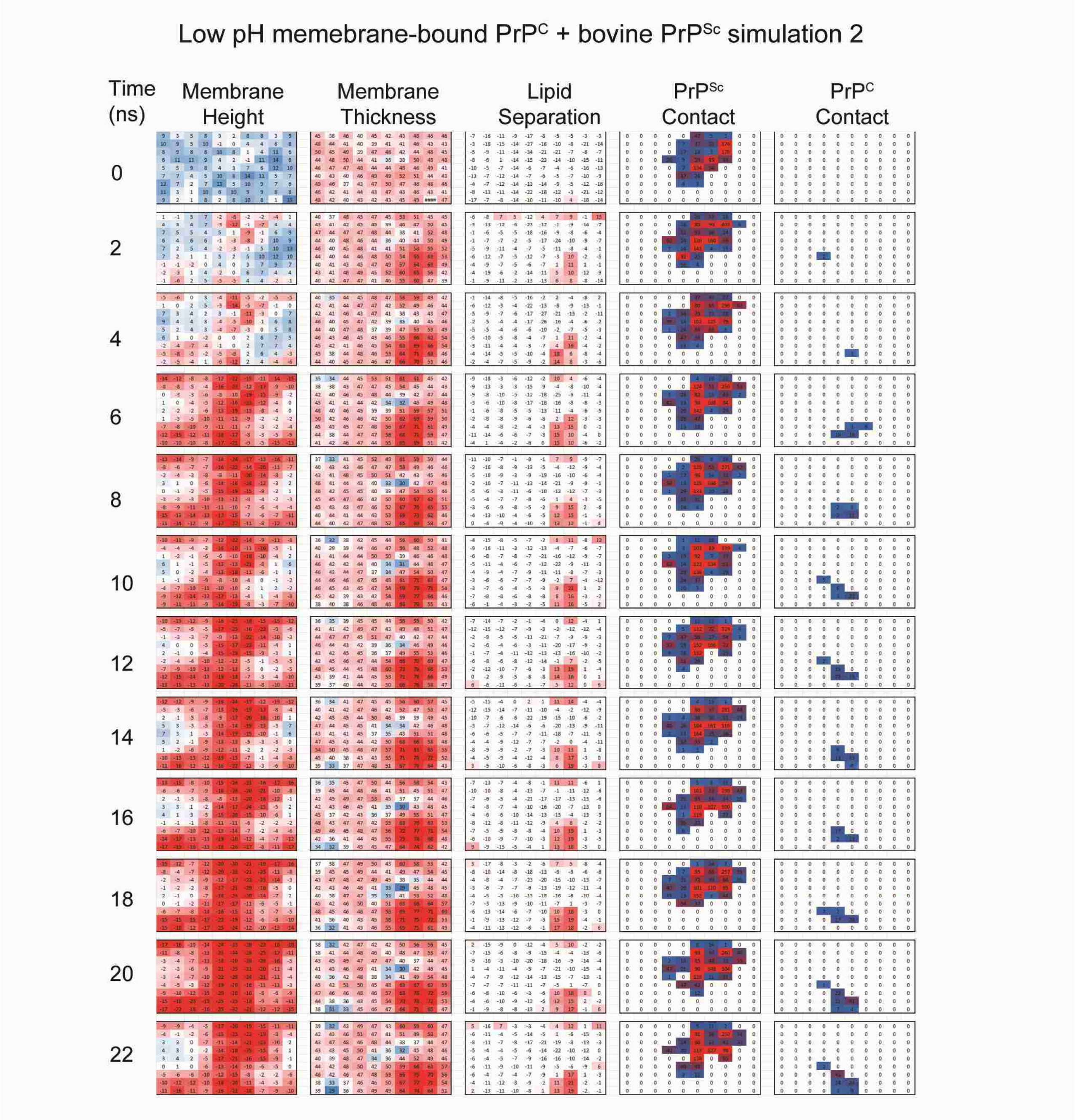

Figure 6.7 Membrane properties for simulation 2

Color scale is the same as that in Figure 6.6.

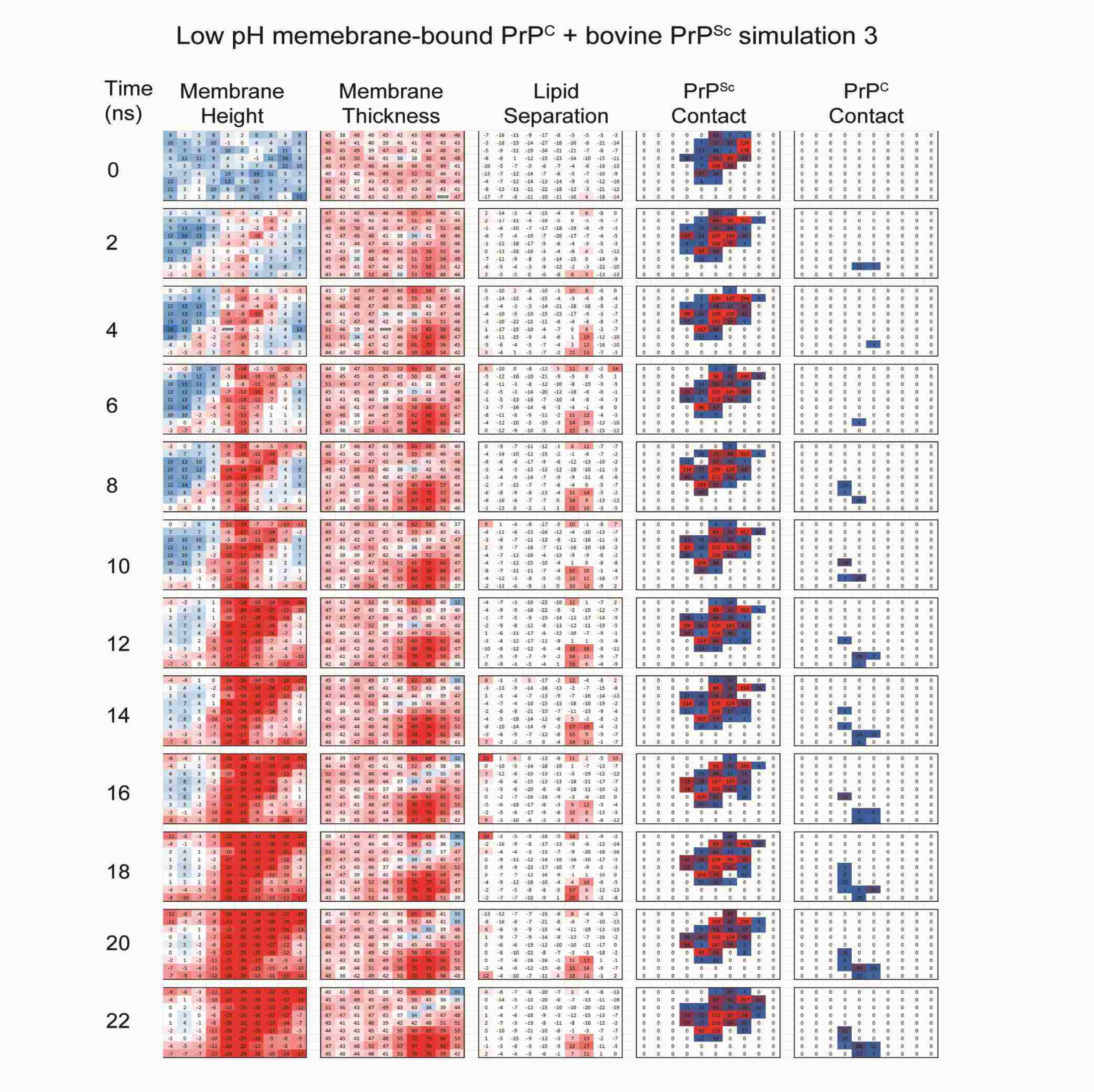

Figure 6.8 Membrane properties for simulation 3

Color scale is the same as that in Figure 6.6.

BIBLIOGRAPHY

1. Aguzzi, A., and A.M. Calella. 2009. Prions: Protein Aggregation and Infectious Diseases. Physiol Rev. 89: 1105–1152.
2. Aguzzi, A., F. Baumann, and J. Bremer. 2008. The Prion ' s Elusive Reason for Being. Annual Review of Neuroscience. 31: 439–477.
3. Almond, J., and J. Pattison. 1997. Human BSE. Nature. 389: 437–438.
4. Hill, A.F., M. Desbruslais, S. Joiner, K.C.L. Sidle, I. Gowland, J. Collinge, L.J. Doey, and P. Lantos. 1997. The same prion strain causes vCJD and BSE. Nature. 389: 448–450.
5. Haley, N.J., C.K. Mathiason, M.D. Zabel, G.C. Telling, and E.A. Hoover. 2009. Detection of sub-clinical CWD infection in conventional test-negative deer long after oral exposure to urine and feces from CWD+ deer. PLoS One. 4: e7990.
6. Mathiason, C.K., J.G. Powers, S.J. Dahmes, D.A. Osborn, K.V. Miller, R.J. Warren, G.L. Mason, S.A. Hays, J. Hayes-Klug, D.M. Seelig, M.A. Wild, L.L. Wolfe, T.R. Spraker, M.W. Miller, C.J. Sigurdson, G.C. Telling, and E.A. Hoover. 2006. Infectious Prions in the Saliva and Blood of Deer with Chronic Wasting Disease. Science. 314: 133–136.
7. Vascellari, M., R. Nonno, F. Mutinelli, M. Bigolaro, M.A. Di Bari, E. Melchiotti, S. Marcon, C. D'Agostino, G. Vaccari, and M. Conte. 2007. PrPSc in salivary glands of scrapie-affected sheep. Journal of virology. 81: 4872–4876.
8. Maddison, B.C., H.C. Rees, C.A. Baker, M. Taema, S.J. Bellworthy, L. Thorne, L.A. Terry, and K.C. Gough. 2010. Prions are secreted into the oral cavity in sheep with preclinical scrapie. Journal of Infectious Diseases. 201: 1672–1676.
9. USGS National Wildlife Health Center - Chronic Wasting Disease (CWD). .
10. Williams, E.S., M.W. Miller, T.J. Kreeger, R.H. Kahn, and E.T. Thorne. 2002. Chronic Wasting Disease of Deer and Elk: A Review with Recommendations for Management. The Journal of Wildlife Management. 66: 551–563.
11. Belay, E.D., R.A. Maddox, E.S. Williams, M.W. Miller, P. Gambetti, and L.B. Schonberger. 2004. Chronic Wasting Disease and Potential Transmission to Humans. Emerging Infectious Diseases. 10: 977–984.
12. Bartz, J.C., R.F. Marsh, D.I. McKenzie, and J.M. Aiken. 1998. The Host Range of Chronic Wasting Disease Is Altered on Passage in Ferrets. Virology. 251: 297–301.
13. Race, B., K.D. Meade-White, M.W. Miller, K.D. Barbian, R. Rubenstein, G. LaFauci, L. Cervenakova, C. Favara, D. Gardner, D. Long, M. Parnell, J. Striebel, S.A. Priola, A. Ward, E.S. Williams, R. Race, and B. Chesebro. 2009. Susceptibilities of Nonhuman Primates to Chronic Wasting Disease. Emerg Infect Dis. 15: 1366–1376.
14. Saunders, S.E., J.C. Bartz, and S.L. Bartelt-Hunt. 2012. Soil-mediated prion transmission: Is local soil-type a key determinant of prion disease incidence? Chemosphere. .
15. 2003. Australia lures Japanese beef buyers. ABC News. .

16. Sailer, A., H. Büeler, M. Fischer, A. Aguzzi, and C. Weissmann. 1994. No propagation of prions in mice devoid of PrP. Cell. 77: 967–968.
17. Büeler, H., A. Aguzzi, A. Sailer, R.-A. Greiner, P. Autenried, M. Aguet, and C. Weissmann. 1993. Mice devoid of PrP are resistant to scrapie. Cell. 73: 1339–1347.
18. Büeler, H., M. Fischer, Y. Lang, H. Bluethmann, H.-P. Lipp, S.J. DeArmond, S.B. Prusiner, M. Aguet, and C. Weissmann. 1992. Normal development and behaviour of mice lacking the neuronal cell-surface PrP protein. Nature. 356: 577–582.
19. Burns, C.S., E. Aronoff-Spencer, G. Legname, S.B. Prusiner, W.E. Antholine, G.J. Gerfen, J. Peisach, and G.L. Millhauser. 2003. Copper Coordination in the Full-Length, Recombinant Prion Protein†. Biochemistry. 42: 6794–6803.
20. Lasmézas, C.I. 2003. Putative functions of PrPC. Br Med Bull. 66: 61–70.
21. Le Pichon, C.E., M.T. Valley, M. Polymenidou, A.T. Chesler, B.T. Sagdullaev, A. Aguzzi, and S. Firestein. 2009. Olfactory behavior and physiology are disrupted in prion protein knockout mice. Nat Neurosci. 12: 60–69.
22. Swietnicki, W., R. Petersen, P. Gambetti, and W.K. Surewicz. 1997. pH-dependent stability and conformation of the recombinant human prion protein PrP(90-231). The Journal of Biological Chemistry. 272: 27517–27520.
23. Chianini, F., N. Fernández-Borges, E. Vidal, L. Gibbard, B. Pintado, J. de Castro, S.A. Priola, S. Hamilton, S.L. Eaton, J. Finlayson, Y. Pang, P. Steele, H.W. Reid, M.P. Dagleish, and J. Castilla. 2012. Rabbits are not resistant to prion infection. PNAS. .
24. Wang, F., X. Wang, C.-G. Yuan, and J. Ma. 2010. Generating a Prion with Bacterially Expressed Recombinant Prion Protein. Science. 327: 1132–1135.
25. Soto, C. 2011. Prion hypothesis: the end of the controversy? Trends in Biochemical Sciences. 36: 151–158.
26. Saborio, G.P., B. Permanne, and C. Soto. 2001. Sensitive detection of pathological prion protein by cyclic amplification of protein misfolding. Nature. 411: 810–813.
27. Meier, P., N. Genoud, M. Prinz, M. Maissen, T. Rülicke, A. Zurbriggen, A.J. Raeber, and A. Aguzzi. 2003. Soluble Dimeric Prion Protein Binds PrPSc In Vivo and Antagonizes Prion Disease. Cell. 113: 49–60.
28. Calzolai, L., and R. Zahn. 2003. Influence of pH on NMR structure and stability of the human prion protein globular domain. J. Biol. Chem. 278: 35592–35596.
29. James, T.L., H. Liu, N.B. Ulyanov, S. Farr-Jones, H. Zhang, D.G. Donne, K. Kaneko, D. Groth, I. Mehlhorn, S.B. Prusiner, and F.E. Cohen. 1997. Solution structure of a 142-residue recombinant prion protein corresponding to the infectious fragment of the scrapie isoform. Proc Natl Acad Sci U S A. 94: 10086–10091.
30. Lopez Garcia, F. 2000. NMR structure of the bovine prion protein. Proc. Natl. Acad. Sci. U.S.A. 97: 8334–8339.
31. Haire, L.F., S.M. Whyte, N. Vasisht, A.C. Gill, C. Verma, E.J. Dodson, G.G. Dodson, and P.M. Bayley. 2004. The Crystal Structure of the Globular Domain of Sheep Prion Protein. Journal of Molecular Biology. 336: 1175–1183.
32. Antonyuk, S.V., C.R. Trevitt, R.W. Strange, G.S. Jackson, D. Sangar, M. Batchelor, S. Cooper, C. Fraser, S. Jones, T. Georgiou, A. Khalili-Shirazi, A.R. Clarke, S.S. Hasnain, and

J. Collinge. 2009. Crystal Structure of Human Prion Protein Bound to a Therapeutic Antibody. PNAS. 106: 2554–2558.

33. Knaus, K.J., M. Morillas, W. Swietnicki, M. Malone, W.K. Surewicz, and V.C. Yee. 2001. Crystal structure of the human prion protein reveals a mechanism for oligomerization. Nature structural biology. 8: 770–4.
34. Pan, K.M., M. Baldwin, J. Nguyen, M. Gasset, A. Serban, D. Groth, I. Mehlhorn, Z. Huang, R.J. Fletterick, and F.E. Cohen. 1993. Conversion of alpha-helices into beta-sheets features in the formation of the scrapie prion proteins. PNAS. 90: 10962–10966.
35. Caughey, B.W., A. Dong, K.S. Bhat, D. Ernst, S.F. Hayes, and W.S. Caughey. 1991. Secondary structure analysis of the scrapie-associated protein PrP 27-30 in water by infrared spectroscopy. Biochemistry. 30: 7672–7680.
36. Jackson, G.S., A.F. Hill, C. Joseph, L. Hosszu, A. Power, J.P. Waltho, A.R. Clarke, and J. Collinge. 1999. Multiple folding pathways for heterologously expressed human prion protein. Biochimica et biophysica acta. 1431: 1–13.
37. Lennon, C.W., H.D. Cox, S.P. Hennelly, S.J. Chelmo, and M.A. McGuirl. 2007. Probing Structural Differences in Prion Protein Isoforms by Tyrosine Nitration†. Biochemistry. 46: 4850–4860.
38. Gong, B., A. Ramos, E. Vázquez-Fernández, C.J. Silva, J. Alonso, Z. Liu, and J.R. Requena. 2011. Probing structural differences between PrPC and PrPSc by surface nitration and acetylation: evidence of conformational change in the C-terminus. Biochemistry. 50: 4963–4972.
39. Vázquez-Fernández, E., J. Alonso, M.A. Pastrana, A. Ramos, L. Stitz, E. Vidal, I. Dynin, B. Petsch, C.J. Silva, and J.R. Requena. 2012. Structural Organization of Mammalian Prions as Probed by Limited Proteolysis. PLoS ONE. 7: e50111.
40. Lu, X., P.L. Wintrode, and W.K. Surewicz. 2007. β-Sheet core of human prion protein amyloid fibrils as determined by hydrogen/deuterium exchange. PNAS. 104: 1510–1515.
41. Wille, H., M.D. Michelitsch, V. Guénebaut, S. Supattapone, A. Serban, F.E. Cohen, D.A. Agard, and S.B. Prusiner. 2002. Structural studies of the scrapie prion protein by electron crystallography. PNAS. 99: 3563–3568.
42. Govaerts, C., H. Wille, S.B. Prusiner, and F.E. Cohen. 2004. Evidence for assembly of prions with left-handed β-helices into trimers. PNAS. 101: 8342–8347.
43. Wille, H., W. Bian, M. McDonald, A. Kendall, D.W. Colby, L. Bloch, J. Ollesch, A.L. Borovinskiy, F.E. Cohen, S.B. Prusiner, and G. Stubbs. 2009. Natural and Synthetic Prion Structure from X-Ray Fiber Diffraction. PNAS. 106: 16990–16995.
44. Van der Kamp, M.W., and V. Daggett. 2010. Influence of pH on the human prion protein: insights into the early steps of misfolding. Biophys. J. 99: 2289–98.
45. Garrec, J., I. Tavernelli, and U. Rothlisberger. 2013. Two Misfolding Routes for the Prion Protein around pH 4.5. PLoS Comput Biol. 9: e1003057.
46. Zhong, L., and J. Xie. 2009. Investigation of the Effect of Glycosylation on Human Prion Protein by Molecular Dynamics. Journal of Biomolecular Structure and Dynamics. 26: 525–533.

47. Campos, S.R.R., M. Machuqueiro, and A.M. Baptista. 2010. Constant-pH Molecular Dynamics Simulations Reveal a β-Rich Form of the Human Prion Protein. J. Phys. Chem. B. 114: 12692–12700.
48. Zhang, J., and D.D.W. Liu. 2011. Molecular Dynamics Studies on the Structural Stability of Wild-type Dog Prion Protein. Journal of Biomolecular Structure and Dynamics. 28: 861–869.
49. Huang, I.-Y. 2010. Molecular Dynamics Simulations of Human Prion Protein under the Different Temperatures. .
50. Alonso, D.O.V., S.J. DeArmond, F.E. Cohen, and V. Daggett. 2001. Mapping the early steps in the pH-induced conformational conversion of the prion protein. Proc. Natl. Acad. Sci. U.S.A. 98: 2985–2989.
51. DeMarco, M.L., and V. Daggett. 2004. From conversion to aggregation: Protofibril formation of the prion protein. Proc. Natl. Acad. Sci. U.S.A. 101: 2293–2298.
52. Scouras, A.D., and V. Daggett. 2008. Species variation in PrPSc protofibril models. J. Mater. Sci. 43: 3625–3637.
53. Abskharon, R.N.N., G. Giachin, A. Wohlkonig, S.H. Soror, E. Pardon, G. Legname, and J. Steyaert. 2014. Probing the N-Terminal β-Sheet Conversion in the Crystal Structure of the Human Prion Protein Bound to a Nanobody. J. Am. Chem. Soc. 136: 937–944.
54. DeMarco, M.L., J. Silveira, B. Caughey, and V. Daggett. 2006. Structural properties of prion protein protofibrils and fibrils: An experimental assessment of atomic models. Biochemistry. 45: 15573–15582.
55. Fontaine, S.N., and D.R. Brown. 2009. Mechanisms of Prion Protein Aggregation. Protein and Peptide Letters. 16: 14–26.
56. Morris, K.L., and L.C. Serpell. 2012. X-ray fibre diffraction studies of amyloid fibrils. In: Methods in molecular biology (Clifton, N.J.). . pp. 121–135.
57. Bocharova, O.V., L. Breydo, A.S. Parfenov, V.V. Salnikov, and I.V. Baskakov. 2005. In vitro Conversion of Full-length Mammalian Prion Protein Produces Amyloid Form with Physical Properties of PrPSc. Journal of Molecular Biology. 346: 645–659.
58. Hafner-Bratkovič, I., L. Gaedtke, A. Ondracka, P. Veranič, I. Vorberg, and R. Jerala. 2011. Effect of Hydrophobic Mutations in the H2-H3 Subdomain of Prion Protein on Stability and Conversion In Vitro and In Vivo. PLoS ONE. 6: e24238.
59. O'Sullivan, D.B.D., C.E. Jones, S.R. Abdelraheim, A.R. Thompsett, M.W. Brazier, H. Toms, D.R. Brown, and J.H. Viles. 2007. NMR characterization of the pH 4 β-intermediate of the prion protein: the N-terminal half of the protein remains unstructured and retains a high degree of flexibility. Biochemical Journal. 401: 533.
60. Gerber, R., A. Tahiri-Alaoui, P.J. Hore, and W. James. 2007. Oligomerization of the Human Prion Protein Proceeds via a Molten Globule Intermediate. J. Biol. Chem. 282: 6300–6307.
61. Bjorndahl, T.C., G.-P. Zhou, X. Liu, R. Perez-Pineiro, V. Semenchenko, F. Saleem, S. Acharya, A. Bujold, C.A. Sobsey, and D.S. Wishart. 2011. Detailed Biophysical Characterization of the Acid-Induced PrPc to PrPβ Conversion Process. Biochemistry. 50: 1162–1173.

62. Vendrely, C., H. Valadié, L. Bednarova, L. Cardin, M. Pasdeloup, J. Cappadoro, J. Bednar, M. Rinaudo, and M. Jamin. 2005. Assembly of the full-length recombinant mouse prion protein I. Formation of soluble oligomers. Biochimica et Biophysica Acta (BBA) - General Subjects. 1724: 355–366.
63. Cheng, C.J., and V. Daggett. 2015. Comparison of PrPSc models from a Soluble Oligomer Perspective. In preparation. .
64. Cheng, C.J., and V. Daggett. 2014. Molecular Dynamics Simulations Capture the Misfolding of the Bovine Prion Protein at Acidic pH. Biomolecules. 4: 181–201.
65. Wadsworth, J.D.F., and J. Collinge. 2011. Molecular pathology of human prion disease. Acta Neuropathol. 121: 69–77.
66. Head, M.W., and J.W. Ironside. 2012. Review: Creutzfeldt–Jakob disease: prion protein type, disease phenotype and agent strain. Neuropathology and Applied Neurobiology. 38: 296–310.
67. Gambetti, P., I. Cali, S. Notari, Q. Kong, W.-Q. Zou, and W.K. Surewicz. 2011. Molecular biology and pathology of prion strains in sporadic human prion diseases. Acta Neuropathol. 121: 79–90.
68. Bett, C., S. Joshi-Barr, M. Lucero, M. Trejo, P. Liberski, J.W. Kelly, E. Masliah, and C.J. Sigurdson. 2012. Biochemical properties of highly neuroinvasive prion strains. PLoS Pathog. 8: e1002522.
69. Puoti, G., A. Bizzi, G. Forloni, J.G. Safar, F. Tagliavini, and P. Gambetti. 2012. Sporadic human prion diseases: molecular insights and diagnosis. The Lancet Neurology. 11: 618–628.
70. Borchelt, D.R., M. Scott, A. Taraboulos, N. Stahl, and S.B. Prusiner. 1990. Scrapie and cellular prion proteins differ in their kinetics of synthesis and topology in cultured cells. J. Cell Biol. 110: 743–752.
71. Caughey, B., and G.J. Raymond. 1991. The scrapie-associated form of PrP is made from a cell surface precursor that is both protease- and phospholipase-sensitive. J. Biol. Chem. 266: 18217–18223.
72. Riek, R., S. Hornemann, G. Wider, M. Billeter, R. Glockshuber, and K. Wüthrich. 1996. NMR structure of the mouse prion protein domain PrP(121–231). Nature. 382: 180–182.
73. Zahn, R., A. Liu, T. Lührs, R. Riek, C. von Schroetter, F. López García, M. Billeter, L. Calzolai, G. Wider, and K. Wüthrich. 2000. NMR solution structure of the human prion protein. Proc. Natl. Acad. Sci. U.S.A. 97: 145–50.
74. Stöhr, J., J.C. Watts, G. Legname, A. Oehler, A. Lemus, H.-O.B. Nguyen, J. Sussman, H. Wille, S.J. DeArmond, S.B. Prusiner, and K. Giles. 2011. Spontaneous generation of anchorless prions in transgenic mice. Proc. Natl. Acad. Sci. U.S.A. 108: 21223–21228.
75. Chesebro, B., M. Trifilo, R. Race, K. Meade-White, C. Teng, R. LaCasse, L. Raymond, C. Favara, G. Baron, S. Priola, B. Caughey, E. Masliah, and M. Oldstone. 2005. Anchorless Prion Protein Results in Infectious Amyloid Disease Without Clinical Scrapie. Science. 308: 1435–1439.
76. Zou, W.-Q., S. Capellari, P. Parchi, M.-S. Sy, P. Gambetti, and S.G. Chen. 2003. Identification of Novel Proteinase K-resistant C-terminal Fragments of PrP in Creutzfeldt-Jakob Disease. J. Biol. Chem. 278: 40429–40436.

77. Norstrom, E.M., and J.A. Mastrianni. 2005. The AGAAAAGA palindrome in PrP is required to generate a productive PrPSc-PrPC complex that leads to prion propagation. J. Biol. Chem. 280: 27236–27243.
78. Jobling, M.F., L.R. Stewart, A.R. White, C. McLean, A. Friedhuber, F. Maher, K. Beyreuther, C.L. Masters, C.J. Barrow, S.J. Collins, and R. Cappai. 1999. The hydrophobic core sequence modulates the neurotoxic and secondary structure properties of the prion peptide 106-126. J. Neurochem. 73: 1557–1565.
79. Supattapone, S., P. Bosque, T. Muramoto, H. Wille, C. Aagaard, D. Peretz, H.-O.B. Nguyen, C. Heinrich, M. Torchia, J. Safar, F.E. Cohen, S.J. DeArmond, S.B. Prusiner, and M. Scott. 1999. Prion protein of 106 residues creates an artificial transmission barrier for prion replication in transgenic mice. Cell. 96: 869–878.
80. Solomon, I.H., N. Khatri, E. Biasini, T. Massignan, J.E. Huettner, and D.A. Harris. 2011. An N-terminal polybasic domain and cell surface localization are required for mutant prion protein toxicity. The Journal of Biological Chemistry. 286: 14724–14736.
81. Legname, G., I.V. Baskakov, H.-O.B. Nguyen, D. Riesner, F.E. Cohen, S.J. DeArmond, and S.B. Prusiner. 2004. Synthetic mammalian prions. Science. 305: 673–676.
82. Van der Kamp, M.W., and V. Daggett. 2009. The consequences of pathogenic mutations to the human prion protein. Protein Eng. Des. Sel. 22: 461–468.
83. Lloyd, S.E., S. Mead, and J. Collinge. 2013. Genetics of prion diseases. Current Opinion in Genetics & Development. 23: 345–351.
84. Beck, J.A., M. Poulter, T.A. Campbell, G. Adamson, J.B. Uphill, R. Guerreiro, G.S. Jackson, J.C. Stevens, H. Manji, J. Collinge, and S. Mead. 2010. PRNP allelic series from 19 years of prion protein gene sequencing at the MRC Prion Unit. Human Mutation. 31: E1551–E1563.
85. Giachin, G., I. Biljan, G. Ilc, J. Plavec, and G. Legname. 2013. Probing Early Misfolding Events in Prion Protein Mutants by NMR Spectroscopy. Molecules. 18: 9451–9476.
86. Liemann, S., and R. Glockshuber. 1999. Influence of amino acid substitutions related to inherited human prion diseases on the thermodynamic stability of the cellular prion protein. Biochemistry. 38: 3258–3267.
87. Swietnicki, W., R.B. Petersen, P. Gambetti, and W.K. Surewicz. 1998. Familial Mutations and the Thermodynamic Stability of the Recombinant Human Prion Protein. J. Biol. Chem. 273: 31048–31052.
88. Van der Kamp, M.W., and V. Daggett. 2010. Pathogenic mutations in the hydrophobic core of the human prion protein can promote structural instability and misfolding. J. Mol. Biol. 404: 732–748.
89. Alzualde, A., B. Indakoetxea, I. Ferrer, F. Moreno, M. Barandiaran, A. Gorostidi, A. Estanga, I. Ruiz, M. Calero, F.W. van Leeuwen, B. Atares, R. Juste, A.B. Rodriguez-Martínez, and A. López de Munain. 2010. A novel PRNP Y218N mutation in Gerstmann-Sträussler-Scheinker disease with neurofibrillary degeneration. J. Neuropathol. Exp. Neurol. 69: 789–800.
90. Peoc'h, K., P. Manivet, P. Beaudry, F. Attane, G. Besson, D. Hannequin, N. Delasnerie-Lauprêtre, and J.-L. Laplanche. 2000. Identification of three novel mutations (E196K,

V203I, E211Q) in the prion protein gene (PRNP) in inherited prion diseases with Creutzfeldt-Jakob disease phenotype. Human Mutation. 15: 482–482.

91. Riek, R., G. Wider, M. Billeter, S. Hornemann, R. Glockshuber, and K. Wüthrich. 1998. Prion protein NMR structure and familial human spongiform encephalopathies. Proc. Natl. Acad. Sci. U.S.A. 95: 11667–11672.
92. Daggett, V. 2006. Alpha-sheet: The toxic conformer in amyloid diseases? Acc. Chem. Res. 39: 594–602.
93. Armen, R.S., M.L. DeMarco, D.O.V. Alonso, and V. Daggett. 2004. Pauling and Corey's alpha-pleated sheet structure may define the prefibrillar amyloidogenic intermediate in amyloid disease. Proc. Natl. Acad. Sci. U.S.A. 101: 11622–7.
94. Forloni, G., N. Angeretti, R. Chiesa, E. Monzani, M. Salmona, O. Bugiani, and F. Tagliavini. 1993. Neurotoxicity of a prion protein fragment. Nature. 362: 543–546.
95. Lisa, S., M. Meli, G. Cabello, R. Gabizon, G. Colombo, and M. Gasset. 2010. The structural intolerance of the PrP alpha-fold for polar substitution of the helix-3 methionines. Cell. Mol. Life Sci. 67: 2825–2838.
96. DeMarco, M.L., and V. Daggett. 2007. Molecular mechanism for low pH triggered misfolding of the human prion protein. Biochemistry. 46: 3045–54.
97. Zuegg, J., and J.E. Gready. 1999. Molecular dynamics simulations of human prion protein: Importance of correct treatment of electrostatic interactions. Biochemistry. 38: 13862–13876.
98. Bamdad, K., and H. Naderi-Manesh. 2007. Contribution of a putative salt bridge and backbone dynamics in the structural instability of human prion protein upon R208H mutation. Biochem. Biophys. Res. Commun. 364: 719–724.
99. Langella, E., R. Improta, O. Crescenzi, and V. Barone. 2006. Assessing the acid–base and conformational properties of histidine residues in human prion protein (125–228) by means of pKa calculations and molecular dynamics simulations. Proteins. 64: 167–177.
100. Watanabe, Y., O. Inanami, M. Horiuchi, W. Hiraoka, Y. Shimoyama, F. Inagaki, and M. Kuwabara. 2006. Identification of pH-sensitive regions in the mouse prion by the cysteine-scanning spin-labeling ESR technique. Biochem. Biophys. Res. Commun. 350: 549–556.
101. Hosszu, L.L.P., M.A. Wells, G.S. Jackson, S. Jones, M. Batchelor, A.R. Clarke, C.J. Craven, J.P. Waltho, and J. Collinge. 2005. Definable equilibrium states in the folding of human prion protein. Biochemistry. 44: 16649–16657.
102. Torrent, J., M.T. Alvarez-Martinez, J.-P. Liautard, C. Balny, and R. Lange. 2005. The role of the 132–160 region in prion protein conformational transitions. Prot. Sci. 14: 956–967.
103. Alonso, D.O.V., C. An, and V. Daggett. 2002. Simulations of biomolecules: Characterization of the early steps in the pH-induced conformational conversion of the hamster, bovine and human forms of the prion protein. Phil. Trans. R. Soc. Lond. A. 360: 1165–1178.
104. Colacino, S., G. Tiana, R.A. Broglia, and G. Colombo. 2006. The determinants of stability in the human prion protein: Insights into folding and misfolding from the analysis of the change in the stabilization energy distribution in different conditions. Proteins. 62: 698–707.

105. De Simone, A., A. Zagari, and P. Derreumaux. 2007. Structural and hydration properties of the partially unfolded states of the prion protein. Biophys. J. 93: 1284–1292.
106. Eghiaian, F., T. Daubenfeld, Y. Quenet, M. van Audenhaege, A.-P. Bouin, G. van der Rest, J. Grosclaude, and H. Rezaei. 2007. Diversity in prion protein oligomerization pathways results from domain expansion as revealed by hydrogen/deuterium exchange and disulfide linkage. Proc. Natl. Acad. Sci. U.S.A. 104: 7414–7419.
107. Hafner-Bratkovič, I., R. Bester, P. Pristovšek, L. Gaedtke, P. Veranič, J. Gašperšič, M. Manček-Keber, M. Avbelj, M. Polymenidou, C. Julius, A. Aguzzi, I. Vorberg, and R. Jerala. 2011. Globular domain of the prion protein needs to be unlocked by domain swapping to support prion protein conversion. J. Biol. Chem. 286: 12149–12156.
108. Zhang, Y., J. Qian, P.-Y. Wang, and Z.-C. Ou-Yang. 2006. Molecular dynamical simulations of point mutation occurring at the 198-th site of prion protein. J. Comput. Theor. Nanosci. 3: 964–969.
109. Zhang, Y., L. Dai, M. Iwamoto, and Z. Ou-Yang. 2006. Molecular dynamics study on the conformational transition of prion induced by the point mutation: F198S. Thin Solid Films. 499: 224–228.
110. Vanik, D.L., and W.K. Surewicz. 2002. Disease-associated F198S mutation increases the propensity of the recombinant prion protein for conformational conversion to scrapie-like form. J. Biol. Chem. 277: 49065–49070.
111. Julien, O., S. Chatterjee, A. Thiessen, S.P. Graether, and B.D. Sykes. 2009. Differential stability of the bovine prion protein upon urea unfolding. Prot. Sci. 18: 2172–2182.
112. Jones, M., V. McLoughlin, J.G. Connolly, C.F. Farquhar, I.R. MacGregor, and M.W. Head. 2009. Production and characterization of a panel of monoclonal antibodies against native human cellular prion protein. Hybridoma. 28: 13–20.
113. Hart, T., L.L.P. Hosszu, C.R. Trevitt, G.S. Jackson, J.P. Waltho, J. Collinge, and A.R. Clarke. 2009. Folding kinetics of the human prion protein probed by temperature jump. Proc. Natl. Acad. Sci. U.S.A. 106: 5651–6.
114. Kachel, N., W. Kremer, R. Zahn, and H.R. Kalbitzer. 2006. Observation of intermediate states of the human prion protein by high pressure NMR spectroscopy. BMC Struct. Biol. 6: 16.
115. Abalos, G.C., J.T. Cruite, A. Bellon, S. Hemmers, J. Akagi, J.A. Mastrianni, R.A. Williamson, and L. Solforosi. 2008. Identifying key components of the PrPC-PrPSc replicative interface. J. Biol. Chem. 283: 34021–34028.
116. Resenberger, U.K., A. Harmeier, A.C. Woerner, J.L. Goodman, V. Müller, R. Krishnan, R.M. Vabulas, H.A. Kretzschmar, S. Lindquist, F.U. Hartl, G. Multhaup, K.F. Winklhofer, and J. Tatzelt. 2011. The cellular prion protein mediates neurotoxic signalling of β-sheet-rich conformers independent of prion replication. EMBO J. 30: 2057–2070.
117. Rambold, A.S., V. Muller, U. Ron, N. Ben-Tal, K.F. Winklhofer, and J. Tatzelt. 2008. Stress-protective signalling of prion protein is corrupted by scrapie prions. EMBO J. 27: 1974–1984.
118. Supattapone, S., E. Bouzamondo, H.L. Ball, H. Wille, H.-O.B. Nguyen, F.E. Cohen, S.J. DeArmond, S.B. Prusiner, and M. Scott. 2001. A protease-resistant 61-residue prion peptide causes neurodegeneration in transgenic mice. Mol. Cell. Biol. 21: 2608–2616.

119. Kundu, B., N.R. Maiti, E.M. Jones, K.A. Surewicz, D.L. Vanik, and W.K. Surewicz. 2003. Nucleation-dependent conformational conversion of the Y145Stop variant of human prion protein: Structural clues for prion propagation. Proc. Natl. Acad. Sci. U.S.A. 100: 12069–12074.
120. Helmus, J.J., K. Surewicz, P.S. Nadaud, W.K. Surewicz, and C.P. Jaroniec. 2008. Molecular conformation and dynamics of the Y145Stop variant of human prion protein in amyloid fibrils. Proc. Natl. Acad. Sci. U.S.A. 105: 6284–6289.
121. Chen, W., M.W. van der Kamp, and V. Daggett. 2010. Diverse effects on the native β-sheet of the human prion protein due to disease-associated mutations. Biochemistry. 49: 9874–9881.
122. Sigurdson, C.J., S. Joshi-Barr, C. Bett, O. Winson, G. Manco, P. Schwarz, T. Rülicke, K.P.R. Nilsson, I. Margalith, A. Raeber, D. Peretz, S. Hornemann, K. Wüthrich, and A. Aguzzi. 2011. Spongiform encephalopathy in transgenic mice expressing a point mutation in the β2–α2 loop of the prion protein. J. Neurosci. 31: 13840–13847.
123. Scouras, A.D., and V. Daggett. 2012. Disruption of the X-loop turn of the prion protein linked to scrapie resistance. Protein Eng. Des. Sel. 25: 243–249.
124. Safar, J., H. Wille, V. Itri, D. Groth, H. Serban, M. Torchia, F.E. Cohen, and S.B. Prusiner. 1998. Eight prion strains have PrPSc molecules with different conformations. Nat. Med. 4: 1157–1165.
125. Nilsson, K.P.R., S. Joshi-Barr, O. Winson, and C.J. Sigurdson. 2010. Prion Strain Interactions Are Highly Selective. J. Neurosci. 30: 12094–12102.
126. Makarava, N., G.G. Kovacs, R. Savtchenko, I. Alexeeva, H. Budka, R.G. Rohwer, and I.V. Baskakov. 2011. Genesis of Mammalian Prions: From Non-infectious Amyloid Fibrils to a Transmissible Prion Disease. PLoS Pathog. 7: e1002419.
127. Scouras, A.D., and V. Daggett. 2011. The dynameomics rotamer library: Amino acid side chain conformations and dynamics from comprehensive molecular dynamics simulations in water. Prot. Sci. 20: 341–352.
128. Van der Kamp, M.W., R.D. Schaeffer, A.L. Jonsson, A.D. Scouras, A.M. Simms, R.D. Toofanny, N.C. Benson, P.C. Anderson, E.D. Merkley, S. Rysavy, D. Bromley, D.A.C. Beck, and V. Daggett. 2010. Dynameomics: A comprehensive database of protein dynamics. Structure. 18: 423–435.
129. Beck, D.A.C., M.E. McCully, D.O.V. Alonso, and V. Daggett. 2000. in lucem Molecular Mechanics (ilmm). University of Washington, Seattle: .
130. Levitt, M., M. Hirshberg, R. Sharon, and V. Daggett. 1995. Potential energy function and parameters for simulations of the molecular dynamics of proteins and nucleic acids in solution. Comput. Phys. Commun. 91: 215–231.
131. Levitt, M., M. Hirshberg, R. Sharon, K.E. Laidig, and V. Daggett. 1997. Calibration and testing of a water model for simulation of the molecular dynamics of proteins and nucleic acids in solution. J. Phys. Chem. B. 101: 5051–5061.
132. Beck, D.A.C., and V. Daggett. 2004. Methods for molecular dynamics simulations of protein folding/unfolding in solution. Methods San Diego Calif. 34: 112–20.
133. Lee, B., and F.M. Richards. 1971. The interpretation of protein structures: Estimation of static accessibility. J. Mol. Biol. 55: 379–400.

134. Kabsch, W., and C. Sander. 1983. Dictionary of protein secondary structure: pattern recognition of hydrogen-bonded and geometrical features. Biopolymers. 22: 2577–637.
135. Prusiner, S.B., M.R. Scott, S.J. DeArmond, and F.E. Cohen. 1998. Prion Protein Biology. Cell. 93: 337–348.
136. Prusiner, S.B. 1991. Molecular biology of prion diseases. Science. 252: 1515–1522.
137. Collinge, J. 1999. Variant Creutzfeldt-Jakob disease. The Lancet. 354: 317–323.
138. Hosszu, L.L.P., M.H. Tattum, S. Jones, C.R. Trevitt, M.A. Wells, J.P. Waltho, J. Collinge, G.S. Jackson, and A.R. Clarke. 2010. The H187R Mutation of the Human Prion Protein Induces Conversion of Recombinant Prion Protein to the PrPSc-like Form. Biochemistry. 49: 8729–8738.
139. Adrover, M., K. Pauwels, S. Prigent, C. de Chiara, Z. Xu, C. Chapuis, A. Pastore, and H. Rezaei. 2010. Prion Fibrillization Is Mediated by a Native Structural Element That Comprises Helices H2 and H3. J. Biol. Chem. 285: 21004–21012.
140. Gerber, R., A. Tahiri-Alaoui, and P. Hore. 2008. Conformational pH dependence of intermediate states during oligomerization of the human prion protein. Prot. Sci. 17: 537–544.
141. Hornemann, S., and R. Glockshuber. 1998. A scrapie-like unfolding intermediate of the prion protein domain PrP(121–231) induced by acidic pH. PNAS. 95: 6010–6014.
142. Swietnicki, W., R. Petersen, P. Gambetti, and W.K. Surewicz. 1997. pH-dependent Stability and Conformation of the Recombinant Human Prion Protein PrP(90–231). J. Biol. Chem. 272: 27517–27520.
143. Harris, D.A. 2003. Trafficking, Turnover and Membrane Topology of PrP Protein Function in Prion Disease. Br Med Bull. 66: 71–85.
144. Mironov, A., D. Latawiec, H. Wille, E. Bouzamondo-Bernstein, G. Legname, R.A. Williamson, D. Burton, S.J. DeArmond, S.B. Prusiner, and P.J. Peters. 2003. Cytosolic Prion Protein in Neurons. J. Neurosci. 23: 7183–7193.
145. Roos, A., and W.F. Boron. 1982. Intracellular pH. Physiol Rev. 62: 1377–1377.
146. Aubry, L., G. Klein, J.L. Martiel, and M. Satre. 1993. Kinetics of endosomal pH evolution in Dictyostelium discoideum amoebae. Study by fluorescence spectroscopy. J Cell Sci. 105: 861–866.
147. Arnold, J.E., C. Tipler, L. Laszlo, J. Hope, M. Landon, and R.J. Mayer. 1995. The abnormal isoform of the prion protein accumulates in late-endosome-like organelles in scrapie-infected mouse brain. The Journal of Pathology. 176: 403–411.
148. Borchelt, D.R., A. Taraboulos, and S.B. Prusiner. 1992. Evidence for synthesis of scrapie prion proteins in the endocytic pathway. J. Biol. Chem. 267: 16188–16199.
149. Caughey, B., G.J. Raymond, D. Ernst, and R.E. Race. 1991. N-terminal truncation of the scrapie-associated form of PrP by lysosomal protease(s): implications regarding the site of conversion of PrP to the protease-resistant state. Journal of virology. 65: 6597–603.
150. Godsave, S.F., H. Wille, P. Kujala, D. Latawiec, S.J. DeArmond, A. Serban, S.B. Prusiner, and P.J. Peters. 2008. Cryo-immunogold electron microscopy for prions: toward identification of a conversion site. The Journal of neuroscience : the official journal of the Society for Neuroscience. 28: 12489–99.

151. Matsunaga, Y., D. Peretz, A. Williamson, D. Burton, I. Mehlhorn, D. Groth, F.E. Cohen, S.B. Prusiner, and M.A. Baldwin. 2001. Cryptic epitopes in N-terminally truncated prion protein are exposed in the full-length molecule: dependence of conformation on pH. Proteins. 44: 110–118.
152. DeMarco, M.L., and V. Daggett. 2009. Characterization of cell-surface prion protein relative to its recombinant analogue: insights from molecular dynamics simulations of diglycosylated, membrane-bound human prion protein. J. Neurochem. 109: 60–73.
153. Paramithiotis, E., M. Pinard, T. Lawton, S. LaBoissiere, V.L. Leathers, W.-Q. Zou, L.A. Estey, J. Lamontagne, M.T. Lehto, L.H. Kondejewski, G.P. Francoeur, M. Papadopoulos, A. Haghighat, S.J. Spatz, M. Head, R. Will, J. Ironside, K. O'Rourke, Q. Tonelli, H.C. Ledebur, A. Chakrabartty, and N.R. Cashman. 2003. A prion protein epitope selective for the pathologically misfolded conformation. Nature Medicine. 9: 893–899.
154. Hirschberger, T., M. Stork, B. Schropp, K.F. Winklhofer, J. Tatzelt, and P. Tavan. 2006. Structural instability of the prion protein upon M205S/R mutations revealed by molecular dynamics simulations. Biophys. J. 90: 3908–3918.
155. Palmer, M.S., A.J. Dryden, J.T. Hughes, and J. Collinge. 1991. Homozygous prion protein genotype predisposes to sporadic Creutzfeldt–Jakob disease. Nature. 352: 340–342.
156. Schätzl, H.M., F. Wopfner, S. Gilch, A. von Brunn, and G. Jäger. 1997. Is codon 129 of prion protein polymorphic in human beings but not in animals? The Lancet. 349: 1603–1604.
157. Green, K.M., S.R. Browning, T.S. Seward, J.E. Jewell, D.L. Ross, M.A. Green, E.S. Williams, E.A. Hoover, and G.C. Telling. 2008. The elk PRNP codon 132 polymorphism controls cervid and scrapie prion propagation. The Journal of general virology. 89: 598–608.
158. Chen, W., M.W. Van der Kamp, and V. Daggett. 2014. Structural and dynamic properties of the human prion protein. Biophysical Journal. .
159. Selvaggini, C., L. Degioia, L. Cantu, E. Ghibaudi, L. Diomede, F. Passerini, G. Forloni, O. Bugiani, F. Tagliavini, and M. Salmona. 1993. Molecular Characteristics of a Protease-Resistant, Amyloidogenic and Neurotoxic Peptide Homologous to Residues 106-126 of the Prion Protein. Biochemical and Biophysical Research Communications. 194: 1380–1386.
160. De Gioia, L., C. Selvaggini, E. Ghibaudi, L. Diomede, O. Bugiani, G. Forloni, F. Tagliavini, and M. Salmona. 1994. Conformational polymorphism of the amyloidogenic and neurotoxic peptide homologous to residues 106-126 of the prion protein. J. Biol. Chem. 269: 7859–7862.
161. Brown, D.R., B. Schmidt, and H.A. Kretzschmar. 1996. Role of microglia and host prion protein in neurotoxicity of a prion protein fragment. Nature. 380: 345–347.
162. Armen, R.S., B.M. Bernard, R. Day, D.O.V. Alonso, and V. Daggett. 2005. Characterization of a possible amyloidogenic precursor in glutamine-repeat neurodegenerative diseases. Proceedings of the National Academy of Sciences of the United States of America. 102: 13433–13438.
163. Baylis, M., and W. Goldmann. 2004. The Genetics of Scrapie in Sheep and Goats. Current Molecular Medicine. 4: 385–396.

164. Gambetti, P., P. Parchi, R.B. Petersen, S.G. Chen, and E. Lugaresi. 1995. Fatal familial insomnia and familial Creutzfeldt-Jakob disease: clinical, pathological and molecular features. Brain Pathol. 5: 43–51.
165. Gsponer, J., P. Ferrara, and A. Caflisch. 2001. Flexibility of the murine prion protein and its Asp178Asn mutant investigated by molecular dynamics simulations. J. Mol. Graph. Model. 20: 169–182.
166. Kaneko, K., L. Zulianello, M. Scott, C.M. Cooper, A.C. Wallace, T.L. James, F.E. Cohen, and S.B. Prusiner. 1997. Evidence for protein X binding to a discontinuous epitope on the cellular prion protein during scrapie prion propagation. Proceedings of the National Academy of Sciences of the United States of America. 94: 10069–74.
167. Muramoto, T., M. Scott, F.E. Cohen, and S.B. Prusiner. 1996. Recombinant scrapie-like prion protein of 106 amino acids is soluble. PNAS. 93: 15457–15462.
168. Kell, G.S. 1967. Precise representation of volume properties of water at one atmosphere. J. Chem. Eng. Data. 12: 66–69.
169. Beck, D.A.C., R.S. Armen, and V. Daggett. 2005. Cutoff size does strongly influence molecular dynamics results on solvated polypeptides. Biochemistry. 44: 5856–5860.
170. Humphrey, W., A. Dalke, and K. Schulten. 1996. VMD – Visual Molecular Dynamics. Journal of Molecular Graphics. 14: 33–38.
171. Gambetti, P., Q. Kong, W. Zou, P. Parchi, and S.G. Chen. 2003. Sporadic and familial CJD: classification and characterisation. Br Med Bull. 66: 213–239.
172. DeArmond, S.J., H. Sánchez, F. Yehiely, Y. Qiu, A. Ninchak-Casey, V. Daggett, A.P. Camerino, J. Cayetano, M. Rogers, D. Groth, M. Torchia, P. Tremblay, M.R. Scott, F.E. Cohen, and S.B. Prusiner. 1997. Selective Neuronal Targeting in Prion Disease. Neuron. 19: 1337–1348.
173. DeArmond, S.J., Y. Qiu, H. Sànchez, P.R. Spilman, A. Ninchak-Casey, D. Alonso, and V. Daggett. 1999. PrPc glycoform heterogeneity as a function of brain region: implications for selective targeting of neurons by prion strains. J. Neuropathol. Exp. Neurol. 58: 1000–1009.
174. Mouillet-Richard, S., M. Ermonval, C. Chebassier, J.L. Laplanche, S. Lehmann, J.M. Launay, and O. Kellermann. 2000. Signal Transduction Through Prion Protein. Science. 289: 1925–1928.
175. Linden, R., V.R. Martins, M.A.M. Prado, M. Cammarota, I. Izquierdo, and R.R. Brentani. 2008. Physiology of the Prion Protein. Physiol Rev. 88: 673–728.
176. Millhauser, G.L. 2007. Copper and the Prion Protein: Methods, Structures, Function, and Disease. Annual Review of Physical Chemistry. 58: 299–320.
177. Klewpatinond, M., P. Davies, S. Bowen, D.R. Brown, and J.H. Viles. 2008. Deconvoluting the Cu2+ Binding Modes of Full-length Prion Protein. J. Biol. Chem. 283: 1870–1881.
178. Singh, A., A.O. Isaac, X. Luo, M.L. Mohan, M.L. Cohen, F. Chen, Q. Kong, J. Bartz, and N. Singh. 2009. Abnormal Brain Iron Homeostasis in Human and Animal Prion Disorders. PLoS Pathog. 5: e1000336.
179. Rudd, P.M., T. Endo, C. Colominas, D. Groth, S.F. Wheeler, D.J. Harvey, M.R. Wormald, H. Serban, S.B. Prusiner, A. Kobata, and R.A. Dwek. 1999. Glycosylation differences between the normal and pathogenic prion protein isoforms. PNAS. 96: 13044–13049.

180. DeMarco, M.L., and V. Daggett. 2005. Local environmental effects on the structure of the prion protein. Comptes rendus biologies. 328: 847–62.
181. Collinge, J., K.C.L. Sidle, J. Meads, J. Ironside, and A.F. Hill. 1996. Molecular analysis of prion strain variation and the aetiology of “new variant” CJD. Nature. 383: 685–690.
182. Hornemann, S., C. Schorn, and K. Wüthrich. 2004. NMR structure of the bovine prion protein isolated from healthy calf brains. EMBO Rep. 5: 1159–1164.
183. Lee, S.-W., Y. Mou, S.-Y. Lin, F.-C. Chou, W.-H. Tseng, C. Chen, C.-Y.D. Lu, S.S.-F. Yu, and J.C.C. Chan. 2008. Steric Zipper of the Amyloid Fibrils Formed by Residues 109–122 of the Syrian Hamster Prion Protein. Journal of Molecular Biology. 378: 1142–1154.
184. Silva, R.A.G.D., W. Barber-Armstrong, and S.M. Decatur. 2003. The Organization and Assembly of a β-Sheet Formed by a Prion Peptide in Solution: An Isotope-Edited FTIR Study. J. Am. Chem. Soc. 125: 13674–13675.
185. Walsh, P., P. Neudecker, and S. Sharpe. 2010. Structural Properties and Dynamic Behavior of Nonfibrillar Oligomers Formed by PrP(106−126). J. Am. Chem. Soc. 132: 7684–7695.
186. Cheng, H.-M., T.W.T. Tsai, W.Y.C. Huang, H.-K. Lee, H.-Y. Lian, F.-C. Chou, Y. Mou, and J.C.C. Chan. 2011. Steric Zipper Formed by Hydrophobic Peptide Fragment of Syrian Hamster Prion Protein. Biochemistry. 50: 6815–6823.
187. Baron, G.S., K. Wehrly, D.W. Dorward, B. Chesebro, and B. Caughey. 2002. Conversion of raft associated prion protein to the protease-resistant state requires insertion of PrP-res (PrPSc) into contiguous membranes. EMBO J. 21: 1031–1040.
188. Lin, S.-J., K.-H. Yu, J.-R. Wu, C.-F. Lee, C.-P. Jheng, H.-R. Chen, and C.-I. Lee. 2013. Liberation of GPI-Anchored Prion from Phospholipids Accelerates Amyloidogenic Conversion. International Journal of Molecular Sciences. 14: 17943–17957.
189. Baron, G.S., and B. Caughey. 2003. Effect of Glycosylphosphatidylinositol Anchor-dependent and -independent Prion Protein Association with Model Raft Membranes on Conversion to the Protease-resistant Isoform. J. Biol. Chem. 278: 14883–14892.
190. Zhang, Y., W. Swietnicki, M.G. Zagorski, W.K. Surewicz, and F.D. Sönnichsen. 2000. Solution Structure of the E200K Variant of Human Prion Protein IMPLICATIONS FOR THE MECHANISM OF PATHOGENESIS IN FAMILIAL PRION DISEASES. J. Biol. Chem. 275: 33650–33654.
191. Sanghera, N., and T.J.T. Pinheiro. 2002. Binding of prion protein to lipid membranes and implications for prion conversion. Journal of Molecular Biology. 315: 1241–1256.
192. Wang, F., S. Yin, X. Wang, L. Zha, M.-S. Sy, and J. Ma. 2010. Role of the highly conserved middle region of prion protein (PrP) in PrP-lipid interaction. Biochemistry. 49: 8169–8176.
193. Boland, M.P., C.R. Hatty, F. Separovic, A.F. Hill, D.J. Tew, K.J. Barnham, C.L. Haigh, M. James, C.L. Masters, and S.J. Collins. 2010. Anionic Phospholipid Interactions of the Prion Protein N Terminus Are Minimally Perturbing and Not Driven Solely by the Octapeptide Repeat Domain. J. Biol. Chem. 285: 32282–32292.
194. Morillas, M., W. Swietnicki, P. Gambetti, and W.K. Surewicz. 1999. Membrane Environment Alters the Conformational Structure of the Recombinant Human Prion Protein. J. Biol. Chem. 274: 36859–36865.

195. Pan, T., B.-S. Wong, T. Liu, R. Li, R.B. Petersen, and M.-S. Sy. 2002. Cell-surface prion protein interacts with glycosaminoglycans. Biochem. J. 368: 81–90.
196. Priola, S.A., and V.A. Lawson. 2001. Glycosylation influences cross-species formation of protease-resistant prion protein. EMBO J. 20: 6692–6699.
197. Heller, H., M. Schaefer, and K. Schulten. 1993. Molecular dynamics simulation of a bilayer of 200 lipids in the gel and in the liquid crystal phase. J. Phys. Chem. 97: 8343–8360.
198. Huang, P., F. Lian, Y. Wen, C. Guo, and D. Lin. 2013. Prion protein oligomer and its neurotoxicity. Acta Biochim Biophys Sin. : gmt037.
199. Simoneau, S., H. Rezaei, N. Salès, G. Kaiser-Schulz, M. Lefebvre-Roque, C. Vidal, J.-G. Fournier, J. Comte, F. Wopfner, J. Grosclaude, H. Schätzl, and C.I. Lasmézas. 2007. In Vitro and In Vivo Neurotoxicity of Prion Protein Oligomers. PLoS Pathog. 3: e125.
200. Silveira, J.R., G.J. Raymond, A.G. Hughson, R.E. Race, V.L. Sim, S.F. Hayes, and B. Caughey. 2005. The most infectious prion protein particles. Nature. 437: 257–261.
201. Requena, J.R., and H. Wille. 2014. The structure of the infectious prion protein: Experimental data and molecular models. Prion. 8: 60–66.
202. Cobb, N.J., F.D. Sönnichsen, H. Mchaourab, and W.K. Surewicz. 2007. Molecular architecture of human prion protein amyloid: A parallel, in-register β-structure. PNAS. 104: 18946–18951.
203. Cobb, N.J., A.C. Apetri, and W.K. Surewicz. 2008. Prion Protein Amyloid Formation under Native-like Conditions Involves Refolding of the C-terminal α-Helical Domain. J. Biol. Chem. 283: 34704–34711.
204. Smirnovas, V., G.S. Baron, D.K. Offerdahl, G.J. Raymond, B. Caughey, and W.K. Surewicz. 2011. Structural organization of brain-derived mammalian prions examined by hydrogen-deuterium exchange. Nature Structural & Molecular Biology. 18: 504–506.
205. Diaz-Espinoza, R., and C. Soto. 2012. High-resolution structure of infectious prion protein: the final frontier. Nature Structural & Molecular Biology. 19: 370–377.
206. Sali, A., and T.L. Blundell. 1993. Comparative protein modelling by satisfaction of spatial restraints. J. Mol. Biol. 234: 779–815.
207. Ortega, A., D. Amorós, and J. García de la Torre. 2011. Prediction of hydrodynamic and other solution properties of rigid proteins from atomic- and residue-level models. Biophys. J. 101: 892–898.
208. Wilkins, D.K., S.B. Grimshaw, V. Receveur, C.M. Dobson, J.A. Jones, and L.J. Smith. 1999. Hydrodynamic Radii of Native and Denatured Proteins Measured by Pulse Field Gradient NMR Techniques†. Biochemistry. 38: 16424–16431.
209. Gordon, M. 1970. Statistical mechanics of chain molecules. P. J. Flory, pp. xix + 432, 1969. New York: Interscience. 164s. Brit. Poly. J. 2: 302–303.
210. Sokolowski, F., A.J. Modler, R. Masuch, D. Zirwer, M. Baier, G. Lutsch, D.A. Moss, K. Gast, and D. Naumann. 2003. Formation of Critical Oligomers Is a Key Event during Conformational Transition of Recombinant Syrian Hamster Prion Protein. J. Biol. Chem. 278: 40481–40492.
211. Tahiri-Alaoui, A., V.L. Sim, B. Caughey, and W. James. 2006. Molecular Heterosis of Prion Protein β-Oligomers A POTENTIAL MECHANISM OF HUMAN RESISTANCE TO DISEASE. J. Biol. Chem. 281: 34171–34178.

212. Baskakov, I.V., G. Legname, M.A. Baldwin, S.B. Prusiner, and F.E. Cohen. 2002. Pathway Complexity of Prion Protein Assembly into Amyloid. J. Biol. Chem. 277: 21140–21148.
213. Bocharova, O.V., L. Breydo, V.V. Salnikov, A.C. Gill, and I.V. Baskakov. 2005. Synthetic prions generated in vitro are similar to a newly identified subpopulation of PrPSc from sporadic Creutzfeldt-Jakob Disease. Protein Science. 14: 1222–1232.
214. Novitskaya, V., O.V. Bocharova, I. Bronstein, and I.V. Baskakov. 2006. Amyloid Fibrils of Mammalian Prion Protein Are Highly Toxic to Cultured Cells and Primary Neurons. J. Biol. Chem. 281: 13828–13836.
215. Tayebi, M., D.R. Jones, W.A. Taylor, B.F. Stileman, C. Chapman, D. Zhao, and M. David. 2011. PrPSc-Specific Antibodies with the Ability to Immunodetect Prion Oligomers. PLoS ONE. 6: e19998.
216. Vasan, S., P.Y. Mong, and A. Grossman. 2006. Interaction of Prion Protein with Small Highly Structured RNAs: Detection and Characterization of PrP-Oligomers. Neurochem Res. 31: 629–637.
217. Ulrih, N.P., M. Skrt, P. Veranič, V. Galvani, T. Vranac, and V.Č. Šerbec. 2006. Oligomeric forms of peptide fragment PrP(214–226) in solution are preferentially recognized by PrPSc-specific antibody. Biochemical and Biophysical Research Communications. 344: 1320–1326.
218. Kosmač, M., S. Koren, G. Giachin, T. Stoilova, R. Gennaro, G. Legname, and V.Č. Šerbec. 2011. Epitope mapping of a PrP(Sc)-specific monoclonal antibody: Identification of a novel C-terminally truncated prion fragment. Molecular Immunology. 48: 746–750.
219. Oboznaya, M.B., S. Gilch, M.A. Titova, D.O. Koroev, T.D. Volkova, O.M. Volpina, and H.M. Schätzl. 2007. Antibodies to a Nonconjugated Prion Protein Peptide 95-123 Interfere with PrP Sc Propagation in Prion-Infected Cells. Cell Mol Neurobiol. 27: 271–284.
220. Peretz, D., R.A. Williamson, K. Kaneko, J. Vergara, E. Leclerc, G. Schmitt-Ulms, I.R. Mehlhorn, G. Legname, M.R. Wormald, P.M. Rudd, R.A. Dwek, D.R. Burton, and S.B. Prusiner. 2001. Antibodies inhibit prion propagation and clear cell cultures of prion infectivity. Nature. 412: 739–743.
221. Donofrio, G., F.L. Heppner, M. Polymenidou, C. Musahl, and A. Aguzzi. 2005. Paracrine Inhibition of Prion Propagation by Anti-PrP Single-Chain Fv Miniantibodies. J. Virol. 79: 8330–8338.
222. Beringue, V., D. Vilette, G. Mallinson, F. Archer, M. Kaisar, M. Tayebi, G.S. Jackson, A.R. Clarke, H. Laude, J. Collinge, and S. Hawke. 2004. PrPSc Binding Antibodies Are Potent Inhibitors of Prion Replication in Cell Lines. J. Biol. Chem. 279: 39671–39676.
223. Moroncini, G., N. Kanu, L. Solforosi, G. Abalos, G.C. Telling, M. Head, J. Ironside, J.P. Brockes, D.R. Burton, and R.A. Williamson. 2004. Motif-grafted antibodies containing the replicative interface of cellular PrP are specific for PrPSc. PNAS. 101: 10404–10409.
224. Novitskaya, V., N. Makarava, A. Bellon, O.V. Bocharova, I.B. Bronstein, R.A. Williamson, and I.V. Baskakov. 2006. Probing the Conformation of the Prion Protein within a Single Amyloid Fibril Using a Novel Immunoconformational Assay. J. Biol. Chem. 281: 15536–15545.
225. Solforosi, L., A. Bellon, M. Schaller, J.T. Cruite, G.C. Abalos, and R.A. Williamson. 2007. Toward Molecular Dissection of PrPC-PrPSc Interactions. J. Biol. Chem. 282: 7465–7471.

226. Biasini, E., M.E. Seegulam, B.N. Patti, L. Solforosi, A.Z. Medrano, H.M. Christensen, A. Senatore, R. Chiesa, R.A. Williamson, and D.A. Harris. 2008. Non-infectious aggregates of the prion protein react with several PrPSc-directed antibodies. Journal of Neurochemistry. 105: 2190–2204.
227. Chiesa, R., P. Piccardo, E. Biasini, B. Ghetti, and D.A. Harris. 2008. Aggregated, Wild-Type Prion Protein Causes Neurological Dysfunction and Synaptic Abnormalities. J. Neurosci. 28: 13258–13267.
228. Biasini, E., A.Z. Medrano, S. Thellung, R. Chiesa, and D.A. Harris. 2008. Multiple biochemical similarities between infectious and non-infectious aggregates of a prion protein carrying an octapeptide insertion. Journal of Neurochemistry. 104: 1293–1308.
229. Stanker, L.H., M.C. Scotcher, A. Lin, J. McGarvey, S.B. Prusiner, and R. Hnasko. 2012. Novel Epitopes Identified by Anti-PrP Monoclonal Antibodies Produced Following Immunization of Prnp0/0 Balb/cJ Mice with Purified Scrapie Prions. Hybridoma (Larchmt). 31: 314–324.
230. Korth, C., B. Stierli, P. Streit, M. Moser, O. Schaller, R. Fischer, W. Schulz-Schaeffer, H. Kretzschmar, A. Raeber, U. Braun, F. Ehrensperger, S. Hornemann, R. Glockshuber, R. Riek, M. Billeter, K. Wüthrich, and B. Oesch. 1997. Prion (PrPSc)-specific epitope defined by a monoclonal antibody. Nature. 390: 74–77.
231. Khalili-Shirazi, A., M. Kaisar, G. Mallinson, S. Jones, D. Bhelt, C. Fraser, A.R. Clarke, S.H. Hawke, G.S. Jackson, and J. Collinge. 2007. β-PrP form of human prion protein stimulates production of monoclonal antibodies to epitope 91–110 that recognise native PrPSc. Biochimica et Biophysica Acta (BBA) - Proteins and Proteomics. 1774: 1438–1450.
232. Thuring, C.M.A., J.H.F. Erkens, J.G. Jacobs, A. Bossers, L.J.M. Van Keulen, G.J. Garssen, F.G. Van Zijderveld, S.J. Ryder, M.H. Groschup, T. Sweeney, and J.P.M. Langeveld. 2004. Discrimination between Scrapie and Bovine Spongiform Encephalopathy in Sheep by Molecular Size, Immunoreactivity, and Glycoprofile of Prion Protein. Journal of Clinical Microbiology. 42: 972–980.
233. Zanusso, G., M. Fiorini, S. Ferrari, K. Meade-White, I. Barbieri, E. Brocchi, B. Ghetti, and S. Monaco. 2014. Gerstmann-Sträussler-Scheinker disease and “anchorless Prion Protein” mice share prion conformational properties diverging from sporadic Creutzfeldt-Jakob disease. J. Biol. Chem. : jbc.M113.531335.
234. Kumar, J., S. Sreeramulu, T.L. Schmidt, C. Richter, J. Vonck, A. Heckel, C. Glaubitz, and H. Schwalbe. 2010. Prion Protein Amyloid Formation Involves Structural Rearrangements in the C-Terminal Domain. ChemBioChem. 11: 1208–1213.
235. Serpa, J.J., A.P. Patterson, J. Pan, J. Han, D.S. Wishart, E.V. Petrotchenko, and C.H. Borchers. 2013. Using multiple structural proteomics approaches for the characterization of prion proteins. Journal of Proteomics. 81: 31–42.
236. Groveman, B.R., M.A. Dolan, L.M. Taubner, A. Kraus, R.B. Wickner, and B. Caughey. 2014. Parallel In-register Intermolecular β-Sheet Architectures for Prion-seeded Prion Protein (PrP) Amyloids. J. Biol. Chem. 289: 24129–24142.
237. Larda, S.T., K. Simonetti, M.S. Al-Abdul-Wahid, S. Sharpe, and R.S. Prosser. 2013. Dynamic Equilibria between Monomeric and Oligomeric Misfolded States of the Mammalian Prion Protein Measured by 19F NMR. J. Am. Chem. Soc. 135: 10533–10541.

238. Kazlauskaite, J., N. Sanghera, I. Sylvester, C. Vénien-Bryan, and T.J.T. Pinheiro. 2003. Structural Changes of the Prion Protein in Lipid Membranes Leading to Aggregation and Fibrillization†. Biochemistry. 42: 3295–3304.
239. Critchley, P., J. Kazlauskaite, R. Eason, and T.J.T. Pinheiro. 2004. Binding of prion proteins to lipid membranes. Biochemical and Biophysical Research Communications. 313: 559–567.